NSF Grant ATM-8814913
NOAA Contract #NA85RAH05045

A NUMERICAL SIMULATION OF TORNADOGENESIS

by Lewis D. Grasso

William R. Cotton, P.I.

Colorado State University

DEPARTMENT OF ATMOSPHERIC SCIENCE

PAPER NO. 495

A NUMERICAL SIMULATION OF TORNADOGENESIS

by

Lewis D. Grasso

Department of Atmospheric Science

Colorado State University

Fort Collins, CO 80523

Research Supported by

National Science Foundation

under Grant ATM-8814913

National Oceanic and Atmospheric Administration

under Contract #NA85RAH05045

May 15, 1992

Atmospheric Science Paper No. 495

ABSTRACT

A NUMERICAL SIMULATION OF TORNADOGENESIS

The CSU RAMS was used to investigate tornadogesesis using high resolution interactive nests to explicitly resolve the tornado. Convection was initiated with a warm bubble in a horizontally homogeneous environment using from a composite of soundings taken May 20, 1977, the day of the Del City tornado.

The simulated supercell has many observed characteristics some of which are: a hook echo, bounded weak echo region, strong updrafts and a mesocyclone.

The high resolution nests captured the necessary features that allowed tornadogenesis to occur. It is found that a pressure-deficit tube developed on the largest horizontal gradient of the updraft when the magnitude of the three dimensional vorticity exceeded the strain rate in this region. It is suggested that efficient tilting/convergence of vortex lines by the updraft gradient aided in allowing the vorticity term to exceed the strain term, in the diagnostic equation for pressure, and allow pressures to fall rapidly.

Near cloud base and below, this tilting/convergence of vortex lines will locally be unable to allow the pressures to continue to fall at the base of the pressure-deficit tube since vertical motion is constrained to vanish at the lower boundary. The storm's downdrafts are thought to play a key role in reorientating vortex lines into a vertical position in the sub-cloud air. Convergence of sub-cloud air towards the pressure-deficit tube will also draw in already vertically orientated vortex lines. Once the vortex lines are converged sufficiently, the pressures will fall as the flow exhibits highly rotational characteristics, and allow the pressure-deficit tube to continue working towards the lower boundary. As the

lower boundary is approached, increasing frictional forces will enhance the convergence of vortex lines.

Lewis D. Grasso
Department of Atmospheric Science
Colorado State University
Fort Collins, Colorado 80523
Summer 1992

ACKNOWLEDGEMENTS

My warmest thanks are extended to the following people: Dr. William Cotton and Dr. Robert Walko for their guidance in this subject area, Brenda Thompson for her help in preparing this thesis and finally Judy Sorbie-Dunn and Lucy McCall for aiding me with the figures.

This research was supported by the National Oceanic and Atmospheric Administration under contract NA85RAH05045 and the National Science Foundation under grant ATM-8814913.

Computations were performed on the CSU Stardent computer, which was purchased under support of the Army Research Office under contract DAAL03-86-K-0175.

TABLE OF CONTENTS

Chapter 1

INTRODUCTION

Each spring in the central plains of the United States, groups of people get very excited with the appearance of a "shot gun" sounding in the early morning. Quickly they run to the 500 mb chart to see if colder air will blow in and jump up and down if they see P.V.A. over the region in question. Some losing composure, will examine jet streaks at 200 or 300 mb to see where the right entrance region or the left exit region is in relation to other features. Although these people don't have a name, one could call them "tornado groupies"! After they consult the maps and if it looks like severe weather is imminent, their hearts start pounding, the blood rushes through their veins, some may even hyper-ventilate, the excitement is overwhelming, quite similar to children on Christmas morning waiting to rush to the tree to open their gifts!

The next thing these people must do is find someone who is willing to sacrifice their car in case of large hail, core punching, as it's called, often is necessary, some do it for fun! That one lucky person must also be willing to risk getting a speeding ticket, as it's often necessary to exceed legal speed limits to get better video, video? Oh my God, who has the camcorder? Once this person is found, off they go, racing aimlessly across unfamiliar territory in the hopes of witnessing on of mother natures most awesome, beautiful and devastating phenomena ...the tornado!

If these people are lucky enough to see a tornado their reaction all across the country is the same...blurred, indistinguishable speech. Just listen to any video during that moment as testimony. Suddenly shock overwhelms their body's, speech slows to a grinding halt as though a divine thing had occurred. They all try to say "wow" while their lower jaw falls to the ground. What they are witnessing is incomprehensible. For the person

who is directly effected by the tornado there is nothing exciting about it, in fact, it's more like a living hell, loved ones killed, dream homes completely destroyed and in some cases entire towns wiped off the face of the earth in a matter of a few short horrifying moments that ironically seems like forever to end.

With tornadic supercell thunderstorms being so often observed by these tornado groupies it wasn't long before somebody asks "why?", why do these storms behave the way they do? Unfortunately these answers had to wait until three dimensional numerical models and Doppler radar were developed so as to "see" inside the thunderstorm and investigate the parameters that explain the storm behavior.

1.1 Review of Modelling Efforts

Three dimensional numerical cloud models to simulate cumulus convection made their debut in the early 1970's. In what follows is a review of modelling efforts since that time. It will be pointed out what these models were able to do well and their limitations.

Robert Wilhelmson (1974) ran a three dimensional numerical cloud model to simulate deep precipitating convection in an environment characterized by one directional vertical shear. The lateral boundary conditions used are periodic in x and y. The lower and upper boundaries are rigid, turbulent free and free slip. The model was initiated horizontally homogeneous with an idealized vertical sounding of temperature that is conducive to convective overturning. The winds are unidirectional with an imposed vertical shear from -6 m/s at 300 m to 6 m/s at 8.1 km. The winds below 300 m are held constant at -6 m/s as are the winds above 8.1 km held fixed at 6 m/s. Convection was triggered using an axisymmetric warm bubble from Z = 900 m to 2100m.

The domain is 38.4 km on a horizontal side and 15 km in the vertical. The grid spacing is the same in all directions and is equal to 600 m with a 30 s time step.

The simulation was only run out to 55 minutes due to the contaminating effects of amplifying internal gravity waves triggered by numerical instability. Although the simulated convection does not have the added "push" from the latent heat of freezing and the

shear was weak by typical supercell standards, the model did resolve basic features observed in thunderstorms, namely the perturbation high at the storm top and the apparent obstacle like flow at mid-levels around the convective element.

Schlesinger (1978) used a three dimensional numerical cloud model to study the effects of variable ambient vertical wind shear on storm development. An overview of this model is the following main points;

1) flow is anelastic

2) Coriolis is neglected

3) no ice phase, liquid water is partitioned into cloud and rain

4) liquid water exerts a drag force equal to its weight

5) supersaturation is instantaneously removed by latent heat release, liquid water in unsaturated air evaporates until the wet bulb temperature is reached or until all liquid water is completely evaporated

6) cloud and raindrop parameterization follows that of Takeda (1966) All water drops have the same horizontal speed as the wind field. Cloud water has zero terminal fall speed relative to air. The terminal fall speed of rainwater is a function of rainwater content.

7) turbulent diffusion of momentum, heat and moisture is modelled similar to Deardorff (1970).

The model was initiated horizontally homogeneous, that is, no initial vertical vorticity or horizontal divergence, with an idealized vertical temperature structure that is conducive to convection. The winds were varied from unidirectional to strong low level veering.

The convection was initiated by a cylindrical buoyant updraft with its axis on the center grid of the domain. The updraft is 9 km in radius and extends through the lowest 4.2 km The largest perturbation in temperature and vertical speeds are 1°C at 1.75

km and 3 m/s at 1.4 km respectively. The relative humidity is slightly larger than the surrounding environment.

Since the grid domain is in each horizontal direction 48.6 km with 27 grid intervals and 14 km in the vertical with 20 grid intervals the winds were reduced 30 to 40 percent so as to prevent the convective element from moving rapidly out of the domain. The results here expand on Wilhelmson's study and they are:

1) sheared storms exhibit quasi-erect high speed updrafts. Cyclonic-anticyclonic vortex pair aloft, mid-level barrier flow around the updraft and storm splitting.

2) sheared storms have a weak growing stage but the mature stage is stronger and more persistent updrafts and downdrafts. Convergence at the surface is with shear.

3) With shear, the mid-level perturbation low migrates from the storm center to the right and left flank

4) perturbation pressures lift non-buoyant subcloud air into the storm

5) with directional turning of the shear vectors, one of the split storms is stronger.

Klemp and Wilhelmson (1978a,b) give us an idea into how three dimensional numerical cloud modelling is limited, they say, "...Three dimensional modeling currently requires sacrifices in the representation of physical processes and in the scales of resolution which must be made through careful consideration of one's modelling goals. It is not feasible, for example, to model storm evolution with a grid that lies well with in the inertial subrange, with a domain three or four times the storm size and with a detailed representation of microphysical interactions."

For their study, the top, bottom and lateral boundary conditions have been derived by Oliger and Sundstrom (1976) and they are:

1) top and bottom, require $W = 0$

2) lateral boundaries are open in an attempt to minimize gravity waves being reflected and is similar to Klemp and Lilly (1978)

The grid width on each horizontal side is 1000 m and in the vertical is 500 m. The domain is 24 km in each horizontal direction and 10 km in the vertical. The model was initiated horizontally homogeneous and convection was triggered using a warm bubble. A 10 s time step was used throughout the simulation.

The results of the simulation, with vertical shear, are able to capture the storm splitting process. They propose that liquid water loading is a possible mechanism.

In an other study, Klemp and Wilhelmson (1978) showed, using the three dimensional numerical cloud model described above that after the storm splitting process the right member will become stronger and favored for further development over the left member in an environment characterized by a hodograph where the shear vectors turn clockwise. The opposite is true for counter clock wise turning shear vectors.

Schlesinger (1980) points out that Klemp and Wilhelmson's idea that rainwater loading might be responsible for the split of the initial storm needs to be looked at closer. He suggests that ingestion and mixing of evaporatively cooled outside air may also contribute to storm splitting. In the model used here, open non-periodic lateral boundaries are used. The upper and lower boundaries are rigid and free slip. The horizontal grid spacing in each horizontal direction is 1.8 km. The vertical grid resolution is 700 m. The domain is 48.6 km on a horizontal side and 14 km in the vertical. Following Takeda (1966) liquid water is partitioned into cloud drops and precipitation. The model is initially horizontally homogeneous with vertical shear of the horizontal wind with marked low level veering. The convection was initiated with a rising thermal perturbation.

One conclusion drawn was that twin meso-lows aloft at the cloud flanks aid in updraft splitting in four ways, they are;

1) a divergent horizontal pressure gradient force with in the cloud is induced between the flanks

2) a low level upward pressure gradient force is concentrated between the flanks

3) parcels feeding the secondary downdraft are steered quasi cyclostrophically around the flanking low centers and into the front of the cloud

4) these parcels encounter a downward pressure force.

Later a diagnostic equation for pressure is derived by the author, one term involved is the square of the magnitude of the three dimensional vorticity vector. This term can be used to explain the formation of the meso lows appearing on the flanks of the convective updraft. Consider initially an east west orientated vortex tube with the vorticity vector pointing west. Consider an atmosphere where the equivalent potential temperature surfaces are horizontal. Therefore initially, the vortex tube lies on an equivalent potential temperature surface. If equivalent potential vorticity is conserved, then the vortex tube must always lie on that surface. As the convective updraft grows, it bulges up the θ_e surface, during this process, the vortex tube is also lifted up. At this time, the θ_e surface can be looked at as a hill and the vortex tube as a garden hose riding up and over the hill. Moving from east to west, the vortex tube is horizontal until one approaches the updraft. On the east side of the updraft, the vortex tube has a vertical component, generating positive vertical vorticity. On the west side of the updraft the vortex tube has a negative vertical component. In terms of forming a meso-low, the sign of the vertical vorticity is immaterial. Due to the horizontal gradient of the updrafts vertical speed, horizontal vorticity is generated azimuthally around the convective element. This horizontal vorticity is basically the same around the updraft in the growing stage, however, the three dimensional vorticity is not. The magnitude of the three dimensional vorticity is largest on the east and west sides of the updraft due to the extra component due to the initially horizontal vortex tube being drawn up by the bulging equivalent potential temperature surface. Since the magnitude of the three dimensional vorticity is largest on the right (east) and left (west) flanks of the updraft, and if the strian rate is smaller in magnitude, it follows from the diagnostic equation for pressure that the pressure deficits will be largest in these regions, hence, the formation of two meso-lows on the right and left flanks.

Wilhelmson and Klemp (1981) ran their three dimensional numerical cloud model again to study storm splitting, however, instead of using some idealized conditions, a composite sounding for the region where severe weather had actually occurred was used

to initiate the model. A warm bubble was used to trigger the convection. The domain was 80 km in the east west direction and 160 km in the north south direction with 16.5 km in the vertical. The grid spacing was 2 km for the horizontal and 750 m for the vertical with a 10s time step.

Klemp et al. (1981) simulated the Del City supercell thunderstorm of May 20, 1977 by initializing the model with a composite sounding constructed from special soundings taken in the near storm environment. The domain was 48 km in each horizontal direction and 16 km in the vertical, the grid spacing was 1 km in the horizontal and 500 m in the vertical. Numerical results were compared to Doppler radar data sets on the observed storm.

Air parcel trajectories were calculated to get a view of the storms internal structure. The authors also inform us about the current state of the numerical models used for storm simulation. They say "...since the resolution in current three dimensional models is never sufficient to adequately resolve all scales of motion with in a storm ..." and "...unfortunately, computational restrictions prevent our recomputing the entire simulation using a finer mesh ...".

Rotunno and Klemp (1981) used linear theory to show that the interaction of the updraft with the mean shear produces a favorable vertical pressure gradient on the storms right flank. It was shown that a perturbation high forms upshear and a perturbation low forms down shear. The clockwise turning of the shear vectors will generate an upward vertical pressure force on the right flank and a downward vertical pressure gradient force on the left flank.

The Klemp-Wilhelmson model was used for this endeavor with a domain size of 32 km in the horizontal and 10 km in the vertical. The horizontal grid resolution is 1 km and a vertical grid spacing of 500 m. A 20 s time step was used. Periodic lateral boundary conditions was used with a rigid upper and lower boundary where $W = 0$. The model was initiated with a composite of soundings in a severe weather region and the convection was started with a warm bubble.

Weisman and Klemp (1982) investigated the dependence of isolated storm characteristics on various magnitudes of buoyancy and vertical shear of the horizontal wind. Using the Klemp-Wilhelmson model, initialized with a horizontally homogeneous state, has a domain size of 40 km in the east west direction, 60 km in the north south direction and 17.5 km in the vertical. The horizontal grid spacing was 2 km and the vertical grid was stretched from 350 m at the bottom to 1 km at the top boundary. The convection was started with an axisymmetric thermal with a ten kilometer horizontal radius and 1400 m vertical radius with the maximum temperature excess of 2.0 C. A bulk Richardson number was defined to be the ratio of the parcel buoyancy to the mean zonal kinetic energy of the storm environment. The parcel buoyancy is proportional to the integrated temperature excess of the parcel. For supercell thunderstorms, the bulk Richardson number takes on values from fifteen to thirty.

Rotunno (1984) proposed a theory for tornadogenesis with the combined help of coarse grid numerical simulations and laboratory tornado chamber experiments. A high resolution numerical simulation is not presented and he points out "...given the present state of computers, it is impossible for the three dimensional cloud models, even with nested grids, to simulate both the supercell on a domain large enough to include the undisturbed environment and the tornado with a resolution fine enough to capture the significant dynamical processes ...". He further points out that even if this were possible the simulation would produce too much data and it would be an overwhelming task for any one person to sift through in search of the tornadogenetic process!

Chapter 2

SEVERE STORM ENVIRONMENT AND MORPHOLOGY

One of the first parameters looked at for an indication of possible severe storm development is the vertical sounding of temperature, moisture and winds. One type of sounding is the "tuning fork" or more commonly referred to as the "shot gun" sounding, characterized by the lowest 100 mb or so being nearly adiabatic and high relative humidity capped by a significant inversion. Above the inversion the temperature profile may again be close to adiabatic and very dry up to the mid troposphere. The temperature structure becomes more isothermal as the tropopause is approached. The winds will show significant low-level veering with mid- to upper- tropospheric speed shear. This is an environment that is capable of supporting tornadic supercell thunderstorms (Fawbush and Miller, 1954).

However, the ability for an atmosphere to support severe thunderstorm development doesn't mean that severe storms will develop. It is possible for the vertical shear of the horizontal wind to be too large. In this situation, entrainment will be great and inhibit storm growth. The downshear tilt of the growing updraft will be large and the temperature excess in the core will be smaller than it otherwise would be. The convective available potential energy (CAPE) may also be too large for a given profile of vertical wind shear. Numerical experiments show that a storm with too large CAPE will produce a strong enough downdraft to actually force the gust front to race away from the parent storm and effectively cutting off the convergent lifting of warm moist air directly into the storms updraft. The storm is no longer being fueled and will dissipate. New storm development may occur along the outflow boundary left behind. Therefore, the buoyant energy must be in balance with the vertical shear to allow a growing convective element

to mature into a supercell thunderstorm (Weisman and Klemp, 1982). Even though the buoyant energy is in balance with the vertical shear, large scale subsidence may inhibit the low level inversion from being eroded to allow the release of the convective energy. A forcing mechanism must be available to lift the air beneath the inversion, as this air is typically negatively buoyant. This forcing could be topographically-induced. A very common type of boundary is the dry line to trigger convection. Convergence, set up by sea breezes, such as in Florida, or related fronts from large inland bodies of water or large regions of rain wetted soil. The wetted soil will not heat as rapidly as its neighboring dry soil. The result is a thermal gradient that may act as a forcing. Old thunderstorm outflows will also provide the forcing, provided they do not propagate too far since the further they travel the shallower the leading edge becomes. Cold fronts associated with mid-latitude synoptic baroclinic waves provide an other mechanism of forcing. Interestingly enough, these frontal boundaries, especially the cold front, do not always trigger convection. Associated with cold fronts are jet streams in the upper troposphere. These jet streams may exhibit one or more jet streaks (Palmen and Newton, 1969, pg 199). It is worth while discussing the role played by jet streaks in stabilizing or destabilizing the environment so as to prohibit or enhance the development of severe cumulus convection.

Consider an east west jet streak. Let us assume the flow is in geostrophic balance upstream of the entrance region of the jet streak. Geostrophic flow in a hydrostatic environment implies thermal wind balance. Again, since the flow is hydrostatic the horizontal vorticity is given by the vertical unit vector cross multiplied by the shear vector. Therefore thermal wind balance can be viewed as the horizontal vorticity vector being anti-parallel to a constant, times the horizontal temperature gradient. Consider a parcel flowing into the jet streak above the jet core. Since the environmental vertical shear is increasing rapidly as the parcel enters the streak, the southward pointing horizontal vorticity vector will increase in magnitude. The flow is no longer in geostrophic or equivalently thermal wind balance. The atmosphere must compensate by producing a secondary circulation to try to bring the flow back into a balanced state. As the parcel enters the jet streak, the

northward pressure gradient force is getting larger. The Coriolis torque however, will not have time to adjust and bring the flow back into balance, hence, the parcel "sees" a net northward force that produces an ageostrophic northward cross-stream flow. The east side of the jet streak entrance region is now strongly divergent, as a result, upward vertical motion is produced below to satisfy continuity of mass. It is this ascending branch of the secondary circulation that puts the atmosphere in an even more convectively unstable situation through adiabatic cooling associated with the ascent. The result is a deep adiabatic layer above the low level inversion. Any stable layers under the influence of the ascending branch will effectively be removed. The low level inversion is no longer supported, the surface forcing, not required to be as strong now, can trigger convective overturning of the atmosphere and lead quickly to severe thunderstorm development. It is possible for the surface forcing to be under the descending branch of the secondary circulation associated with the jet streak. In this case the low level inversion has support and may be strong enough to prevent any convection from occurring (Uccellini and Johnson, 1979).

Similar analysis can be applied to the jet streak exit region. Assume the air parcels are in geostrophic balance upstream of the jet exit region. As the parcels enter into the exit region the horizontal pressure gradient will get smaller. The Coriolis force will not adjust rapidly enough to keep the flow in geostrophic balance and therefore will be the larger force and turn the flow anti-cyclonically from an easterly direction towards the south and up the horizontal pressure gradient. The left exit region will become strongly divergent and the right exit region will become convergent. To satisfy mass continuity, upward vertical motion will develop at levels below the left exit region and sinking below the right exit region. Therefore the optimal location for storm development will be co-located with the left exit region of a jet streak.

Once convection begins, the growing storms must continually be supported with warm air that, once lifted, will accelerate vertically upward on its own. A thunderstorm growing with no inflow will not last long, therefore storm relative motion at the low levels from the warm, moist side is one necessary ingredient to maintain storm longevity.

Observational and numerical evidence supports the conclusion that once convection is triggered, the bulk Richardson number, the ratio of available buoyancy to vertical wind shear, will drive the storms into a particular category, be it single cell, multicell or supercell (Weisman and Klemp, 1982). It can't be over emphasized that there does not exist a clear distinction between these particular storm types. Multicell storms may and do at times have supercell characteristics (Cotton and Anthes, 1989, pg 526). Be it as it may, there do exist thunderstorms that can be unmistakably labeled supercells, it is the development of this type of storm that will now be described.

As the nacient cloud begins its life, it immediately interacts with its environment. In the growing stage the cloud is lifting equivalent potential temperature surfaces and the corresponding vortex tubes that are horizontally-oriented from the vertical shear of the horizontal wind. The young cloud will be moving very rapidly towards the north with the low level winds. The action of drawing up vortex tubes will cause the right flank of the updraft to produce positive vertical vorticity. The left flank of the updraft will obtain negative vertical vorticity (Lilly, 1982). As will be discussed later, two diametrically, approximately, opposed meso-lows will form on the storms flanks. The results of the perturbation lows can be seen quite nicely with the horizontal wind field. On the upwind side of the cloud, the flow is towards the north. Recall the cloud has not grown to considerable depths yet and as such is under the influence of the low level winds. As the flow approaches the cloud, in the storm relative sence, it will "split" with one branch flowing towards the northeast and the other branch flowing towards the northwest (Robert Davies-Jones,1982). The branch moving off to the northeast will be influenced by the meso-low on the storms right flank. The meso-low will cause this branch to turn counter-clockwise and the meso-low on the left flank will cause the left branch, heading off to the northwest, to turn clockwise. These branches will converge directly downwind of the cloud. Moreover, the meso-lows will draw this air into the storm enhancing the entrainment into the front of the cloud. At this time microphysical processes have produced hydrometeors primarily on the downshear side of the updraft or in the same region that the environmental air is being entrained into the storm (Schlesinger, 1980).

The hydrometeors will induce a downdraft from a drag force. The combination of this induced-downdraft and the entrainment will cause the updraft to split. The result of the storm-splitting process is to leave the left member in an anticyclonically rotating state with respect to the vertical and the right cell rotating cyclonically. The updrafts in the new cells are a little weaker and will go through a re-growing stage. The left member may continue to head north or perhaps head off on a slight north-westerly direction. However, the environment that the left storm is embedded in will not support its growth.

It can be shown that when an updraft interacts with vertical shear, a perturbation high will form up the shear vector and a perturbation low on the downshear side of the shear vector (Rotunno and Klemp, 1982). Consider the environment where the shear vector turns clockwise with height. This turning of the shear vectors will produce an upward perturbation pressure force on the right flank of the updraft and a downward perturbation force on the left side of the updraft. Since the left moving storm will have its inflow on the left flank, the vertical perturbation pressure force will inhibit updraft development, i.e., subcloud air is being forced up by surface convergence. This air usually is non-buoyant, however the downward perturbation pressure force will inhibit this air from reaching its level of free convection. The above mechanism is one of a few preventative influences of the environment on the left moving storm and subsequently the storm dissipates. The right member storm, due to the inflow being on the right flank and the perturbation pressure force aiding in lifting the non-buoyant subcloud air into the updraft, will continue to grow. As the vertical perturbation pressure gradient force on the right flank will always aid in the development on the right flank of the updraft, this will cause the storm to move continually to the right of the mean wind (Rotunno and Klemp, 1982). This can be a spectacular event when viewed by satellite. On the large scale cloud systems will be moving in a general northeast path, however, some embedded thunderstorms, clearly move east! A close up by a high resolution fast scanning satellite will show overshooting tops moving northeast in the anvil canopy and the right moving storms are easily detected since their overshooting tops will be moving due east!

The strongly-sheared environment will lean the storms downshear. This tilt is necessary as it will cause precipitation to fall outside of the updraft (Ludlam, 1963). Typically

the precipitation falls to the north and northwest of the main updraft with the largest radar reflectivity towards the northwest of the updraft. The evaporation of precipitation cools the air in the forward flank downdraft. This cool pool forms a thermal boundary that extends ahead of the storm towards the northeast. Environmental air originating at the two kilometer level flows cyclonically around the right flank towards the forward flank where it descends in the precipitation to feed the forward flank downdraft. Some of this downdraft air continues to rotate cyclonically near the surface, on the rear flanks of the storm and forms the gust front. This gust front stays in phase with the storm due to the delicate balance between available buoyant energy and the environmental vertical shear. This boundary increases the surface convergence and further aids in lifting warm, moist, but still non-buoyant, air into the storm. At this stage the supercell is in the mature stage.

A vertical scan through a storm reveals another interesting feature about the intensity of the updraft. A strong updraft will rapidly carry growing hydrometeors up and out of the lower parts of the updraft before microphysical processes allow the hydrometeors to grow large enough to reflect significant amounts of radar energy. The strength of the updraft will also produce a precipitation "ceiling" on top of the low level updraft. This low level updraft region is called the weak echo region (WER) or echo-free vault (Browning and Ludlam, 1960, 1962) due to the lack of radar reflectivity. As the updraft further intensifies, the precipitation ceiling will be pushed up so as to produce more of a dome like feature. A horizontal cut by radar through the dome will reveal low or no echo in the center of the dome with higher reflectivity bounding the center dome on all sides. This central weak echo dome is referred to as the bounded weak echo region (BWER) (Chisholm and Renick, 1972). Some bounded weak echo regions can be quite spectacular, resembling a vertically oriented cylindrical hole in the hydrometer field. This is indicative of an extremely intense updraft, thrusting hydrometeors higher into the storm, leaving behind a minimum in the reflectivity field. It is these types of severe storms that are able to produce extreme amounts of supercooled liquid water mixing ratios and to suspend the growing hailstones at large enough heights above the freezing level to allow the hail

to traverse the hydrometer field and grow via wet and dry growth to produce the rings commonly observed in cut hailstones. The largest hail falls out to the northwest and adjacent to the updraft. Tennis ball to baseball sized hail is not uncommon in severe supercell thunderstorms.

With the advent of Doppler radar, the wind field internal to the storm can be examined (Battan, chapter 8, 1973), especially with multiple-Doppler radar scans. The scientist can now "see" the rotational characteristics of the updraft. Of course, a time lapse movie loop of the visual storm can also capture the rotation of the cloud mass. If the rotation is strong enough the circulation will be called a mesocyclone. A single Doppler radar is able to detect mesocyclone circulations within the thunderstorm (Burgess, Wood and Brown, 1982). At times an even smaller circulation develops on the gradient of upward vertical motion. This was originally called gate to gate shear (Burgess et al, 1976), however, in the late 1970's the term tornado vortex signature, or, TVS, was coined (Brown et al, 1978), since it precedes the formation of a tornado by about one half an hour. Numerous Doppler radar observations have consistently indicated that the mesocyclone and the embedded tornadic vortex signature form on the largest horizontal gradient of the vertical motion with the location primarily within the updraft. If there is more that one region of large horizontal gradient of vertical motion the mesocyclone seems to form in the gradient associated with the inflow side of the storm (Brandes, 1984). At this time the mesocyclone is intense enough at the lower levels to wrap the precipitation cyclonically around the rear flanks of the storm. On radar this would appear as the "hook echo". The appearance of the hook echo alone is enough to issue a tornado warning to the public. At this stage of the storm's development a tornado may be spawned.

In the process of tornado-genesis, a distinct lowering of the rain-free base may at times be present. The cloud base that has lowered is referred to as the wall cloud (Fujita, 1959). The wall cloud may have striations spiraling diagonally up and around its edge indicative of strong rotation. The ground observer may at times observe the rotation without much difficulty. If close enough to observe the base of the wall cloud, a local region may exhibit marked rotation and the formation of a funnel cloud as the air being

pulled into this low pressure and low temperature region condenses to make the funnel visible. The funnel will then lower towards the ground, at times however, the funnel may contract back towards the wall cloud or linger at a fixed height for a period of time. When the funnel approaches the ground, the circulation at the ground may already be present. If there does exist rotation on the ground, even though the visible funnel is not in contact with the ground, the resulting vortex is called a tornado. The general public is often drawn to the incorrect conclusion that since the visible funnel is not on the ground, no surface damage will occur. In Colorado, for example, some thunderstorms produce no wall cloud and no visible tornadic funnel! The only indication that a tornadic vortex is actually present is the visible debris rotating at the surface. This situation can be potentially dangerous since the observer may detect a slight indication of rotation at cloud base, maybe the presence of a very thin and short funnel, but following this circulation from cloud base to the ground can be a monumental task. The first instinct may be to look at the ground directly underneath the rotation at cloud base, however, the tornadic vortex may not even exist or if it does, it may arc out from the cloud base and make contact with the ground a large distance from the place on the ground that is directly underneath the rotation at cloud base. The public has an advantage with tornadoes that have a visible vortex to the ground in that at least they know where it is!

Once tornadoes form, the weaker ones may last a few minutes while the stronger ones may last up to and exceed one hour (Robert Davies-Jones,1982). The visible vortex may appear to be quite smooth and well-defined or quite jagged. The mature tornado may have a small tilt away from the vertical. The more intense tornadoes may, and often do, produce smaller scale vortices within and on the edge of the tornado itself. These smaller scale features are called suction vortices. The dissipation or rope stage of the tornado is characterized by the visible tornado becoming very narrow, like a rope, and developing a large tilt with the surface circulation moving rapidly away from the storm and still being able to do considerable damage.

The processes that effect the life time of the tornado are not well understood, however, the ability of the rear flank gust front to move out ahead of the parent updraft seems

to be enough to choke off the warm moist inflow. The tornado could be surrounded by a precipitation curtain whose air is cool and highly non-buoyant. The dissipation of the tornado generally will follow. If for some reason the gust front does not move out and cause an occlusion of the parent updraft, then it seems possible for some sort of balance to occur and allow the tornadoes life to be extended. Typically the gust front does occlude the updraft and a new updraft and hence new mesocyclone will form quickly being able to produce a tornado in some forty five minutes. It is this process that produces tornado families. If the gust front is unable to produce a new updraft after occluding the parent storm, then the parent storm will dissipate and convection will end having efficiently stabilized the atmosphere through which it traveled.

Tornadoes typically rotate counter-clockwise, however, statistically one out of several hundred will rotate clockwise (Fujita and Wakimoto, 1982). Oddly enough, the parent thunderstorms mesocyclone is characterized by cyclonic rotation in the northern hemisphere. In two hours on June 3, 1980 a parent mesocyclone spawned seven tornadoes in Grand Island Nebraska and three of them were anticyclonic (Fujita and Wakimoto, 1982). The National Weather Services radar at the Grand Island airport captured spectacular footage of the cyclonic hook echo of one of the cyclonic tornadoes. In the hook echo a black spot appeared on the radar scope. On a Doppler radar this would probably appear as a Tornado Vortex Signature. This black spot, or reflectivity minimum, coincided with the location of the tornado. As time evolved, however, an anticyclonic hook formed three or four nautical miles to the south east of the cyclonic hook (Fujita and Wakimoto, 1982).

Anticyclonic tornadoes are by no means characterized as weak. On April 4, 1981 in West Bend, Wisconsin, an 8.5 km thunderstorm spawned an F4 anticyclonic tornado. Although rare in occurrence, anticyclonic tornadoes and cyclonic-anticyclonic tornadoes like the one in Grand Island, must be included in a theory of tornado-genetic process.

Chapter 3

ANALYSIS OF THE SIMULATED STORM

3.1 Experimental Design

The Regional Atmospheric Modelling Systems (RAMS) was used to integrate the governing equations forward in time for a three dimensional numerical study of a tornadic-producing supercell thunderstorm. The grid was set up having one kilometer grid spacing in each horizontal direction and a stretched vertical grid with the lowest grid spacing equaling 25 meters and the vertical stretching ratio is 1.2 until a vertical grid spacing of 666m is obtained. The vertical grid spacing is then kept fixed at this resolution to the top of the grid domain. This choice of a stretched grid was selected to obtain high resolution from the surface to a few kilometers above model ground to capture the formation of the tornado. The horizontal domain size is 40 km in each direction and the vertical domain is 16 km. A forward time step of five seconds was chosen. The simulated event is non-hydrostatic and no radiation scheme is used. The coriolis force is turned off as it has little influence on thunderstorm morphology. The compressible continuity equation is used and a time-split acoustic scheme is turned on to handle sound waves separately to maintain computational stability. The boundary conditions used are a wall on top with seven Rayleigh friction absorption layers from the top. The lateral boundary condition is the Klemp-Wilhelmson radiation condition. The lower boundary is rigid with turbulent fluxes of heat, moisture and momentum provided by a surface layer parameterization. No soil model or vegetation is included. Any precipitation that falls on the lower boundary is removed so as to prevent any buildup. The model atmosphere is initialized horizontally homogeneously with a composite of special soundings taken May 20, 1977, the day of the Del City tornadic storm (Ray, et al, 1981). A warm bubble was placed in the center of the

lower boundary. The bubble is ten kilometers on a horizontal side and just under three kilometers deep. The temperature is 1.5K warmer and the water vapor mixing ratio is 2 g/kg greater than the environment.

3.2 Simulated Results

By 30 minutes into the simulation, the storm splitting process has already proceeded. A horizontal plot at this time, Figure 3.1, at 1095 meters, shows two distinct updraft centers. The one located at x = -7.0 kilometers and y = 5.0 kilometers has a maximum updraft speed of 4.2 meters per second. The updraft to the southeast at x = -1.0 kilometers and y = 1.0 kilometers has a maximum updraft speed of 7.8 m/s. This convective element is much stronger than its northwest counterpart and also is larger in horizontal coverage. The downdraft core located at x = -1.0 km and y = 8.0 km has a maximum downward speed of 2.4 meters per second. It looks as though the downdraft is wedging its way in between the two updrafts causing the splitting to occur, similar to the results of Schlesinger (1978), Klemp and Wilhelmson (1978a,b), Schlesinger (1980), Wilhelmson and Klemp (1981). However this is not the only process that will aid the storm splitting process. Looking at Figure 3.2, a horizontal cross section at 892 m of the horizontal vorticity vectors, shows convergence of the vortex lines at the region where the stronger updraft exist. Strong divergence in the vortex lines occurs in the location where the weaker updraft lives. Figure 3.3 shows the vertical vorticity at the same height. Positive, or cyclonic vertical vorticity is found in the region of the strong updraft and negative or anti-cyclonic vertical vorticity in the region of the weaker updraft. These two plots gives one the idea of how the vortex lines are orientated in three dimensions and explains why the strong storm is rotating cyclonically and the weaker storm is rotating anti-cyclonically. The vortex lines converge in a horizontal plane and then are tilted up by the stronger updraft generating positive vertical vorticity. Aloft the vortex lines become horizontal and then " sink " down into the weaker updraft off to the northwest of the stronger updraft. The sinking of the vortex lines causes the three dimensional vorticity vector to have a downward component. This downward pointing vorticity vector

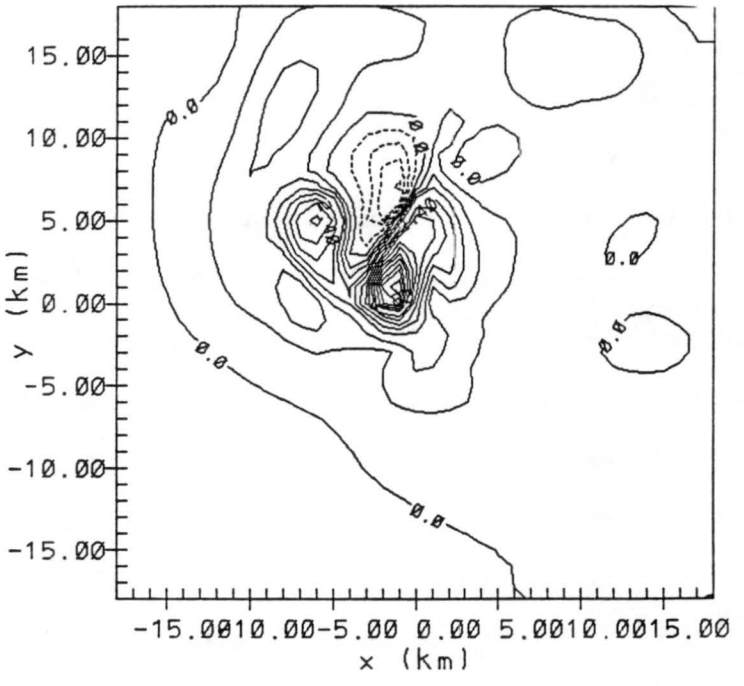

Figure 3.1: horizontal cross section of vertical speed at 1095m and 30min into the simulation. Contour interval is 0.6 m/s. The solid contours are for upward motion and dashed for downward. Maximum upward is 7.8m/s and maximum downward is 2.4m/s.

will cause the weaker storm to rotate anti-cyclonically. The vortex lines then diverge horizontally as they exit the cloud base and remain basically in a horizontal plane.

The diagnostic perturbation pressure equation, to be derived in Chapter 4, indicates that a region characterized by a large magnitude of the three dimensional vorticity, of either sign, relative to its neighborhood, and exceeds the magnitude of the strain rate, will have lower pressure. By examining figures two and three, one sees that the volume of updraft has a larger magnitude of three dimensional vorticity. It should not be surprising to see this on Figure 3.4, a horizontal cross section at 1095 meters of the perturbation pressure. The larger pressure minimum at x = 0.0 kilometers and y = 1.0 kilometers is correlated well with the location of the stronger updraft and the region of positive vertical

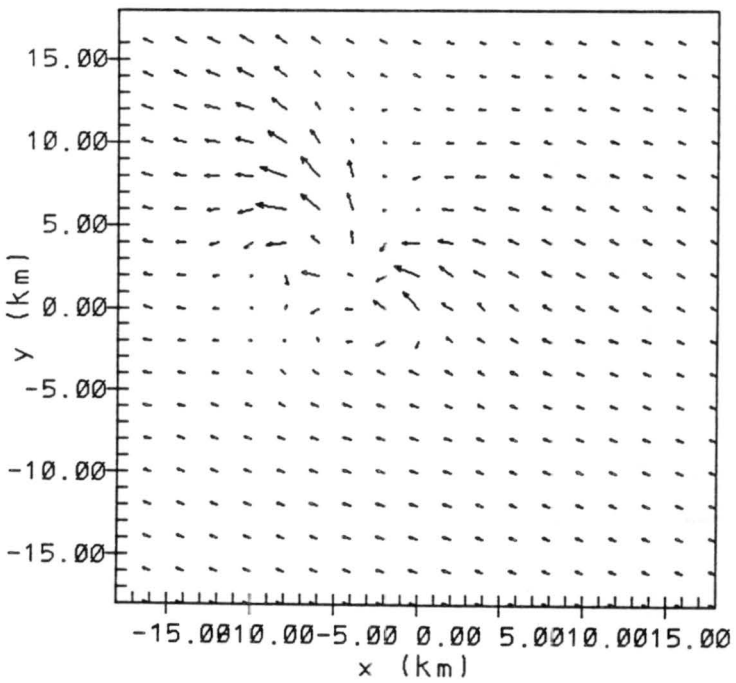

Figure 3.2: horizontal cross section of the horizontal vorticity vectors at 892m and 30min into the simulation. The maximum vector is $0.24s^{-1}$.

vorticity and large horizontal vorticity vectors. The weaker pressure minimum located at x = -5.0 kilometers and y = 6.0 kilometers is actually on the gradient of the updraft to the north of the weaker updraft core. The pressure maximum located at x = -3.0 kilometers and y = -1.0 kilometers is associated with the environmental flow diverging around the two updraft elements, analogous to obstacle flow. The northern pressure maximum is associated with the convergence of the flow to the north of the two updraft elements. In the diagnostic equation for perturbation pressure, the first term, the strain rate squared, is always associated with a perturbation high. As both a divergent and a convergent flow field are characterized by large strain rates the perturbation pressures in these regions will be high. Figure 3.5, a horizontal cross section at 1095 meters of the horizontal wind

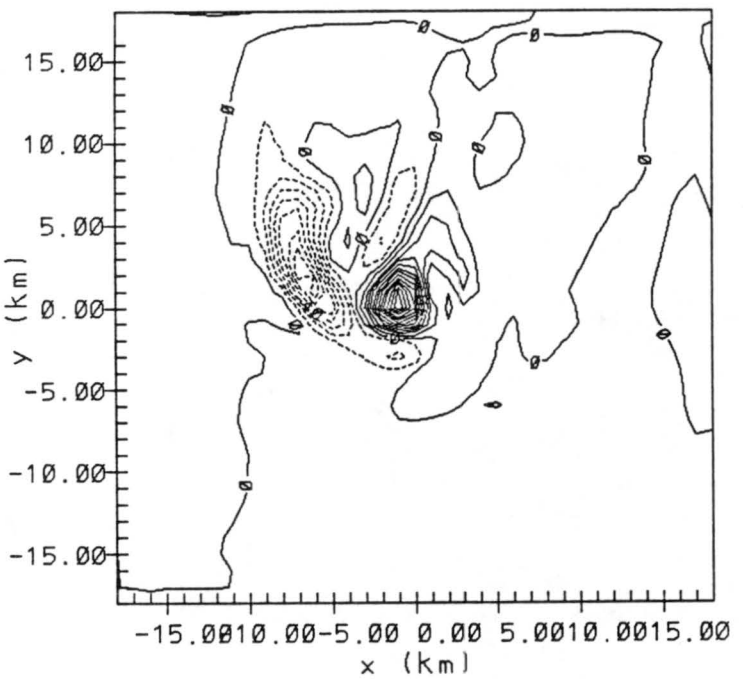

Figure 3.3: horizontal cross section of vertical vorticity at 892m and 30min into the simulation. Solid contour depict positive vorticity and dashed negative vorticity. The maximum positive and negative values are respectively $0.12s^{-1}$, $-0.07s^{-1}$.

vectors, shows that these perturbation highs are indeed associated with divergent and convergent flows to the south and north of the the two updrafts respectively.

Note in Figure 3.5, that the environmental wind, relative to the convective elements is flowing to the south, directly between the two updrafts. This suggests that dry environmental air is being efficiently entrained into the young convective elements and aiding the downdraft in splitting the storm into two distinct members by evaporating cloud material as a consequence of entrainment (Schlesinger, 1980).

Figure 3.6, a horizontal cross section at 1095 meters of rain water mixing ratio, shows that the rain is correlated well in location with the down draft. This supports the idea that initial storm splitting is the result of two processes; a rain driven downdraft and

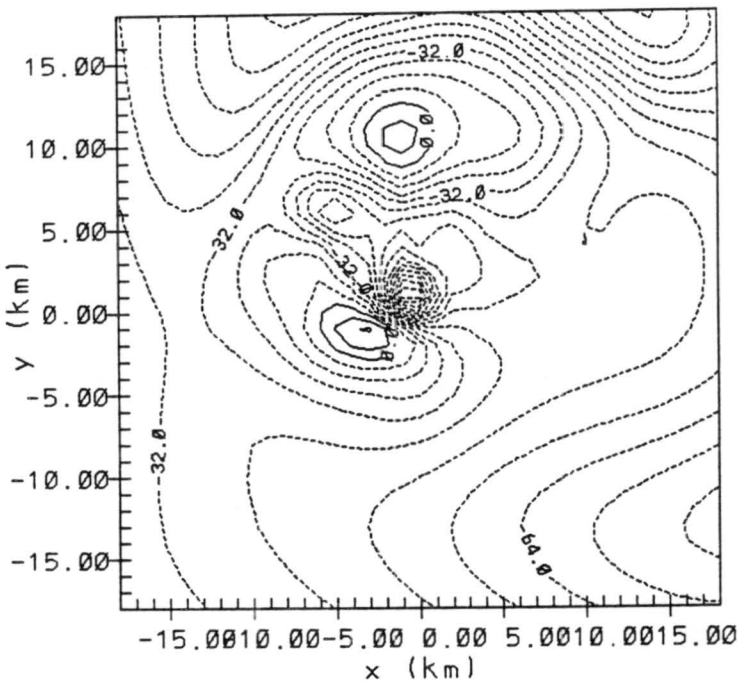

Figure 3.4: horizontal cross section of perturbation pressure at 1095m and 30min into the simulation. The contour interval is 8.0 pa.Solid contours are excesses and dashed deficits. The maximum excess is 16.0 pa and -112.0 pa for the deficit.

entrainment of dry environmental air into the convective element that aids in evaporating cloud in the same general location of the downdraft (Schlesinger, 1980).

Referring to Figure 3.1, as the simulation is run forward in time, the left and weaker updraft moves quickly to the northwest. A mean wind vector is subtracted from the environmental wind to keep the strong updraft centered in the grid.

Recall that the time step is five seconds, the simulation was allowed to run forward to ninety minutes when it was decided to spawn two finer grids. The reasoning for this was that observationally, it is known that rotating storms produced tornadoes roughly two hours after the first radar echo appeared. The physics necessary for tornado-genesis, numerically, must be captured for a sufficient time before the expected time of tornado-

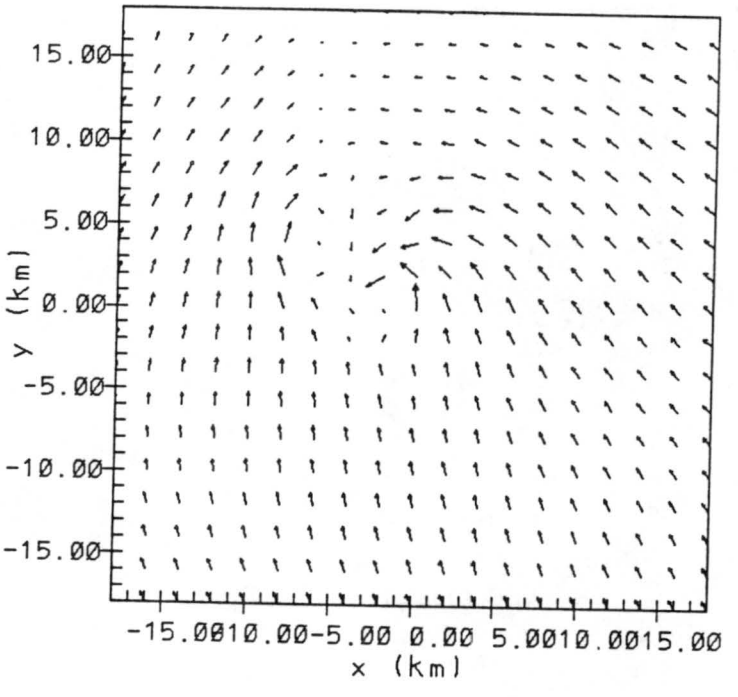

Figure 3.5: horizontal cross section of the horizontal component of wind at 1095m and 30min into the simulation. The maximum wind vector is 15.4 m/s.

genesis. Sufficient time is not cut and dry, so adding the finer interactive grids thirty minutes prior to the expected time of tornado formation was done in the hope that thirty minutes of high resolution calculation was sufficient to allow the simulated storm to generate the processes responsible for the formation of a tornado.

Grid two is ten kilometers on a horizontal side with a grid spacing of 333m. The vertical spacing is the same as the first coarser grid. The third interactive grid is four kilometers on a horizontal side with a grid spacing of 111m. The vertical grid spacing again is the same as the first grid.

Due to the increased horizontal resolution the time step had to be reduced so as to prevent computational instabilities from growing. The first grid has a new time step of

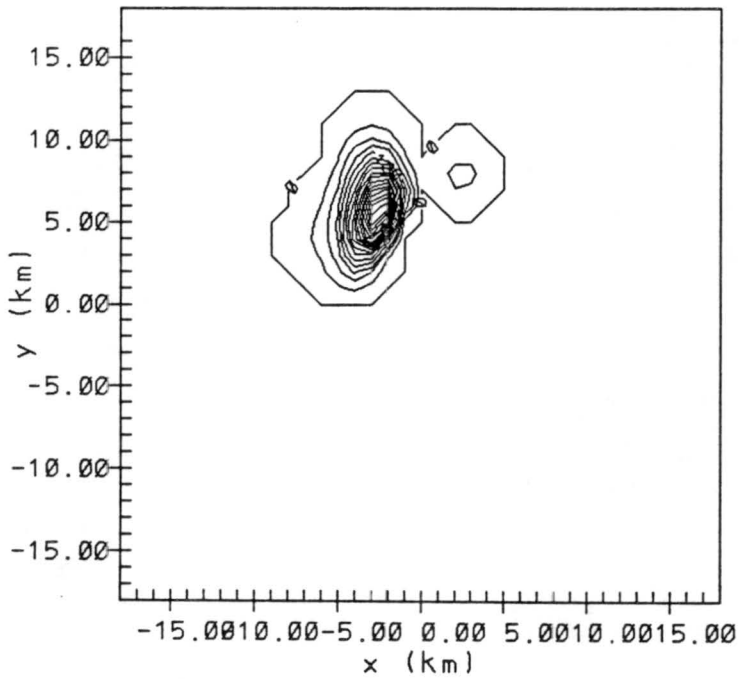

Figure 3.6: horizontal cross section of rain mixing ratio at 1095m and 30min into the simulation. The contour interval is 0.03 g/kg and the maximum is 0.48 g/kg.

one second, the second finer grid has a time step of one third of a second and finally the third finest grid has a time step of one ninth of a second. The model was allowed to run for just sixty seconds when the three dimensional fields were stored for future analysis. The model was started up again and allowed to run for another sixty seconds to store the fields. This process was continued for the next seventeen simulated minutes. Each one minute run required twelve hours of real time on the Stardent 3040 RISC workstation.

With the high resolution grids running for five minutes, Figure 3.7, an east west vertical cut just to the north of the cloud base updraft center, shows a conspicuous updraft and downdraft feature. The main updraft extends to just below 14 km above ground level. The maximum updraft for this cross section is at 9 km and is 45 m/s. The updraft also exhibits a well-observed feature, the eastward lean with height of some 5 km

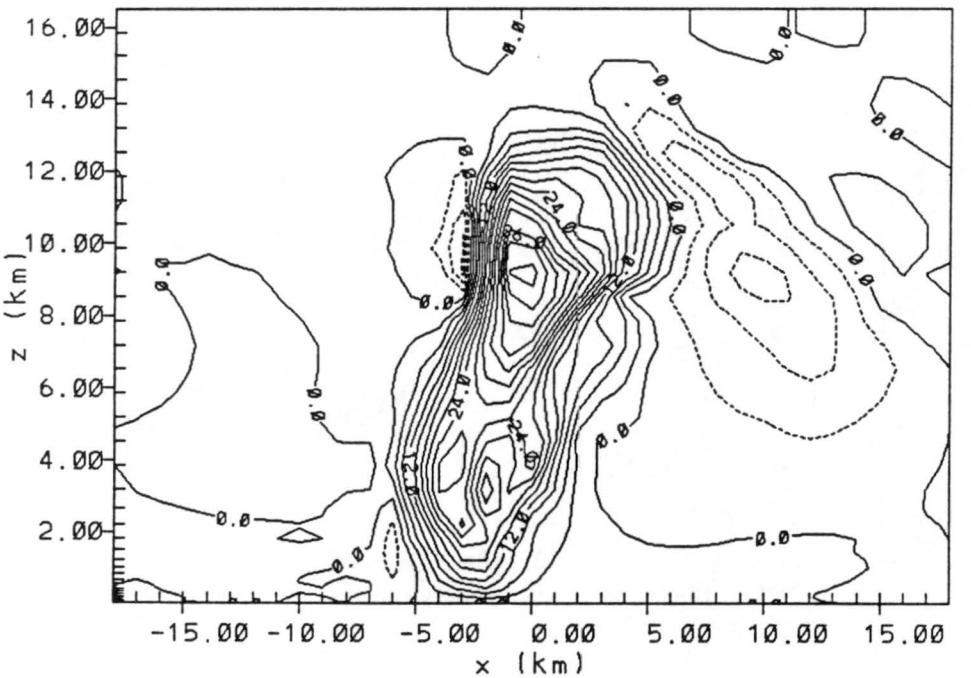

Figure 3.7: Vertical cross section of vertical motion at y = -1.0 km and at 95min into the simulation. The contour interval is 3.0 m/s. The solid contour is upward motion and the dashed is downward. The maximum upward is 45.0 m/s and 9.0 m/s for the maximum downward.

in the horizontal direction. The main downdraft on this figure is a result of hydrometeors being ejected out of the top of the storm where the anvil canopy is forming. The largest downward vertical speed is reached at 9 km and is 9 m/s. A smaller downdraft to the west of the main updraft at 10 km appears to be forced by the vertical perturbation pressure gradient. This downdraft is void of any buoyancy forcing. The very small low-level downdraft to the west of the updraft just below two kilometers is in response to the precipitation field.

The perturbation pressure field for the same vertical cross section as in Figure 3.7 is seen in Figure 3.8. Note that a very large percentage of the main updraft at this time

is characterized by low pressure. The lowest pressure is found at roughly a few hundred meters above cloud base with a magnitude of 5.2 mb deficit. This low-level pressure deficit

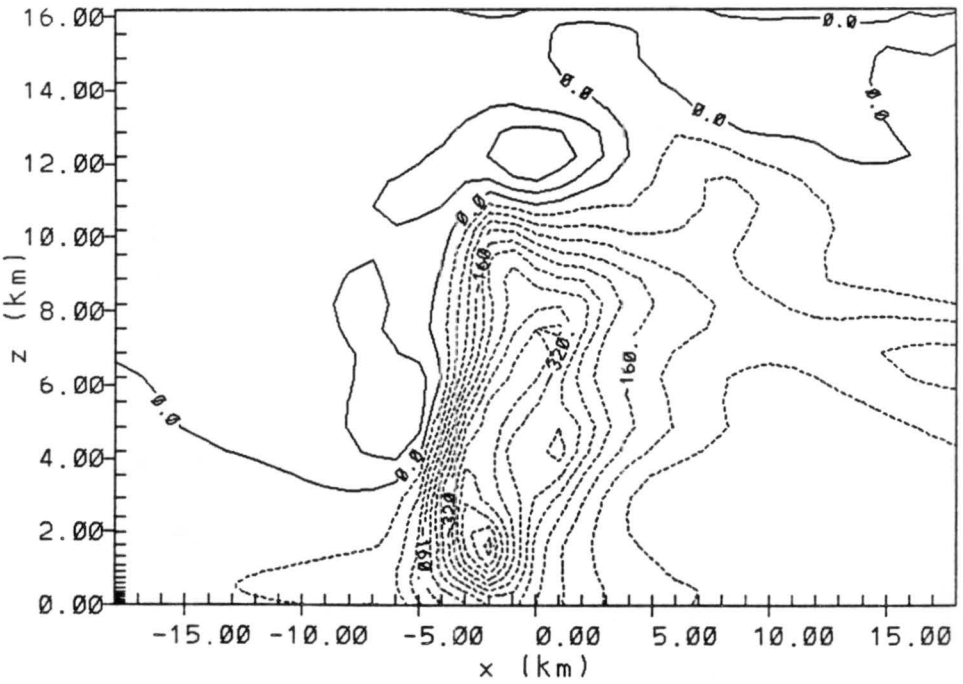

Figure 3.8: Same as Fig. 7 for the perturbation pressure. The contour interval is 40.0 pa. The pressure excess is represented by solid contours and the pressure deficit by dashed. The maximum deficit is 520.0 pa and the maximum excess is 80.0 pa.

will be examined in detail in the next section where tornado-genesis is discussed. The action of the updraft interacting with the tropopause causes the wind field to be highly divergent. In the diagnostic equation for pressure, this type of flow field is characterized by high pressure. Note also that the west side of the updraft is also a region of high pressure, it is proposed that this is due to the environmental wind flowing around the convective element analogous to obstacle flow (Cotton and Tripoli,1978). The low-level perturbation low alone provides an acceleration that will allow sub-cloud air to achieve updraft speeds of 4 m/s just below cloud base in just under thirty seconds!

The perturbation temperature field for the same vertical cross section as in the last two figures is shown in Figure 3.9. The conspicuous feature is the warm column that extends from 2 km above ground level to 12 km capped by a very large cold dome. The maximum temperature excess is 9 K located just above 6 km or roughly the mid levels of the storm. It should be mentioned that simply using a skew-T log-P diagram

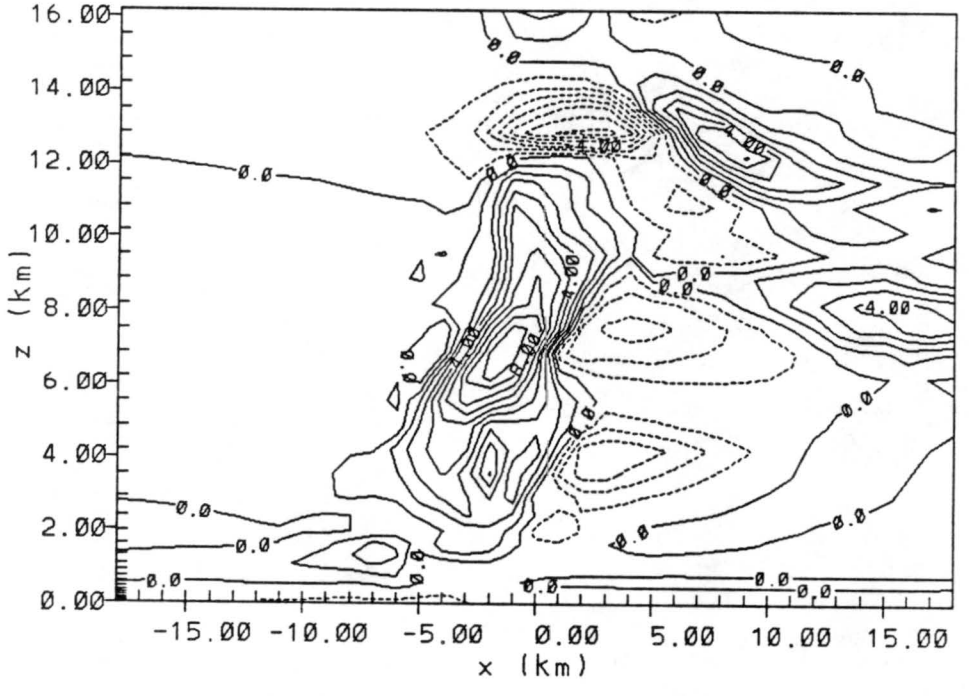

Figure 3.9: Same as Fig. 7 for the perturbation temperature field. The contour interval is 1.0 C. The temperature excess is denoted by solid contours and the deficit by dashed. The maximum temperature excess is 9.0 C and the maximum deficit -7.0 C.

to estimate the temperature excess available to the storm will be an under estimate due to the fact that the moist adiabats do not take into account the heat release due to the ice deposition/freezing process. Entrainment can reduce the temperature excess thus compensating to some degree for the neglect of the ice-phase heating. The upper-level

cold pocket located on top of the updraft is the so-called overshooting top of the updraft. This air will quickly find itself colder than it's environment.

The hydrometer fields are shown in Figures 3.10 through 3.13 for the same vertical cross section as the above figures. Figure 3.10 shows the rain mixing ratio field. Note the distinct downshear lean with height this field shows. The low level maximum of 10 g/kg is just above the vault or weak echo region located between x = -5.0 km and x = -1.0 km and bounded above at the z = 3.0 km. Located 10 km above ground is a secondary maximum of 6.0 g/kg. When compared to the vertical motion field one sees that the low level downdraft located at x = -6.0 kilometers and below 2.0 kilometers is correlated nicely with the rain field on Figure 3.10. The echo free vault is also filled with updraft as would be expected.

The graupel field shown in Figure 3.11 is found in the upper levels of the storm where it leaves the main updraft and is ejected out where the strong environmental winds can carry them down stream. As will be shown, for this vertical cross section, the upper level cut is on the southern side of the storm due to its lean with height. As the graupel has a non-negligible fall speed, the field shows the downward slope with increasing distance downstream.

Figure 3.12 shows the pristine ice mixing ratio field is quite different from the graupel field; being more horizontal with increasing distance downstream from the updraft. This is a reflection of the weak fall speed for this species. Figure 3.13 shows the aggregate field and indicates that this field is not formed in this particular cross section.

Shown in Figure 3.14 is a horizontal cross section at 1095 meters AGL, approximately cloud base, of the vertical motion field. The updraft is generally comma shaped with the maximum updraft speed of 30 m/s in the core. Two distinct downdrafts are seen, one located to the west, associated with the precipitation and has a magnitude of 4 m/s. A smaller downdraft directly to the south of the updraft is not associated with the precipitation field. The magnitude of this downdraft is also 4 m/s.

The horizontal wind components, shown in Figure 3.15, for the same height as the last figure shows the inflow region to be to the east and southeast of the main updraft. The

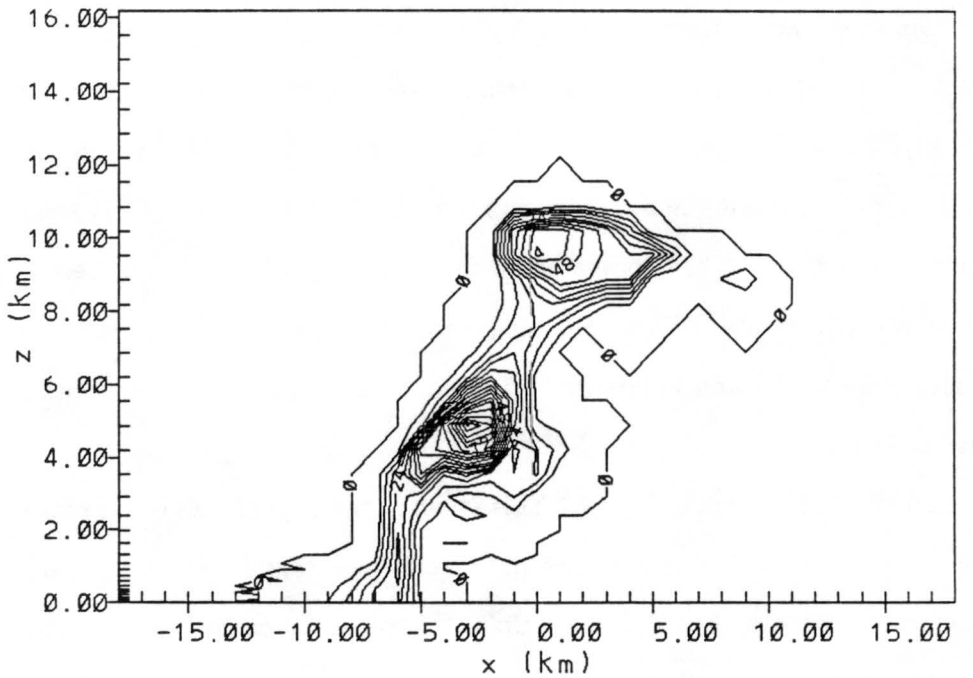

Figure 3.10: Same as in Fig. 7 for the rain mixing ratio field. The contour interval is 0.6 g/kg. The maximum value is 10.2 g/kg.

environmental air from the east and southeast converges and accelerates into the storm continually supplying warm moist air. Of particular interest is the deformation field located roughly at x = -4.0 km and y = -4.0 km. This field is associated with the small downdraft located to the south of the main updraft and gives the updraft the appearance of a comma. This " clear slot " is a common feature with supercell thunderstorms (see Chapter 18 in Mesoscale Meteorology and Forecasting by Peter Ray, editor). The author has observed this feature. Being located directly underneath this region and looking at the updraft field directly to the east of this small downdraft, located on Figure 3.14 from y = -1.0 km to y = -6.0 km at x = -2.0 kilometers, one notices that the western side of the cumulus is sinking rapidly. The deformation pattern can be visually detected in real storms by looking at the cloud tags at cloud base to the northwest and to the southeast.

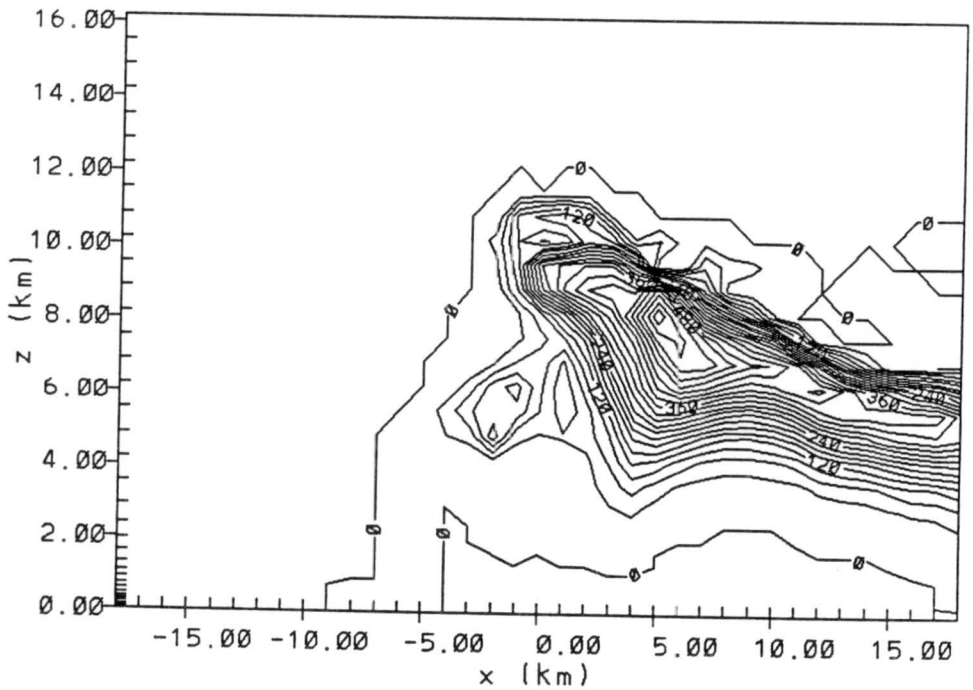

Figure 3.11: Same as Fig. 7 for the graupel field. The contour interval is 0.3 g/kg. The maximum value is 6.0 g/kg.

Figure 3.16, shows the rain mixing ratio at cloud base. The most conspicuous feature is the " hook " appearance. This feature on radar would more than likely cause the National Weather Service to issue a tornado warning. By comparing this field with the vertical motion field one sees that the updraft is void of rain! The southern hook appendage is to the northwest of the smaller downdraft and intrudes into the updraft a bit. The maximum liquid water content is located to the northwest and west of the updraft. The main downdraft is correlated perfectly with this rain field. The region bordered by the rain field to the north , west, and to the south by the hook is the weak echo region and is an indication of a strong updraft. The graupel field is not shown but it is generally located to the north of the updraft with its southern extent around y = 2.0 km and runs east west from x = -6.0 km to x = 4.0 km.

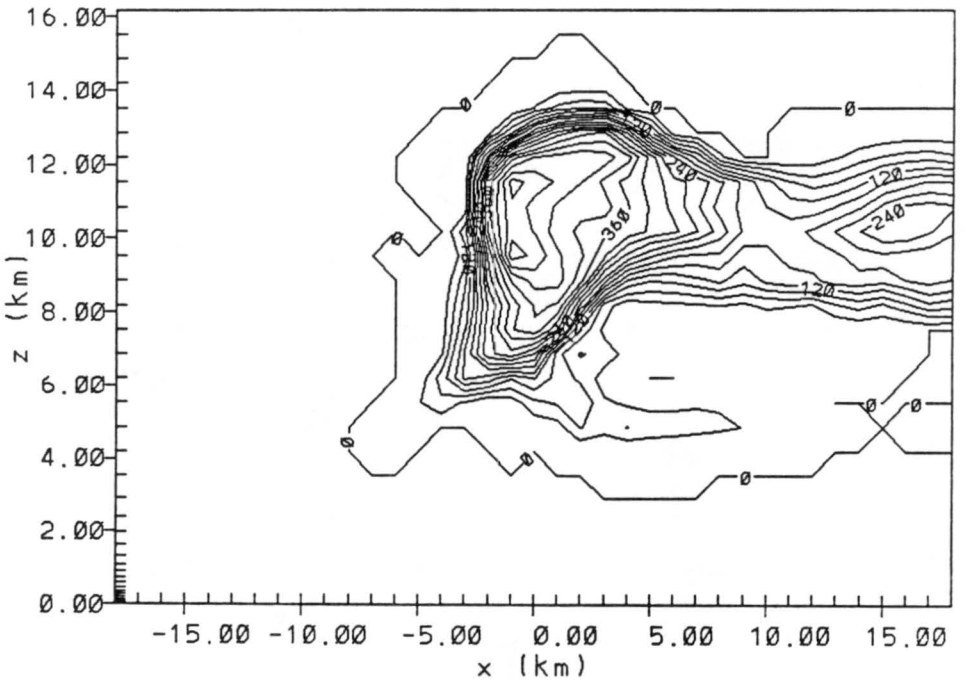

Figure 3.12: Same as Fig. 7 for the pristine ice mixing ratio field. The contour interval is 0.3 g/kg. The maximum value is 4.8 g/kg.

The vertical motion field at 3528 m above ground level is shown in Figure 3.17. Two well-defined updrafts are observed with both having the same maximum updraft speed of 30 m/s. The western updraft is larger and has a strong cyclonic rotation. The downdraft at this level is to the north and northeast of the updraft with a magnitude of 4 m/s to the north and 8 m/s to the northeast.

Environmental air from the southwest is turned cyclonically around the updraft field (Figure 3.18) to the east then to the northern flanks. The conspicuous swirl centered at x = -4.0 km and y = -1.0 km is associated with the western updraft. Note the high correlation between the updraft maximum and the location of the center of the swirl. The eastern updraft does not have any organized rotation as seen in the horizontal wind field.

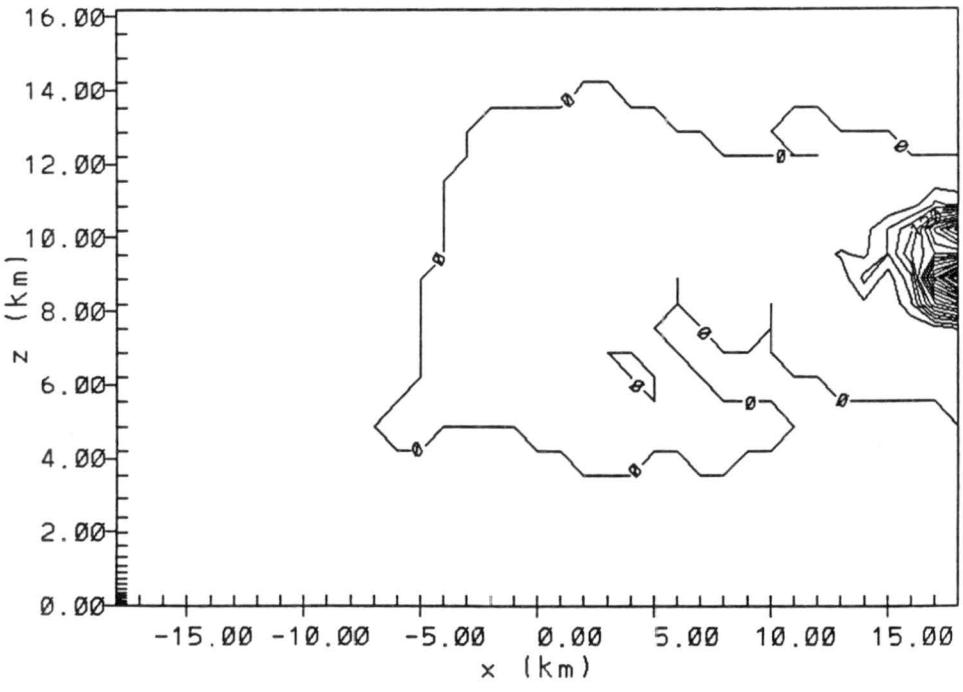

Figure 3.13: Same as Fig. 7 for the aggregate mixing ratio field. The contour interval is 0.03 g/kg. The maximum value is 0.54 g/kg.

The rain mixing ratio field for this level is shown in Figure 3.19. Unlike the rain field at cloud base, the updrafts are completely filled with rain. Notice however, at x = -4.0 km and y = -1.0 km, that the smallest closed contour is a minimum in the local rain field. This minimum is bounded on all sides with higher and large gradients of rain and is called the bounded weak echo region. This is another signature of a dangerous thunderstorm. The graupel field is similar to the one at cloud base, just shifted to the east by about two kilometers and south by one kilometers.

Figure 3.20, a horizontal cross section of vertical velocity at 6865 meters, shows that there is just one main updraft at this level. The maximum updraft speeds are 42 m/s but this does not occur in the interior of the storm. Upon close inspection, one sees that

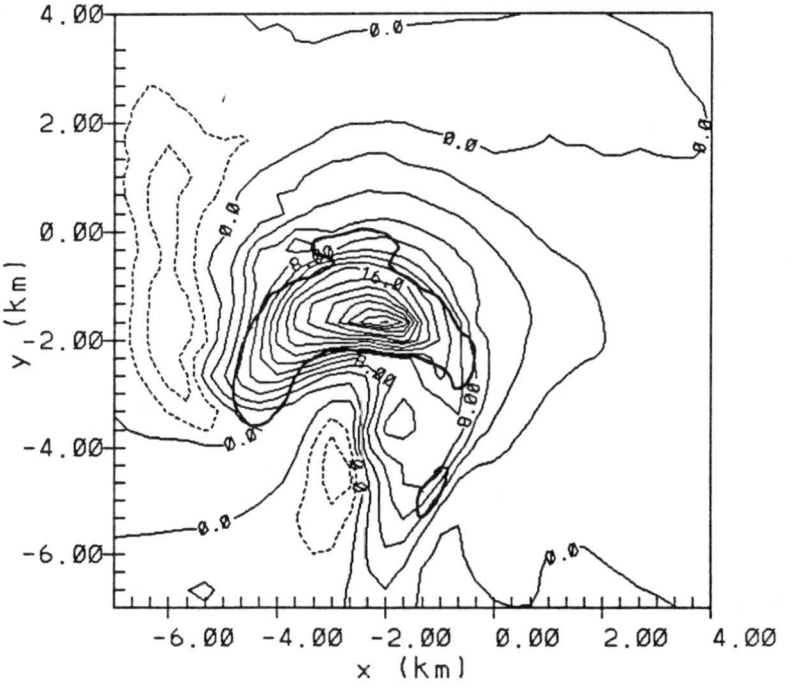

Figure 3.14: Horizontal cross section of vertical motion at 1095m and 95min into the simulation. The contour interval is 2.0 m/s. The contouring is the same as in Fig. 1. The maximum upward motion is 30.0 m/s and the maximum downward is -4.0 m/s. The dark solid depicts the boundary, vertical vorticity of $0.01s^{-1}$,of the mesocyclone.

the interior of the updraft has weaker upward vertical speeds. The inner most contour is the isoline of 24 m/s.

Environmental wind (Figure 3.21) approaches the storm from the west and splits into two flows that move around the updraft, again reminiscent of obstacle-like flow. The southern branch is stronger with wind speed reaching 40 m/s. The area occupied by the updraft shows very little horizontal wind and no noticeable rotation. This implies that the bulk of the kinetic energy is not in rotation, but rather in the ascending flow of the updraft. At lower levels the rotational component of the wind makes a significant contribution to the total kinetic energy of the flow.

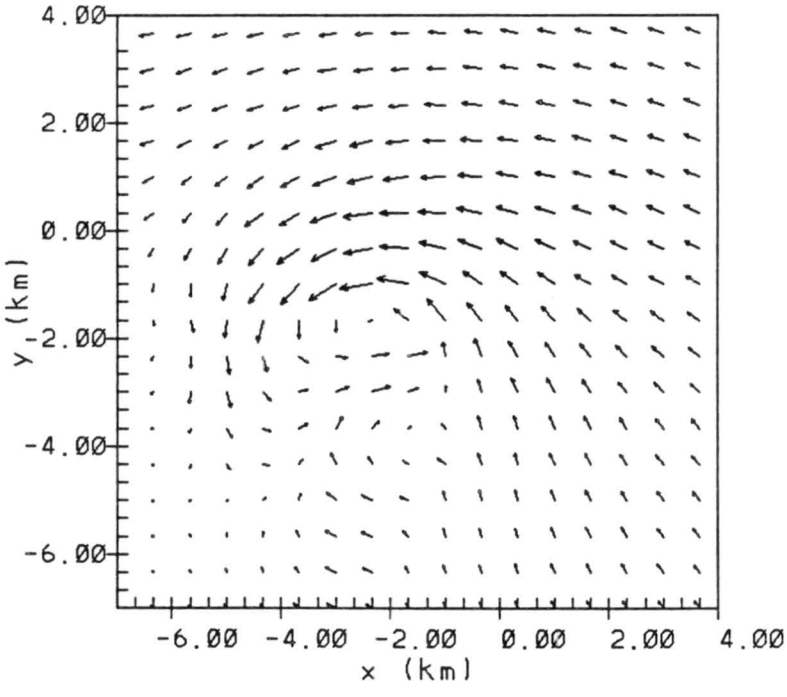

Figure 3.15: horizontal cross section of the horizontal wind vectors at 1095m and 95min into the simulation. The maximum wind vector is 28.0 m/s.

The rain mixing ratio field shown in Figure 3.22 is, interestingly enough, completely bounded on the western, southwestern and southern edges by the large horizontal gradient of upward motion. This clearly indicates that the rain field is contributing to a drag force that is retarding the updraft. Note how the horizontal gradient of updraft weakens considerably where the maximum rain mixing ratio is.

Graupel at this level is displaced a little to the north of the rain field, as shown in Figure 3.23. The maximum graupel mixing ratio, however, is just to the north of the minimum in the updraft. It seems that the combined fields of rain and graupel may have resulted in the minimum upward vertical motion in the interior of the updraft due to drag forces.

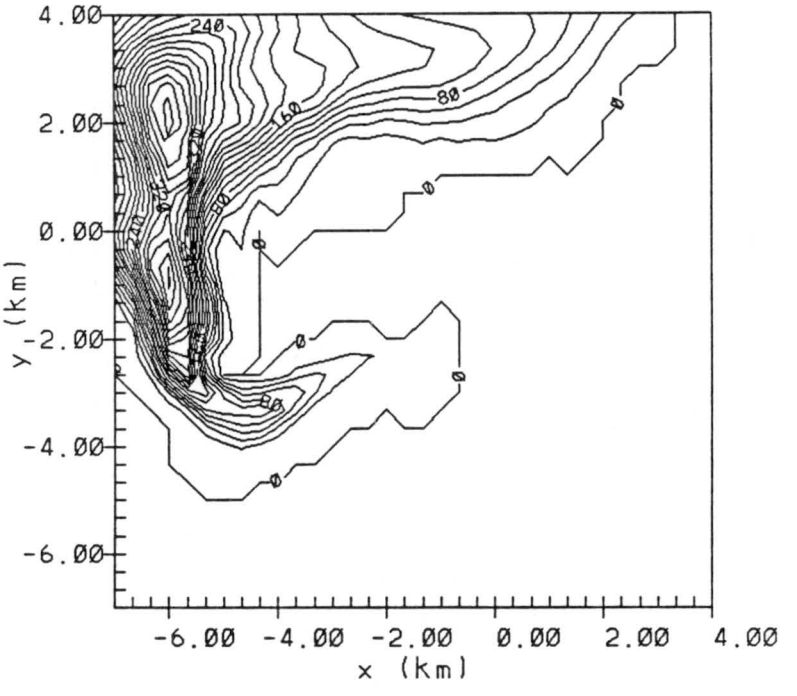

Figure 3.16: horizontal cross section of rain mixing ratio depicting the hook echo. The contour interval is 0.2 g/kg. The maximum value is 42.0 g/kg.

Pristine ice, shown in Figure 3.24, makes up the bulk of the cloud wall. By comparing this figure with the past ones, the pristine ice gradients are correlated well with the gradients of upward vertical motion. In fact this ice field also shows a minimum interior to the storm.

Ten minutes later into the simulation Figure 3.25 shows a vertical cut of the vertical motion field roughly through the center of the storm at cloud base. Again, a mean horizontal wind vector was subtracted to keep the storm in the middle of the grids, therefore the winds are storm relative. Comparing this figure to Figure 3.7, the most obvious difference is the top of the updraft. The storm top has collapsed resulting in a three kilometer depression. The air is sinking in this depression with a magnitude up to 8 m/s. At this time in the simulation, there is a tornado on the ground and it's at its

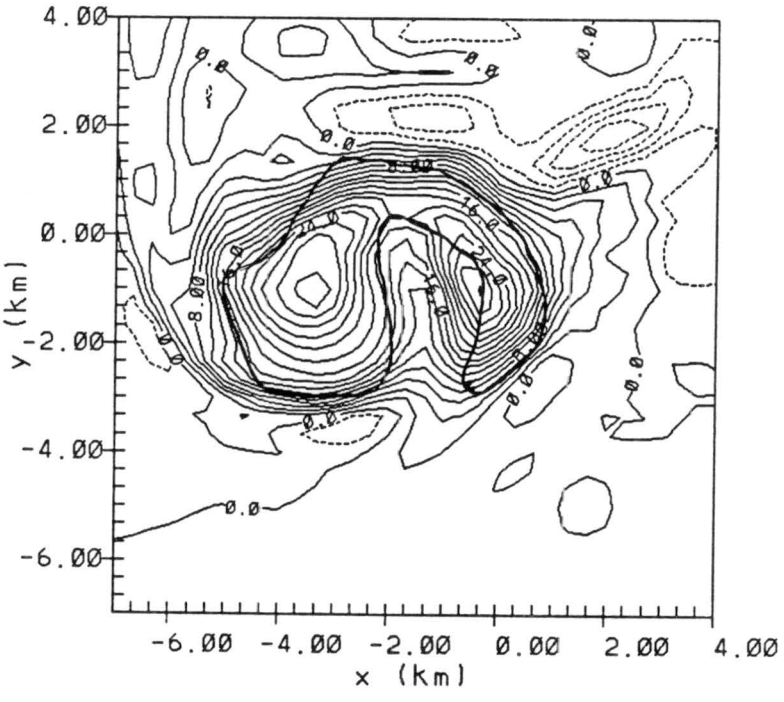

Figure 3.17: horizontal cross section of vertical motion at 3528m and 95min into the simulation. The contour interval is 2.0 m/s. The maximum upward motion is 30.0 m/s and the maximum downward is -8.0 m/s. The boundary of the mesocyclone is shown by the dark solid contour.

maximum intensity. The cause of the overshooting top collapsing is not investigated here, however, Fujita observed this feature by flying over the thunderstorms and noting that when a tornado is on the ground the top collapses and a depression at cloud top results. One can't help but wonder what role if any does the physics of tornado-genesis play in the occurrence of collapsing an overshooting top.

The other features evident in Figure 3.7 are also apparent in this figure with the exception of a new downdraft located at x = - 2.0 km and z = 1.0 km. This downdraft is completely surrounded by updraft in this cut and is associated with the low-level

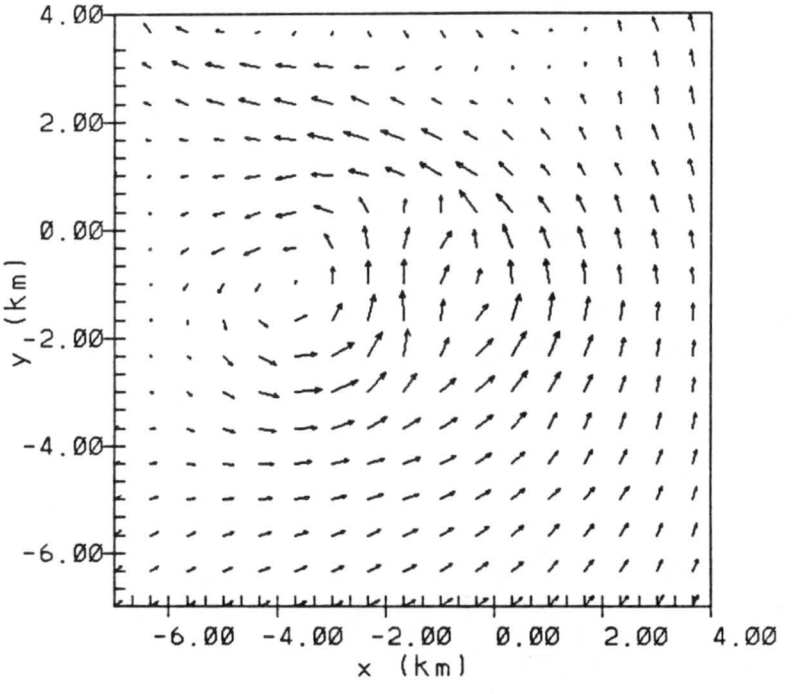

Figure 3.18: horizontal cross section of horizontal wind vectors at 3528m and 95min into the simulation. The maximum vector is 29.5 m/s.

mesocyclone. The maximum upward vertical speed in the updraft is 34 m/s and is weaker than the maximum in Figure 3.7.

Figure 3.26, shows the perturbation pressure field which should be compared to Figure 3.8. The perturbation high found on top of the updraft in Figure 3.8 is not present in Figure 3.26. A well-defined pressure minimum is located in the storm at just under z = 6.0 km. Another well-defined low is located at x = -2.0 km and z = 1.0 km. This low is surrounded by a strong pressure gradient, as a result, air from below as well as from above will be accelerated into this region. The location of this low and the downdraft in the mesocyclone is well correlated. One can not conclude, yet, that this vertical pressure gradient is causing the downdraft in the mesocyclone. One must make sure that buoyant effects are not strong enough to overcome the pressure forcing.

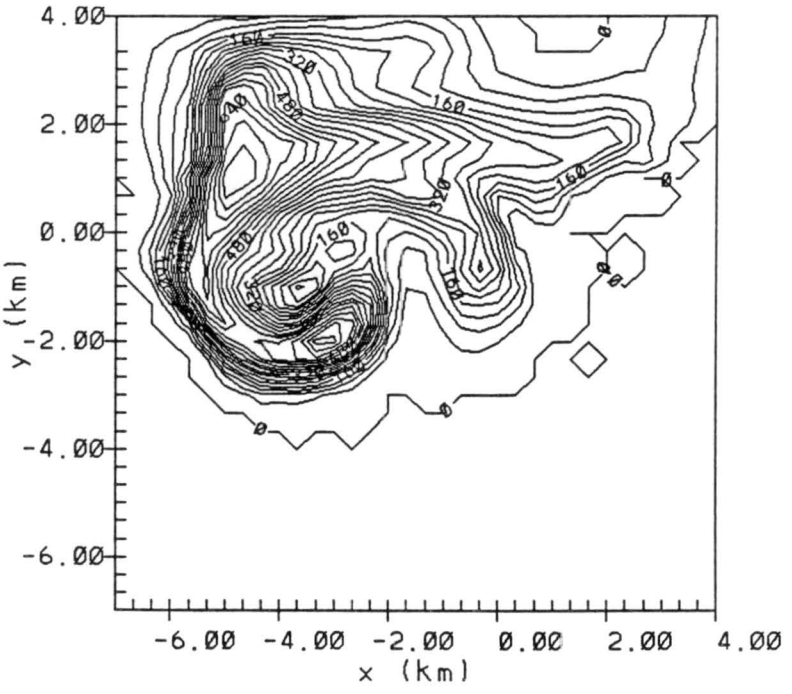

Figure 3.19: horizontal cross section of rain mixing ratio showing the bounded weak echo region at 3528m and 95min into the simulation. The contour interval is 0.4 g/kg. The maximum value is 7.6 g/kg.

The magnitude of the perturbation low is 5.4 mb, comparable to Figure 3.8. However, the vertical perturbation pressure gradient is stronger at this time than it is ten minutes earlier.

By examining Figure 3.27, the perturbation temperature field, one sees that at x = -2.0 kilometers and z = 1.0 kilometer that the air is close to to being neutrally buoyant. Therefore one can conclude that the downdraft in the mesocyclone is caused by the vertical perturbation pressure gradient force. The basic features of Figure 3.9 are also exhibited in Figure 3.27. The maximum temperature excess is 8.1 K comparable to earlier times of 9.0 K.

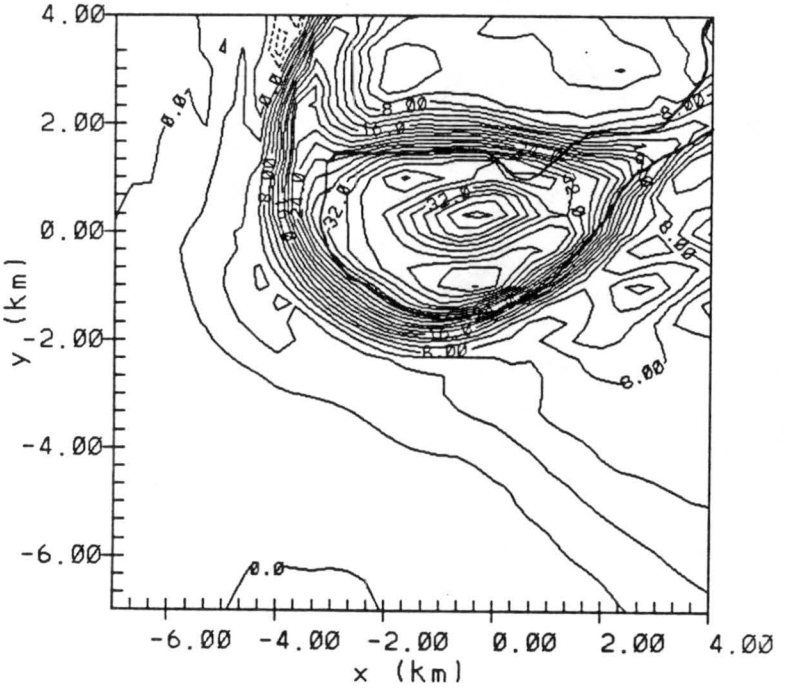

Figure 3.20: horizontal cross section of vertical motion at 6865m and 95min into the simulation. The contour interval is 2.0 m/s. Solid contours are for upward motion. The maximum upward motion is 42.0 m/s.

The rain mixing ratio field, shown in Figure 3.28, is much different than in Figure 3.10. A conspicuous feature is the lack of a double maximum at 105 min compared to 95 min and the height of the rain field does not reach as high as in earlier times. The field continues to display an eastward slope with height. The maximum mixing ratio for this vertical cross section is 6.0 g/kg. In Figure 3.10 the rain field at the surface is between x = -5.0 and -9.0 km and in Figure 3.28 it is between x = -3.0 and -6.0 km. This should not be viewed as a progression of the rain field but rather the result of subtracting out a mean horizontal wind in an attempt to keep the storm in the middle of the grids.

Compared to Figure 3.11, the graupel mixing ratios ten minutes later, shown in Figure 3.29, are very small. The field also does not reach as high as in earlier times. The

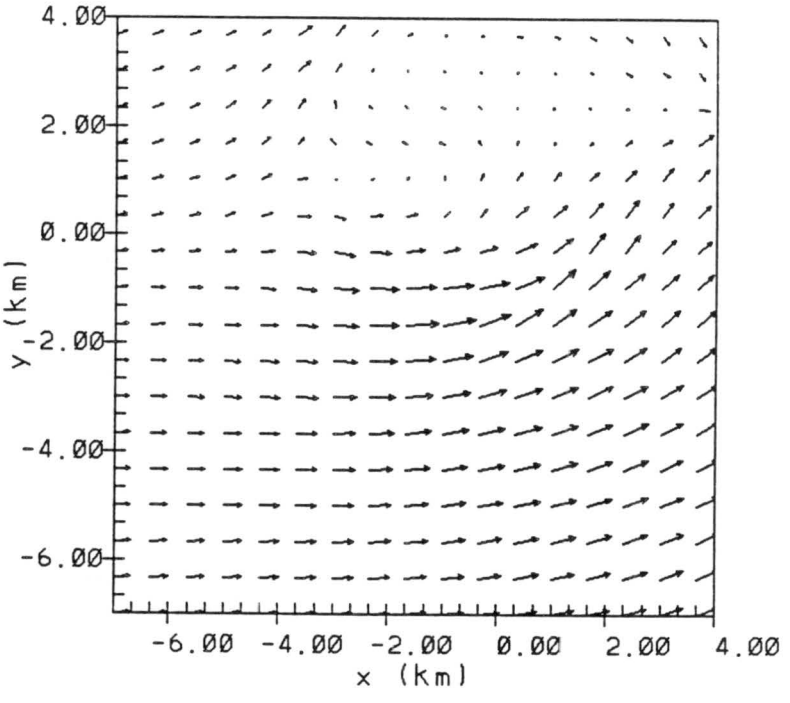

Figure 3.21: horizontal cross section of horizontal wind vectors at 6865m and 95min into the simulation. The largest wind vector is 40.9 m/s.

eastward slope with decreasing height is still preserved. The maximum mixing ratio for this cut is 4.8 g/kg, slightly less than in Figure 3.11.

Pristine ice crystal concentrations in the anvil, shown in Figure 3.30, are comparable to Figure 3.12, both exhibiting similar features. The only difference is in the vertical thickness in the field downstream. Notice in Figure 3.12 at x = 10.0 km, that the anvil is thinner and lower compared to Figure 3.30 at x = 10.0 km.

The aggregate field is dramatically different. Compare Figure 3.13 with Figure 3.31. In Figure 3.13, recall, it looked as though that cut intersected the aggregate field where the source is not in this plane. In Figure 3.31, however, it looks like the source of aggregates is in this plane. It's possible that in subtracting the mean wind the storm was simply

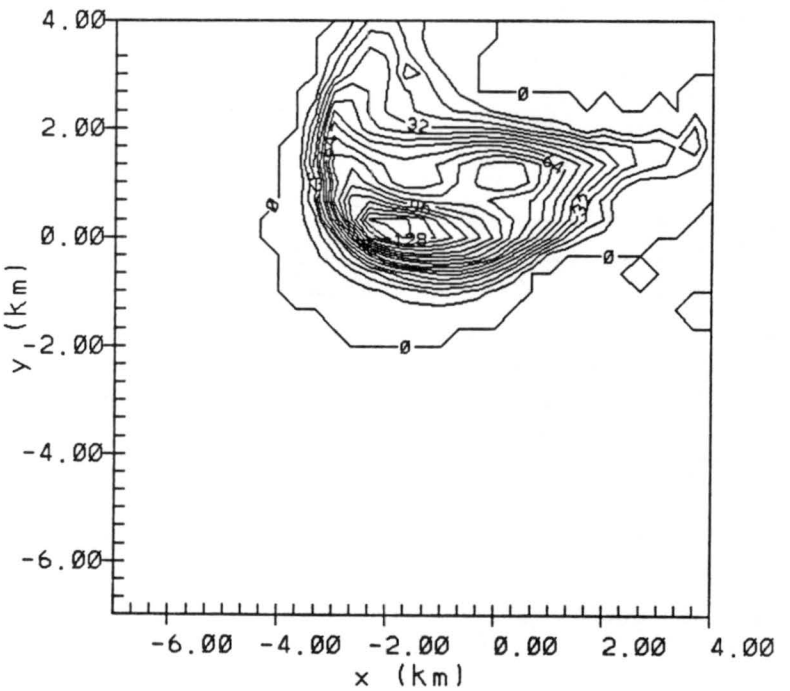

Figure 3.22: horizontal cross section of rain mixing ratio at 6865m and 95min into the simulation. The contour interval is 0.8 g/kg. The maximum value is 13.6 g/kg.

shifted within the grids so as to put the source region in this particular cut and not the generation of a new source. A horizontal cross section in the upper levels of the storm at these two times will answer that question.

A horizontal cross section at 1095 m and 105 min of the vertical motion field shows a horseshoe-shaped updraft with two regions of strong upward vertical motion. The weaker one located at x = -1.0 km and y = -2.0 km with a magnitude of 22 m/s and a stronger one located just to the west at x = -2.0 km, y = -2.0 km with a magnitude of 28 m/s. The updraft bounds a downdraft with a magnitude of 12 m/s. As shown in Figure 3.25, this downdraft does not have a large vertical depth and as was pointed out earlier is associated with the mesocyclone. The downdraft is larger in areal extent as compared to 10 min earlier in Figure 3.14 and has a larger magnitude. The downdraft in Figure

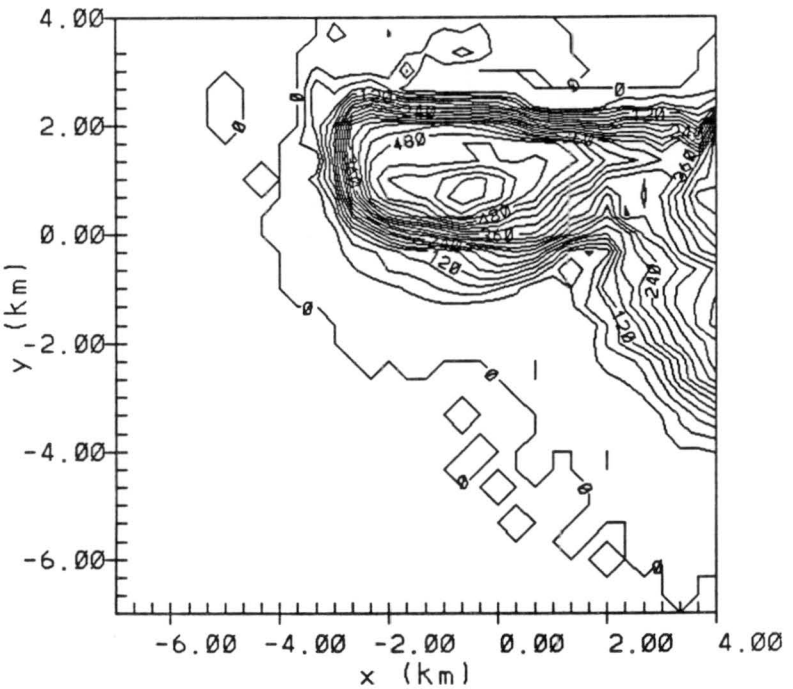

Figure 3.23: horizontal cross section of graupel mixing ratio at 6865m and 95min into the simulation. The contour interval is 0.3 g/kg. The maximum value is 6.0 g/kg.

3.14 located to the south of the main updraft is almost non-existent in Figure 3.32, only a weak and small signature is seen at x = -1.5 km and y = -4.0 km.

The horizontal component of the wind field is shown in Figure 3.33. It is similar to the wind field ten minutes earlier as seen in Figure 3.15. The environmental winds come in from the southeast and east, converge and flow cyclonically to the north of the updraft. However, important differences are seen. In Figure 3.33, the circular wind pattern appears strongly divergent, particularly at x = -2.5 km, y = -2.0 km. This divergent pattern is not seen in Figure 3.15. Also lacking in Figure 3.33 is the deformation field that was pointed out in Figure 3.15 at x = -4.0 km and y = -4.0 km.

The rain mixing ratio in Figure 3.34 shows that an appendage is still clearly apparent. The mixing ratio has increased since 10 min earlier as seen in Figure 3.16. The largest

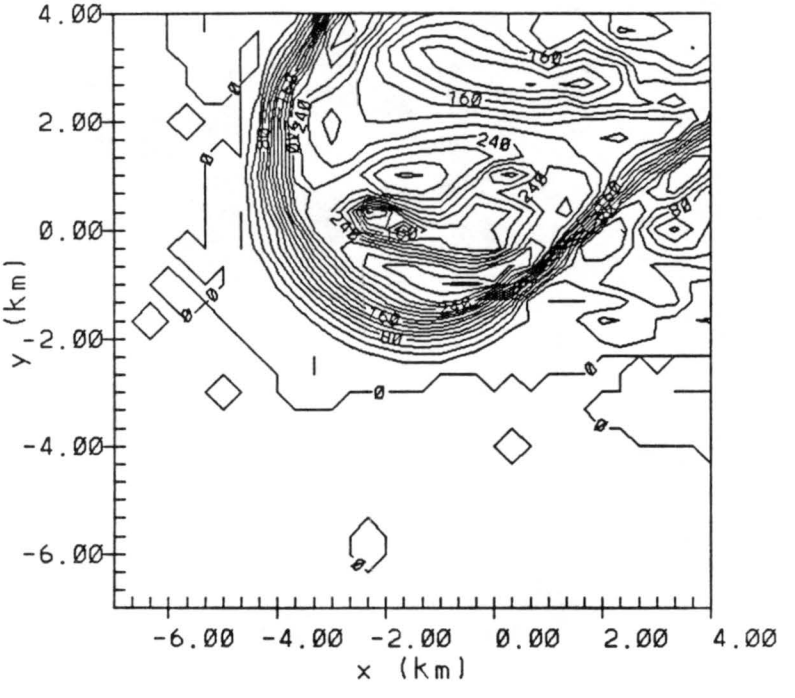

Figure 3.24: horizontal cross section of pristine ice mixing ratio at 6865m and 95min into the simulation. The contour interval is 0.2 g/kg. The maximum value is 3.2 g/kg.

mixing ratios are in an east-west band to the northwest of the main updraft as compared to more of a north-south band in Figure 3.16.

The graupel field, not shown, is similar to that 10 min earlier in that the field runs east to west to the north of the updraft. Instead of one central maximum at 95 min, there are two maxima in the field, one located directly to the north and one to the northeast of the updraft. The magnitudes are similar in both times.

At 3528 m and 105 min the vertical motion field has no resemblance to that ten min earlier in Figure 3.17. The strongest upward motion is located at x = -1.5 km and y = 0.0 km with a magnitude of 28 m/s. Another local maximum in the updraft field is located at x = -1.0 kilometers and y = -3.5 kilometers with a magnitude of 20 m/s. An intruding

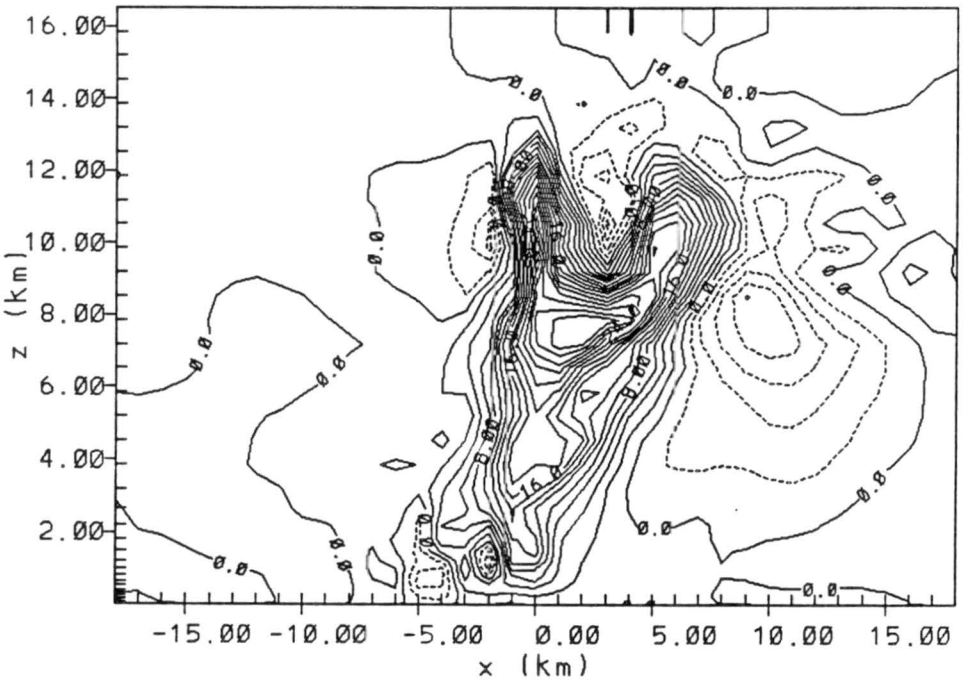

Figure 3.25: Vertical cross section of the vertical motion at y = -1.0 km and 105min into the simulation. Solid contours depict upward motion and dashed for downward. The contour interval is 2.0 m/s. The maximum upward is 34.0 m/s and the maximum downward is 10.0 m/s.

downdraft of magnitude 4.0 m/s located at x = -2.5 kilometers and y = -2.5 kilometers gives the updraft a backwards letter C shape. A more extensive region of downdraft is located to the north and northeast of the updraft with smaller intense regions of sinking motion. The strongest is -8.0 m/s. These features are seen in Figure 3.35.

Figure 3.36 shows the horizontal component of the wind field. The environmental winds are similar to those of Figure 18 where they flow from the southwest and turn cyclonically around the updraft to the northwest. The well-defined and conspicuous rotation seen in Figure 3.18 is not as clear in this figure and is smaller, being located at x = -2.5 km and y = 0.0 km.

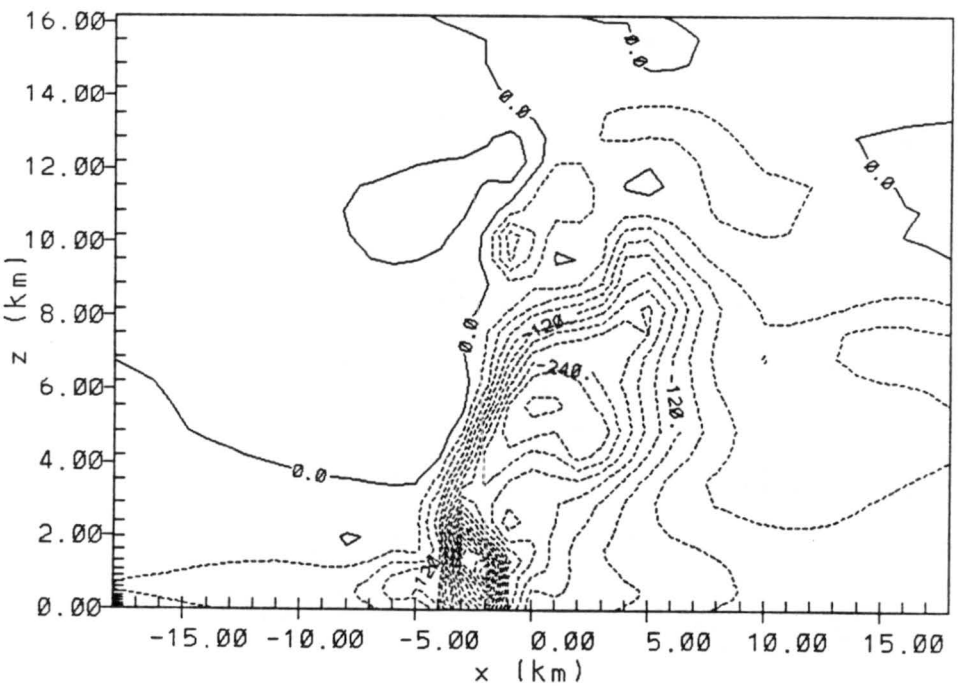

Figure 3.26: Vertical cross section of perturbation pressure at y = -1.0 km and 105min into the simulation. Dashed represents pressure deficits and solid for pressure excess. The contour interval is 30.0 pa. The maximum excess is 30.0 pa and the maximum deficit is -540.0 pa.

The rain mixing ratio field in Figure 3.37 is higher than those 10 min earlier by 2.0 g/kg. There are two areas of local maxima of rain mixing ratios, one located at x = -2.0 km and y = -1.0 km and the second at x = -1.75 km and y = 2.0 km. Although a local minimum is located at x = -2.0 km and y = 1.0 km, between the two local maxima, it's not clear if this region should be labeled a bounded weak echo region. Comparing this to the bounded weak echo region in Figure 3.19, one sees that the minimum in the rain mixing ratio in Figure 3.19 is near 0.4 g/kg, while that in Figure 3.37 is 3.0 g/kg. It's clear that as time evolves from 95 min to 105 min that the bounded weak echo region is

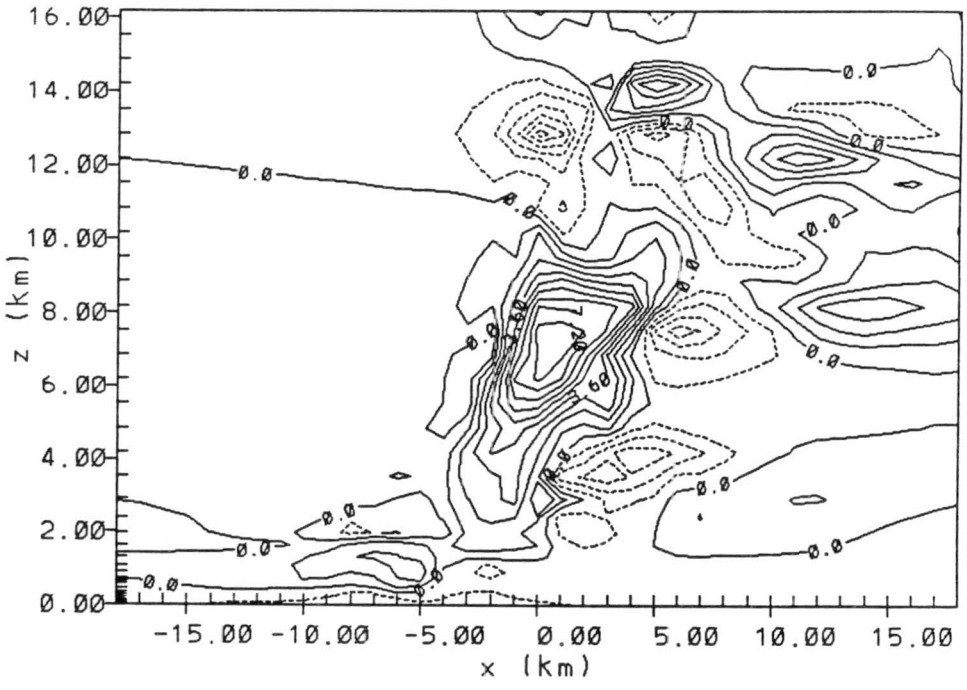

Figure 3.27: Vertical cross section of perturbation temperature at y = -1.0 km and 105min into the simulation. Solid contours show temperature excess and dashed for deficits. The contour interval is 0.9 C. The maximum excess is 8.1 C and -5.4 C for the deficit.

filling with echo. Observations have shown that bounded weak echo regions do fill when a tornado is forming.

The graupel field is not in a continuous band running east to west to the north of the updraft, rather it is in two distinct regions. One to the north and one to the northeast. The mixing ratios are also a little higher.

At 6865 m the updraft field is not at all similar to that 10 min earlier in Figure 3.20. Large horizontal gradients in the updraft speed are found in the southern side with a maximum updraft speed of 36 m/s located just to the north of the large updraft gradients. The updraft field ten minutes earlier, in Figure 3.20, show a local minimum in the upward speed in the center of the storm, which is not apparent in Figure 3.38.

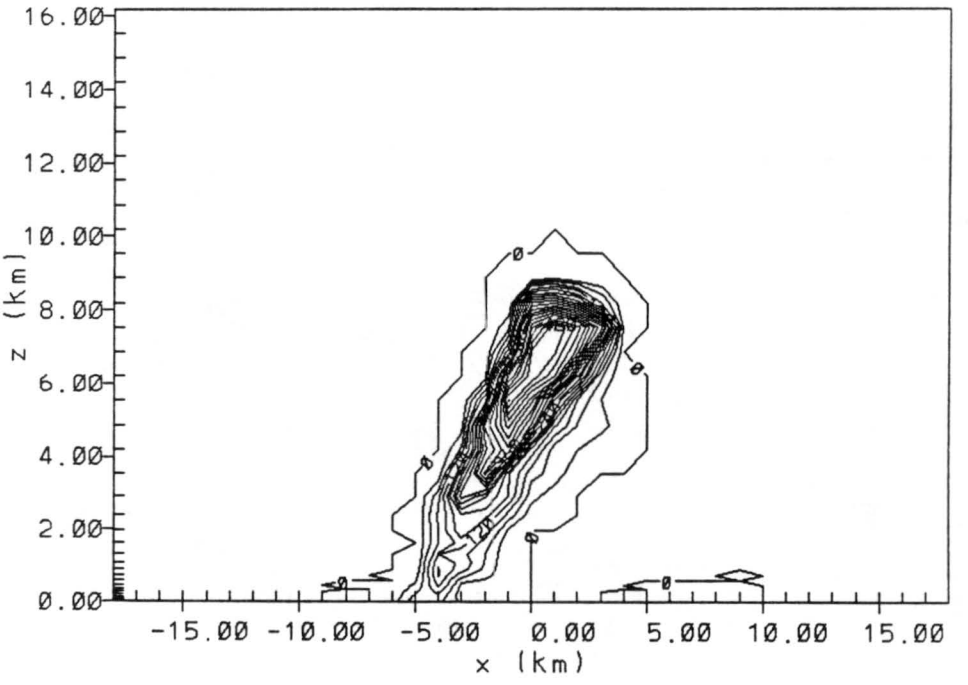

Figure 3.28: Vertical cross section of rain mixing ratio at y = - 1.0 km and 105min into the simulation. The contour interval is 0.3 g/kg. The maximum value is 6.0 g/kg.

Although not shown, the wind field resembles that in Figure 3.21 and the basic feature is obstacle like flow around the storm. The rain mixing ratios are smaller in areal coverage and like Figure 3.22 are coincident with the updraft. The mixing ratios are similar in magnitude for both times. The graupel field at 105 min is very disorganized with relative maxima located to the north, northeast and east of the updraft. The magnitude of graupel mixing ratios are similar to that found in Figure 3.23. The pristine ice field looks qualitatively like that in Figure 3.24 with the horizontal gradient of this field co-located with the large horizontal gradient in the updraft speed. The mixing ratio amounts are also alike.

The results of the simulation have features that are consistent with observations, the main ones are;

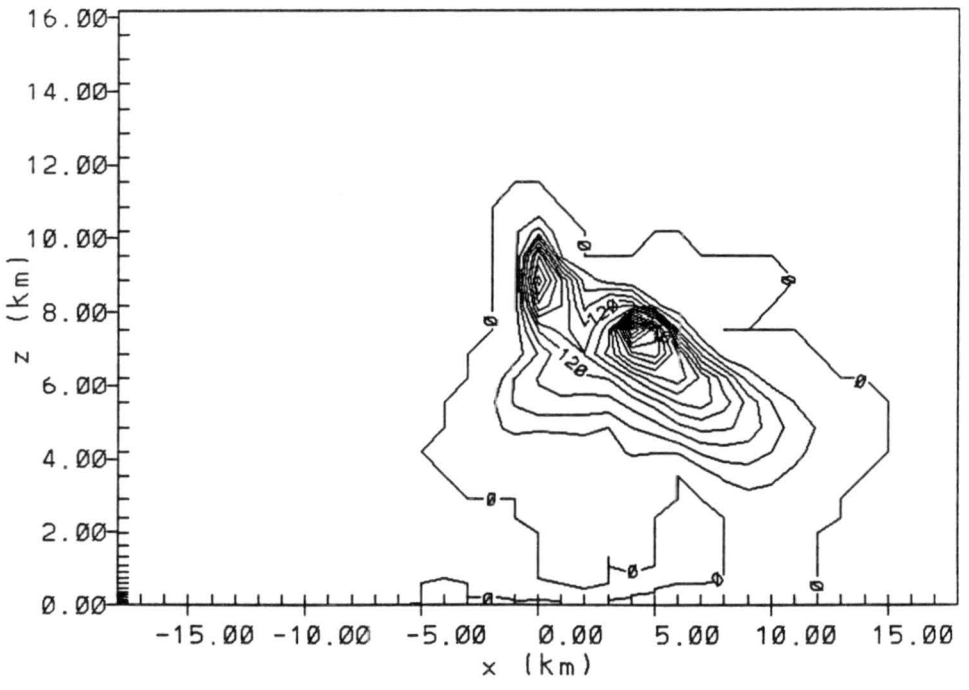

Figure 3.29: Same as Fig. 11 at 105min into the simulation. The maximum value is 4.8 g/kg.

1) The growing storm splits into a severe right mover and a weaker left mover.

2) The existence of strong updrafts (> 45 m/s) and downdrafts and their location relative to one and other.

3) The large values of rain mixing ratios near the freezing level may be suspect; in general, the overall field is consistent.

4) No hail species is included in this simulation; graupel, however, did reach the ground in regions where one would expect hail.

5) The air flow exhibited obstacle-like behavior at mid-levels.

6) The updraft has a significant downshear lean.

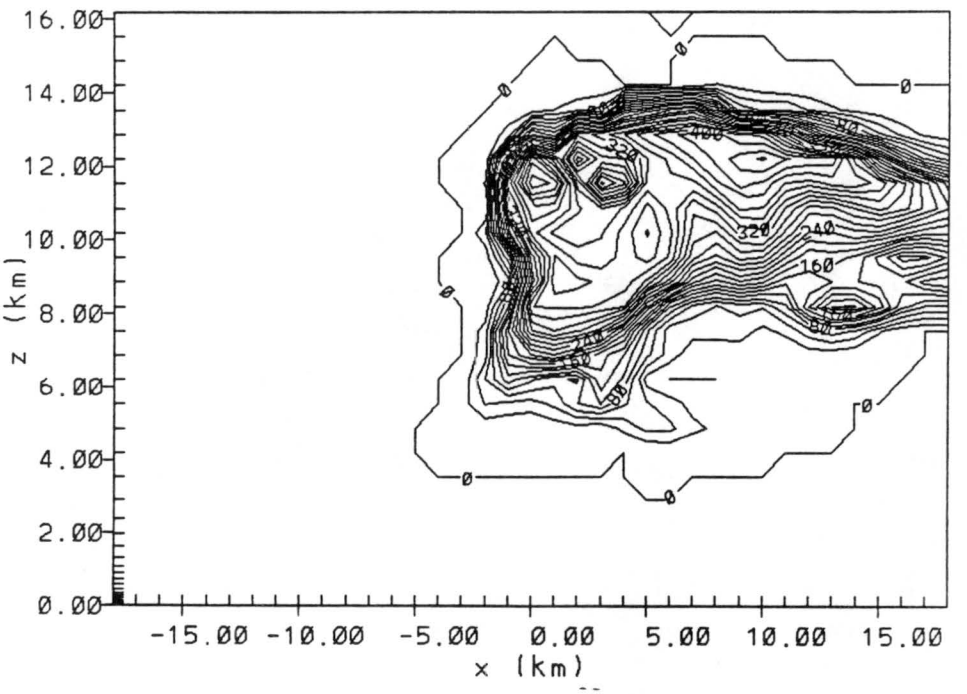

Figure 3.30: Same as Fig. 12 at 105min into the simulation. The contour interval is 0.2 g/kg. The maximum value is 4.6 g/kg.

7) The development of a bounded weak echo region (BWER) and a hook echo.

8) The descent of cloud top at the time of surface tornado formation.

In the next section mathematical equations will be developed and tornado-genesis will be explained.

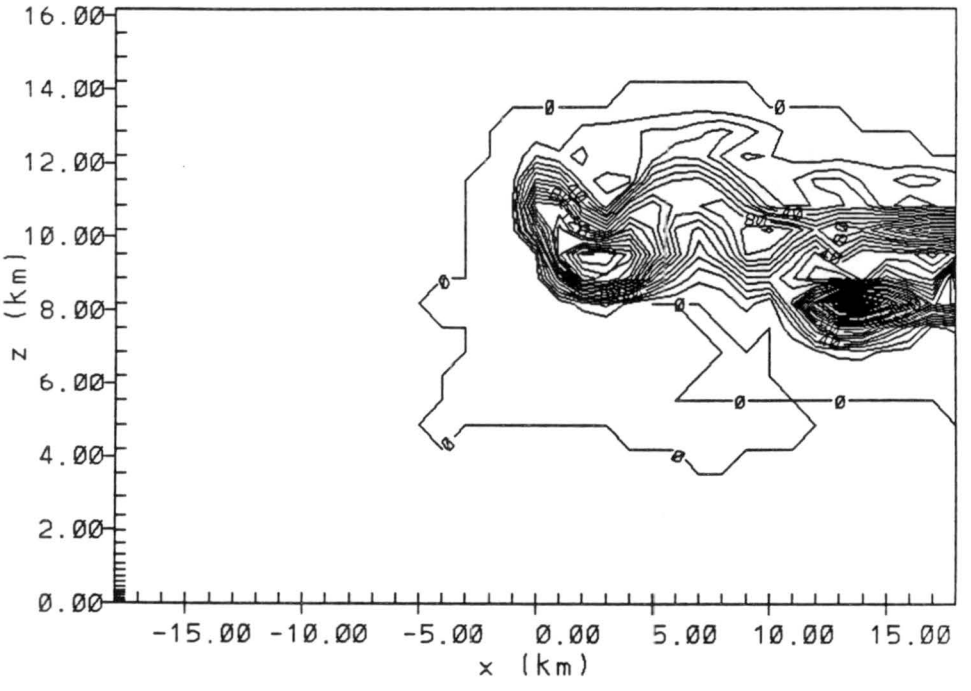

Figure 3.31: Same at Fig. 13 at 105 min into the simulation. The contour interval is 1.0 g/kg. The maximum value is 2.8 g/kg.

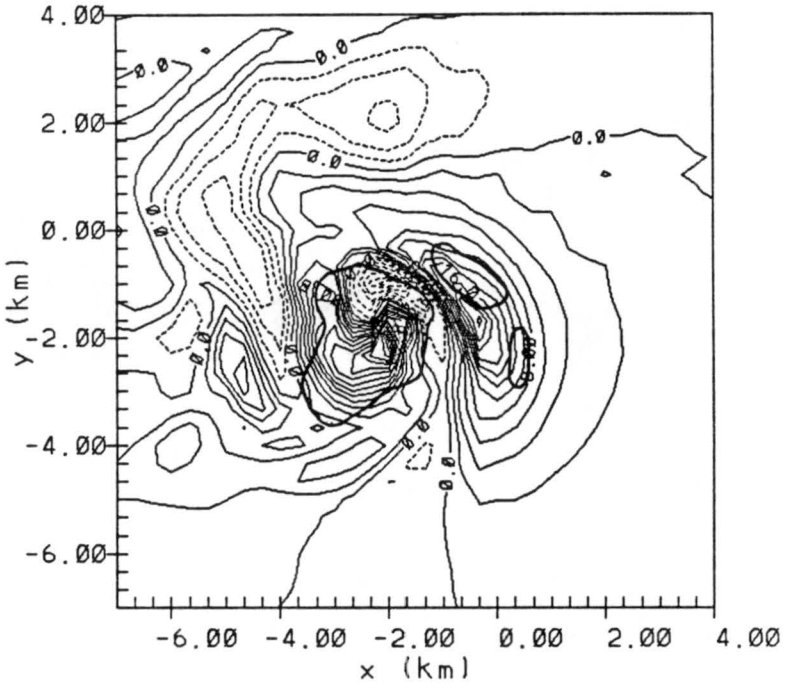

Figure 3.32: Same at Fig. 14 at 105min into the simulation. The maximum upward motion is 28.0 m/s and -12.0 m/s for downward motion.

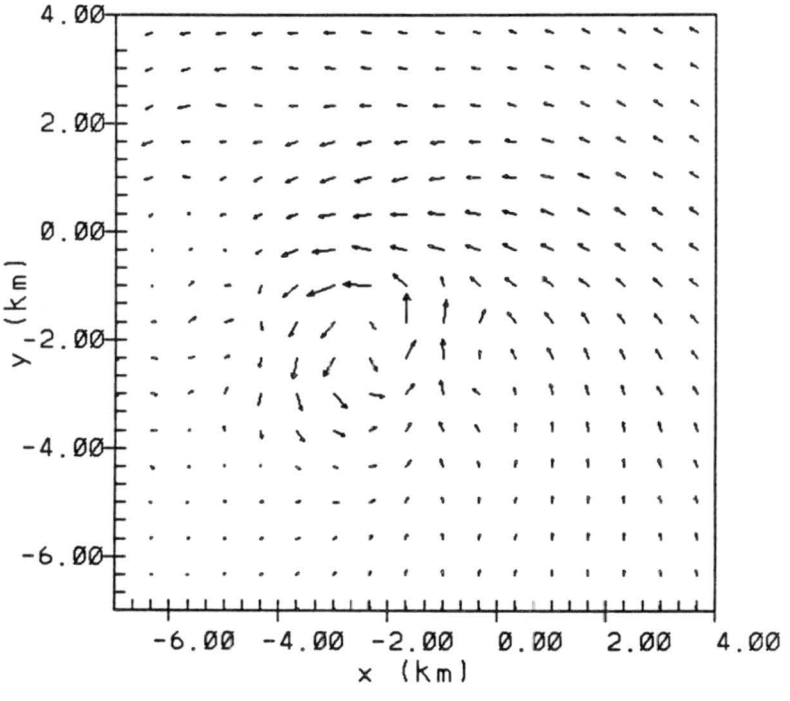

Figure 3.33: Same as Fig.15 at 105 min into the simulation. The maximum wind vector is 37.4 m/s.

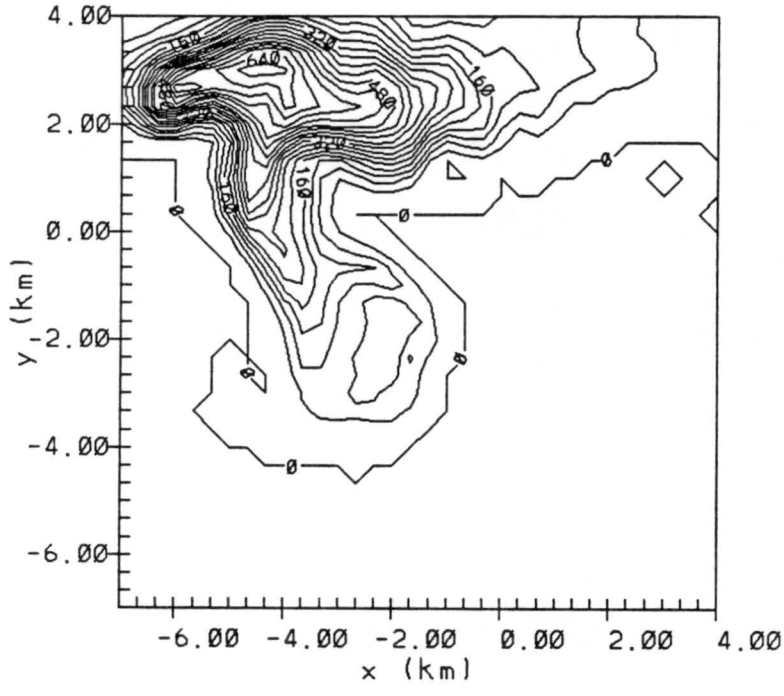

Figure 3.34: Same as Fig. 16 at 105 min into the simulation. The contour interval is 0.4 g/kg. The maximum value is 6.8 g/kg.

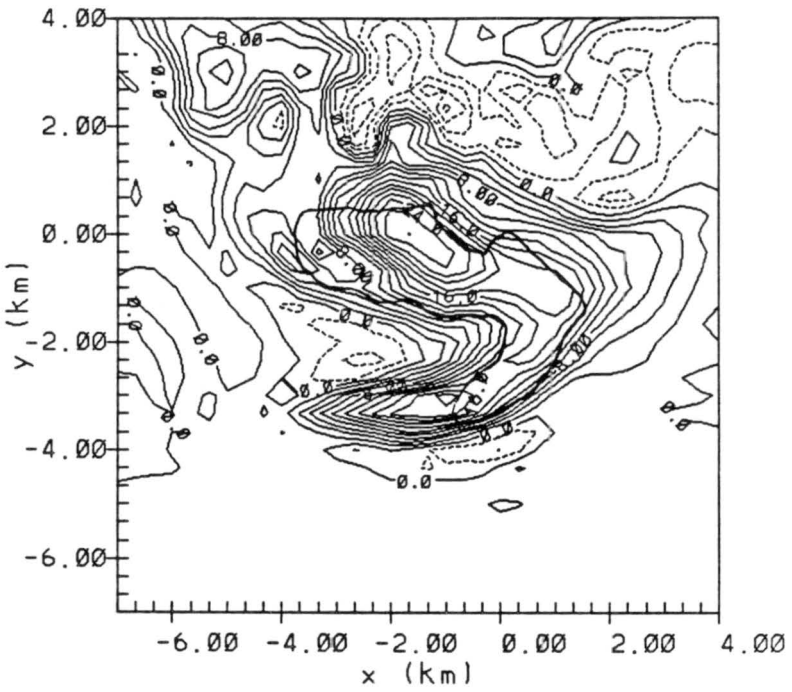

Figure 3.35: Same as Fig. 17 at 105min into the simulation. The maximum upward motion is 28.0 m/s.

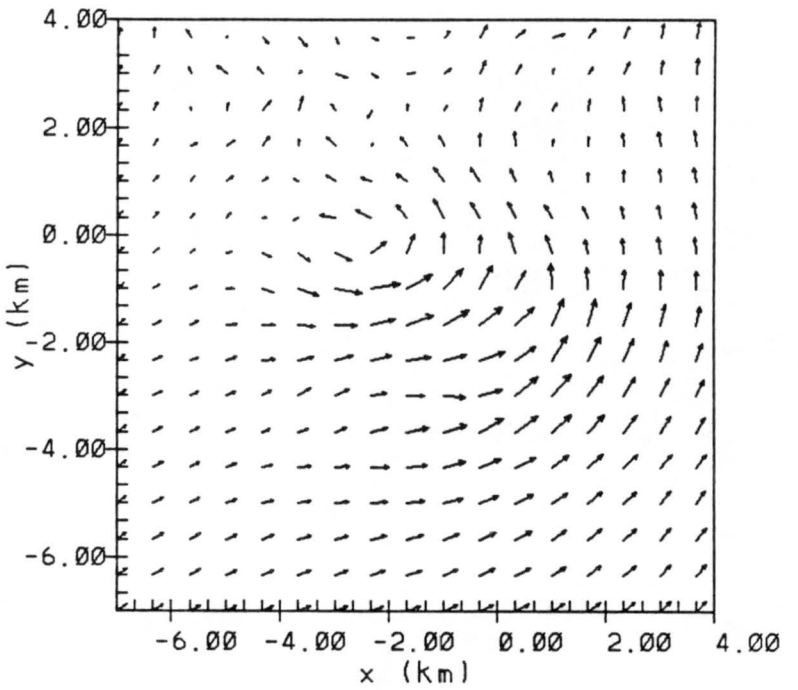

Figure 3.36: Same as Fig. 18 at 105 min into the simulation. The maximum wind vector is 29.1 m/s.

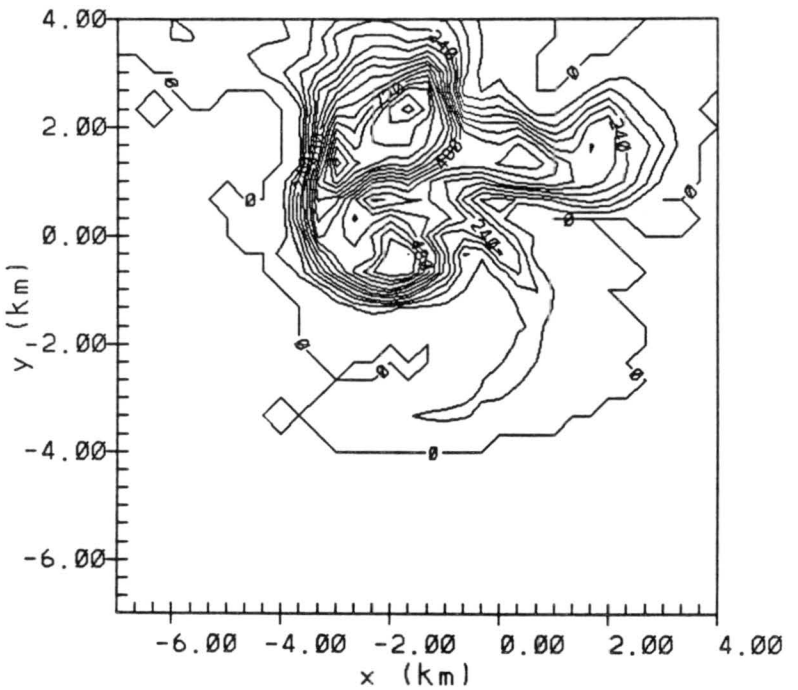

Figure 3.37: Same as Fig. 19 at 105min into the simulation. The contour interval is 0.6 g/kg. The maximum value is 9.6 g/kg.

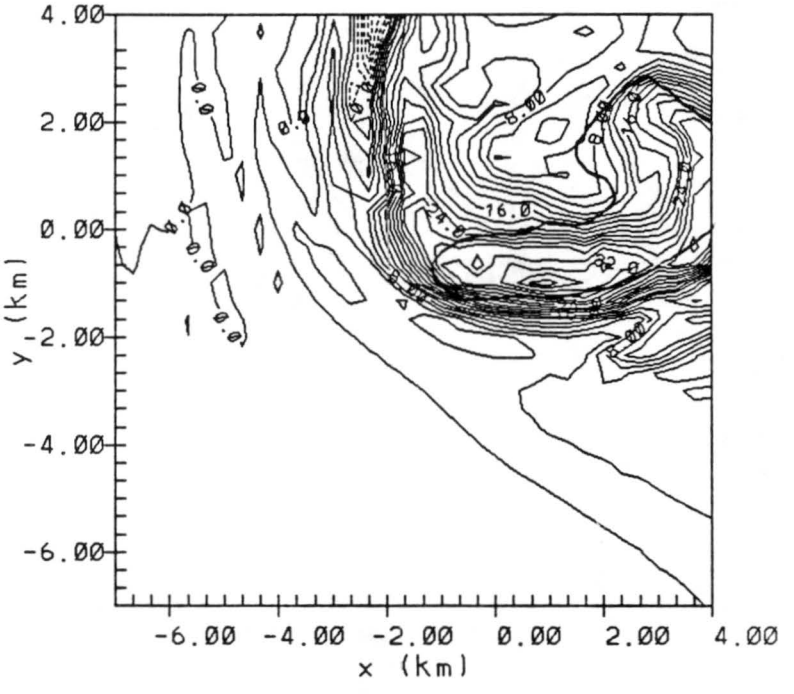

Figure 3.38: Same as Fig. 20 at 105min into the simulation. The maximum upward motion is 36.0 m/s.

Chapter 4

TORNADOGENESIS

4.1 Development of the Vorticity Equation

Before addressing the problem of tornadogenesis theoretically, some mathematical tools must be developed and discussed. The first is the vorticity equation. The equations will be cast using the components of cartesian tensors. The explicit usage of summation signs will be dropped with the understanding that two like indicies will be summed from 1 to 3, unless otherwise indicated. The index used is referred to as a dummy index and it doesn't matter what letter is used.

The momentum equation can be written,

$$\frac{\partial u_i}{\partial t} + u_j \frac{\partial u_i}{\partial x_j} = -\frac{1}{\rho_o(z)} \frac{\partial p^*}{\partial x_i} - \frac{\rho^*}{\rho_o(z)} g \delta_{i3}, \tag{4.1}$$

where Coriolis, friction and Reynolds stress terms have been neglected. The pressure and density have been decomposed into a horizontally homogeneous base state and deviations from that state; $p = p_o(z) + p^*$ $\rho = \rho_o(z) + \rho^*$. The horizontally homogeneous fields are assumed to be in hydrostatic balance, i.e., $\frac{\partial p_o(z)}{\partial z} = -\rho_o(z)g$. Before taking the curl of Eq.4.1, the advection term $u_j \frac{\partial u_i}{\partial x_j}$, will be simplified. Note that,

$$\frac{\partial u_i}{\partial x_j} = \frac{1}{2}\left[\frac{\partial u_i}{\partial x_j} + \frac{\partial u_j}{\partial x_i}\right] + \frac{1}{2}\left[\frac{\partial u_i}{\partial x_j} - \frac{\partial u_j}{\partial x_i}\right] = d_{ij} + r_{ji}, \tag{4.2}$$

where d_{ij} and r_{ji} are the components of the rate of strain and rotational tensor respectively. Vorticity is written,

$$\omega_k \equiv \epsilon_{kij} \frac{\partial u_j}{\partial x_i} = \frac{\epsilon_{kij}}{2} \frac{\partial u_j}{\partial x_i} + \frac{\epsilon_{kij}}{2} \frac{\partial u_j}{\partial x_i}, \tag{4.3}$$

in the last term let i=j and j=i to yield

$$\omega_k = \frac{\epsilon_{kij}}{2} \frac{\partial u_j}{\partial x_i} + \frac{\epsilon_{kji}}{2} \frac{\partial u_i}{\partial x_j}, \tag{4.4}$$

make use of $\epsilon_{kji} = -\epsilon_{kij}$

$$\omega_k = \frac{\epsilon_{kij}}{2}\frac{\partial u_j}{\partial x_i} - \frac{\epsilon_{kij}}{2}\frac{\partial u_i}{\partial x_j} = \epsilon_{kij}\frac{1}{2}\left[\frac{\partial u_j}{\partial x_i} - \frac{\partial u_i}{\partial x_j}\right] = \epsilon_{kij}r_{ij}, \tag{4.5}$$

multiply both sides by ϵ_{knm} yields

$$\omega_k\epsilon_{knm} = \epsilon_{knm}\epsilon_{kij}r_{ij} = \left[\delta_{ni}\delta_{mj} - \delta_{nj}\delta_{mi}\right]r_{ij} = r_{nm} - r_{mn} = 2r_{nm}, \tag{4.6}$$

since $-r_{mn} = r_{nm}$. Solving for r_{nm} yields

$$r_{nm} = \frac{1}{2}\omega_k\epsilon_{knm}. \tag{4.7}$$

Hence the advection term in Eq. 4.1 can be written as

$$\begin{aligned} u_j\frac{\partial u_i}{\partial x_j} &= u_j\frac{\partial u_i}{\partial x_j} - u_j\frac{\partial u_j}{\partial x_i} + u_j\frac{\partial u_j}{\partial x_i} \\ &= u_j\left[\frac{\partial u_i}{\partial x_j} - \frac{\partial u_j}{\partial x_i}\right] + u_j\frac{\partial u_j}{\partial x_i} = 2u_jr_{ji} + u_j\frac{\partial u_j}{\partial x_i}. \end{aligned} \tag{4.8}$$

Substituting Eq. 4.7 into the right hand side of Eq. 4.8 yields

$$u_j\frac{\partial u_i}{\partial x_j} = u_j\epsilon_{jin}\omega_n + u_j\frac{\partial u_j}{\partial x_i} = \epsilon_{inj}\omega_nu_j + u_j\frac{\partial u_j}{\partial x_i}. \tag{4.9}$$

Finally substituting this last expression into Eq. 4.1 yields

$$\frac{\partial u_i}{\partial t} + \epsilon_{inj}\omega_nu_j + \frac{\partial}{\partial x_i}\left[\frac{u_ju_j}{2}\right] = -\frac{1}{\bar{\rho}(z)}\frac{\partial p^*}{\partial x_i} - \frac{\rho^*}{\bar{\rho}(z)}g\delta_{i3}. \tag{4.10}$$

To obtain the vorticity equation, operate on both sides of Eq. 4.10 with $\epsilon_{ksi}\frac{\partial}{\partial x_s}$. The first term on the left hand side of Eq. 4.10 becomes

$$\epsilon_{ksi}\frac{\partial}{\partial x_s}\left[\frac{\partial u_i}{\partial t}\right] = \frac{\partial}{\partial t}\left[\epsilon_{ksi}\frac{\partial u_i}{\partial x_s}\right] = \frac{\partial\omega_k}{\partial t}. \tag{4.11}$$

The second term on the left hand side of Eq. 4.10 becomes

$$\begin{aligned} \epsilon_{ksi}\frac{\partial}{\partial x_s}\left[\epsilon_{inj}\omega_nu_j\right] &= \epsilon_{iks}\epsilon_{inj}\frac{\partial}{\partial x_s}\left[\omega_nu_j\right] \\ &= \left[\delta_{kn}\delta_{sj} - \delta_{kj}\delta sn\right]\frac{\partial}{\partial x_s}\left[\omega_nu_j\right] \\ &= \frac{\partial}{\partial x_j}\left[\omega_ku_j\right] - \frac{\partial}{\partial x_n}\left[\omega_nu_k\right] \\ &= u_j\frac{\partial\omega_k}{\partial x_j} + \omega_k\frac{\partial u_j}{\partial x_j} - u_k\frac{\partial\omega_n}{\partial x_n} - \omega_n\frac{\partial u_k}{\partial x_n}. \end{aligned} \tag{4.12}$$

The third term on the left hand side of Eq. 4.10 becomes

$$\epsilon_{ksi}\frac{\partial}{\partial x_s}\left[\frac{\partial}{\partial x_i}\left[\frac{u_j u_j}{2}\right]\right] = \epsilon_{ksi}\frac{\partial}{\partial x_s}\frac{\partial}{\partial x_i}\left[\frac{u_j u_j}{2}\right]. \tag{4.13}$$

The first term on the right hand side of Eq. 4.10 becomes

$$\epsilon_{ksi}\frac{\partial}{\partial x_s}\left[-\frac{1}{\bar{\rho}(z)}\frac{\partial p^*}{\partial x_i}\right] = -\epsilon_{ksi}\frac{\partial}{\partial x_s}\left[\frac{1}{\rho_o(z)}\right]\frac{\partial p^*}{\partial x_i} - \frac{1}{\rho_o(z)}\epsilon_{ksi}\frac{\partial}{\partial x_s}\left[\frac{\partial p^*}{\partial x_i}\right], \tag{4.14}$$

and the last term of Eq. 4.10 becomes

$$\epsilon_{ksi}\frac{\partial}{\partial x_s}\left[-\frac{\rho^*}{\rho_o(z)}g\delta_i 3\right]. \tag{4.15}$$

By combining all terms, we get the vorticity equation

$$\begin{aligned}\frac{\partial \omega_k}{\partial t} &+ u_j\frac{\partial \omega_k}{\partial x_j} + \omega_k\frac{\partial u_j}{\partial x_j} - u_k\frac{\partial \omega_n}{\partial x_n} - \omega_n\frac{\partial u_k}{\partial x_n} + \epsilon_{ksi}\frac{\partial}{\partial x_s}\frac{\partial}{\partial x_i}\left[\frac{u_j u_j}{2}\right] \\ &= -\epsilon_{ksi}\frac{\partial}{\partial x_s}\left[\frac{1}{\rho_o(z)}\right]\frac{\partial p^*}{\partial x_i} - \frac{\epsilon_{ksi}}{\rho_o(z)}\frac{\partial}{\partial x_s}\left[\frac{\partial p^*}{\partial x_i}\right] + \epsilon_{ksi}\frac{\partial}{\partial x_s}\left[-\frac{\rho^*}{\rho_o(z)}g\delta_{i3}\right].\end{aligned} \tag{4.16}$$

Let a_{ij} be symmetric and b_{ij} be antisymmetric, then

$$a_{ij}b_{ij} = \frac{a_{ij}b_{ij}}{2} + \frac{a_{ij}b_{ij}}{2}. \tag{4.17}$$

Let i=j and j=i in the last term to get

$$a_{ij}b_{ij} = \frac{a_{ij}b_{ij}}{2} + \frac{a_{ji}b_{ji}}{2} = \frac{a_{ij}b_{ij}}{2} - \frac{a_{ij}b_{ij}}{2} = 0. \tag{4.18}$$

Since $a_{ij} = a_{ji}$ and $b_{ji} = -b_{ij}$,the product of two terms, one symmetric and the other being antisymmetric in the same indices, is identically zero. For this reason the fourth and sixth terms on the left hand side of Eq. 4.16 along with the second term on the right hand side are identically zero. The vorticity equation then reduces to

$$\frac{\partial \omega_k}{\partial t} + u_j\frac{\partial \omega_k}{\partial x_j} = -\omega_k\frac{\partial u_j}{\partial x_j} + \omega_j\frac{\partial u_k}{\partial x_j} - \epsilon_{ksi}\frac{\partial}{\partial x_s}\left[\frac{1}{\rho_o(z)}\right]\frac{\partial p^*}{\partial x_i} + \epsilon_{ksi}\frac{\partial}{\partial x_s}\left[-\frac{\rho^*}{\rho_o(z)}g\delta_{i3}\right]. \tag{4.19}$$

Caution must be exercised when examining the first two terms on the right hand side of Eq. 4.19. Traditionally $-\omega_k\frac{\partial u_j}{\partial x_j}$ has been called the convergent term while $\omega_j\frac{\partial u_k}{\partial x_j}$ has been termed tilting and stretching. For $\omega_j\frac{\partial u_k}{\partial x_j}$ when k is not equal to j represents the re-orientation of vortex tubes. When k is equal to j, $\omega_j\frac{\partial u_k}{\partial x_j}$, represents vortex stretching.

Vortex stretching is commonly used to explain increases in vorticity in some atmospheric flows. However, when k = j, the first two terms on the right hand side of Eq. 4.19 identically cancel each other! In other words, vortex stretching is *not* represented in the vorticity equation. The first two terms on the right hand side of Eq. 4.19, therefore, represent convergence and re-orientation of vortex tubes.

The most general expression for divergence is $g^i \cdot \frac{\partial \mathcal{V}}{\partial u_i}$ where g^i is the contravariant basis vector and u^i is the coordinate of the system. Let's transform this expression to a new system denoted by placing a tilde over the variables. The transformation equations are;

$$g^i = \frac{\partial u^i}{\partial \tilde{u}^j}\tilde{g}^j, \qquad \mathcal{V} = v^k g_k = \frac{\partial u^k}{\partial \tilde{u}^n}\tilde{v}^n \frac{\partial \tilde{u}^r}{\partial u^k}\tilde{g}_r. \tag{4.20}$$

Substituting this into the expression for divergence yields

$$\begin{aligned} g^i \cdot \frac{\partial \mathcal{V}}{\partial u^i} &= \frac{\partial u^i}{\partial \tilde{u}^j}\tilde{g}^j \cdot \frac{\partial}{\partial u^i}\left[\frac{\partial u^k}{\partial \tilde{u}^n}\tilde{v}^n \frac{\partial \tilde{u}^r}{\partial u^k}\tilde{g}_r\right] = \frac{\partial u^i}{\partial \tilde{u}^j}\tilde{g}^j \cdot \frac{\partial}{\partial u^i}\left[\frac{\partial u^k}{\partial \tilde{u}^n}\frac{\partial \tilde{u}^r}{\partial u^k}\tilde{v}^n \tilde{g}_r\right] \\ &= \frac{\partial u^i}{\partial \tilde{u}^j}\tilde{g}^j \cdot \frac{\partial}{\partial u^i}\left[\delta^r_n \tilde{v}^n \tilde{g}_r\right] = \frac{\partial u^i}{\partial \tilde{u}^j}\tilde{g}^j \cdot \frac{\partial}{\partial u^i}\left[\tilde{v}^r \tilde{g}_r\right] \\ &= \frac{\partial u^i}{\partial \tilde{u}^j}\tilde{g}^j \cdot \frac{\partial}{\partial \tilde{u}^s}\left[\tilde{v}^r \tilde{g}_r\right]\frac{\partial \tilde{u}^s}{\partial u^i} = \frac{\partial u^i}{\partial \tilde{u}^j}\frac{\partial \tilde{u}^s}{\partial u^i}\tilde{g}^j \cdot \frac{\partial}{\partial \tilde{u}^s}\left[\tilde{v}^r \tilde{g}_r\right] = \delta^s_j \tilde{g}^j \cdot \frac{\partial}{\partial \tilde{u}^s}\left[\tilde{v}^r \tilde{g}_r\right] \\ &= \tilde{g}^j \cdot \frac{\partial}{\partial \tilde{u}^j}\left[\tilde{v}^r \tilde{g}_r\right] = \tilde{g}^j \cdot \frac{\partial \tilde{\mathcal{V}}}{\partial \tilde{u}^j}. \end{aligned} \tag{4.21}$$

Therefore the ***full*** divergence is invariant! However, by leaving one term out of the expression, say just look at the horizontal part, but still in three dimensional space, the resulting two-dimensional divergence is *not* invariant as will be shown for the simplified two dimensional field. Take the (x,y) rectangular coordinate system and rotate it about the origin through an angle α. The transformation equations for the coordinates and wind speeds are

$$\begin{aligned} x &= x'cos\alpha - y'sin\alpha & u' &= ucos\alpha + vsin\alpha \\ y &= x'sin\alpha + y'cos\alpha & v' &= -usin\alpha + vcos\alpha, \end{aligned} \tag{4.22}$$

where the prime denotes the coordinates in the rotated system. Note that x = x(x',y') and y=y(x',y'). Let's compute the divergence in the new system

$$\frac{\partial u'}{\partial x'} = \frac{\partial u}{\partial x'}cos\alpha + \frac{\partial v}{\partial x'}sin\alpha. \tag{4.23}$$

But u=u(x,y)=u(x(x',y'),y(x',y')), therefore, $\frac{\partial u}{\partial x'} = \frac{\partial u}{\partial x}\frac{\partial x}{\partial x'} + \frac{\partial u}{\partial y}\frac{\partial y}{\partial x'}$, from Eq. 4.22, $\frac{\partial x}{\partial x'} = cos\alpha$, $\frac{\partial y}{\partial x'} = sin\alpha$. Similarly $\frac{\partial v}{\partial x'} = \frac{\partial v}{\partial x}\frac{\partial x}{\partial x'} + \frac{\partial v}{\partial y}\frac{\partial y}{\partial x'} = \frac{\partial v}{\partial x}cos\alpha + \frac{\partial v}{\partial y}sin\alpha$. So

$$\frac{\partial u'}{\partial x'} = \frac{\partial u}{\partial x}cos^2\alpha + \frac{\partial u}{\partial y}sin\alpha cos\alpha + \frac{\partial v}{\partial x}sin\alpha cos\alpha + \frac{\partial v}{\partial y}sin^2\alpha. \tag{4.24}$$

Similarly

$$\frac{\partial v'}{\partial y'} = \frac{\partial u}{\partial x}sin^2\alpha - \frac{\partial u}{\partial y}sin\alpha cos\alpha - \frac{\partial v}{\partial x}sin\alpha cos\alpha + \frac{\partial v}{\partial y}cos^2\alpha \tag{4.25}$$

hence

$$\frac{\partial u'}{\partial x'} + \frac{\partial v'}{\partial y'} = \frac{\partial u}{\partial x} + \frac{\partial v}{\partial y}. \tag{4.26}$$

So, the full divergence is invariant for this two dimensional flow. However, as is shown by Eq. 4.24 or 4.25 $\frac{\partial u'}{\partial x'} \neq \frac{\partial u}{\partial x} and \frac{\partial v'}{\partial y'} \neq \frac{\partial v}{\partial y}$. The same is true for three dimensional flow, $\frac{\partial u'}{\partial x'} + \frac{\partial v'}{\partial y'} + \frac{\partial w'}{\partial x'} = \frac{\partial u}{\partial x} + \frac{\partial v}{\partial y} + \frac{\partial w}{\partial z}$ when all three axis are transformed to three new and different axes. But $\frac{\partial u'}{\partial x'} + \frac{\partial v'}{\partial y'} \neq \frac{\partial u}{\partial x} + \frac{\partial v}{\partial y}$! This brings us back immediately to Eq. 4.19. The first term on the right hand side, $\omega_k \frac{\partial u_j}{\partial x_j}$, has a part that cancels with a part with the second term on the right hand side, $\omega_j \frac{\partial u_k}{\partial x_j}$. The parts that are left in these two terms are not invariant under a transformation of coordinates. The implication of this is, looking at these two terms independently, can be misleading (Davis Jones, 1982). For example, one could analyse a wind field and determine that the convergent term is an order of magnitude larger than the tilting term and conclude that tilting is not important in this case. A transformation of coordinates could yield the two terms to be of similar magnitude. The question now is *Is there a correct coordinate system to use?* The answer is no. A coordinate system formed from the eigenvectors, the principle axes, of the strain rate seems to be a likely choice. However, that system is unique. A new system transformed to from the principle system will not be a principle system itself. Because of this, one will still be plagued with the non-invariance of the titling and convergent terms. Although the principle system is orthogonal,it is also a function of time, and the basis vectors would have to be recomputed at each time step in a model. Another likely coordinate system can be defined by the vortex lines. This system is also plagued by the variance of the convergent and tilting terms once a transformation from it has been

carried out. This system is also a function of time as the vortex lines are not necessarily frozen in space.

By looking at just one component of the vorticity equation, say the vertical, one can "miss" processes that lead to vortex tube strength increases in the following way. If the vortex tube is not vertical, than it's easily seen that the vortex tube strength may increase due to the other two horizontal components. One may conclude, erroneously, that say, a thunderstorm is not rotating faster since the vertical component of vorticity is not changing. The thunderstorm may actually be rotating faster simply because it's leaning away from the vertical, as most strong thunderstorms do. The full three dimensionality of the vorticity equation must be considered along with the variance and coupling of the convergent and tilting terms.

4.2 Development of a Pressure Diagnostic Equation

The next tool that is needed is a diagnostic equation for pressure. Multiply Eq. 1 by $\rho_o(z)$ to obtain

$$\rho_o(z)\frac{\partial u_i}{\partial t} + \rho_o(z)u_j\frac{\partial u_i}{\partial x_j} = -\frac{\partial p^*}{\partial x_i} - \rho_o(z)B\delta_{i3} \qquad where B \equiv \frac{\rho^*}{\rho_o(z)}g. \tag{4.27}$$

Add u_i times the anelastic continuity equation, $\frac{\partial}{\partial x_j}[\rho_o(z)u_j] = 0$, to the left hand side of Eq. 27 to obtain

$$\rho_o(z)\frac{\partial u_i}{\partial t} + \frac{\partial}{\partial x_j}[\rho_o(z)u_ju_i] = -\frac{\partial p^*}{\partial x_i} - \rho_o(z)B\delta_{i3}. \tag{4.28}$$

Take the divergence, $\frac{\partial}{\partial x_i}$, of Eq. 28

$$\frac{\partial}{\partial x_i}\left[\frac{\partial}{\partial t}[\rho_o(z)u_i]\right] + \frac{\partial}{\partial x_i}\left[\frac{\partial}{\partial x_j}[\rho_o(z)u_ju_i]\right] = -\frac{\partial}{\partial x_i}\frac{\partial p^*}{\partial x_i} - \frac{\partial}{\partial x_i}[\rho_o(z)B\delta_{i3}]. \tag{4.29}$$

The first term on the left hand side of Eq. 29 is zero since $\frac{\partial}{\partial x_i}\frac{\partial}{\partial t}[\rho_o(z)u_i] = \frac{\partial}{\partial t}\frac{\partial}{\partial x_i}[\rho_o(z)u_i] = 0$ if the fluid is assumed anelastic (i.e., $\frac{\partial}{\partial x_i}[\rho_o(z)u_i] = 0$). Solving for the Laplacian of p^* yields

$$\frac{\partial}{\partial x_i}\frac{\partial p^*}{\partial x_i} = -\frac{\partial}{\partial x_i}\left[\frac{\partial}{\partial x_j}[\rho_o(z)u_ju_i]\right] - \frac{\partial}{\partial x_i}[\rho_o(z)B\delta_{i3}]. \tag{4.30}$$

The first term on the right hand side can be written in a more useful way as follows. Making use of the anelastic continuity equation

$$-\frac{\partial}{\partial x_i}\left[\frac{\partial}{\partial x_j}\left[\rho_o(z)u_j u_i\right]\right] = -\frac{\partial}{\partial x_i}\left[\rho_o(z)u_j\frac{\partial u_i}{\partial x_j}\right]$$
$$= -\rho_o(z)\frac{\partial u_i}{\partial x_j}\frac{\partial u_j}{\partial x_i} - u_j\frac{\partial}{\partial x_i}\left[\rho_o(z)\frac{\partial u_i}{\partial x_j}\right]. \qquad (4.31)$$

Using Eq. 2 for the last two factors in the first term on the right hand side of Eq. 31 yields

$$-\rho_o(z)\left[d_{ij}+r_{ji}\right]\left[d_{ij}+r_{ij}\right] - u_j\frac{\partial}{\partial x_i}\left[\rho_o(z)\frac{\partial u_i}{\partial x_j}\right]. \qquad (4.32)$$

After multiplying out the first term in Eq. 32 and using the fact that the product of d_{ij}, symmetric in i and j and r_{ji}, antisymmetric in i and j, is identically zero yields

$$-\rho_o(z)d_{ij}d_{ij} - \rho_o(z)r_{ji}r_{ij} - u_j\frac{\partial}{\partial x_i}\left[\rho_o(z)\frac{\partial u_i}{\partial x_j}\right]. \qquad (4.33)$$

Using Eq. 7 in the second term yields

$$-\rho_o(z)d_{ij}d_{ij} - \rho_o(z)\left[\epsilon_{jin}\frac{\omega_n}{2}\right]\left[\epsilon_{ijk}\frac{\omega_k}{2}\right] - u_j\frac{\partial}{\partial x_i}\left[\rho_o(z)\frac{\partial u_i}{\partial x_j}\right]. \qquad (4.34)$$

Make use of the fact that $\epsilon_{jin}\epsilon_{ijk} = \epsilon_{inj}\epsilon_{ijk} = \delta_{nj}\delta_{jk} - \delta_{nk}\delta_{jj}$,gives

$$-\rho_o(z)d_{ij}d_{ij} - \frac{\bar{\rho}(z)}{4}\left[\omega_j\omega_j - \delta_{jj}\omega_k\omega_k\right] - u_j\frac{\partial}{\partial x_i}\left[\rho_o(z)\frac{\partial u_i}{\partial x_j}\right]. \qquad (4.35)$$

Now $\delta_{jj} = \delta_{11} + \delta_{22} + \delta_{33} = 3$, then replace the k index of $\omega_k\omega_k$ with j yields

$$-\rho_o(z)d_{ij}d_{ij} - \frac{\bar{\rho}(z)}{2}\omega_j\omega_j - u_j\frac{\partial}{\partial x_i}\left[\rho_o(z)\frac{\partial u_i}{\partial x_j}\right]. \qquad (4.36)$$

Replace the first term on the right hand side of Eq. 30 with Eq. 36 to yield

$$\frac{\partial}{\partial x_i}\frac{\partial p^*}{\partial x_i} = -\rho_o(z)d_{ij}d_{ij} - \frac{\rho_o(z)}{2}\omega_j\omega_j - u_j\frac{\partial}{\partial x_i}\left[\rho_o(z)\frac{\partial u_i}{\partial x_j}\right] - \frac{\partial}{\partial x_i}\left[\rho_o(z)B\delta_{i3}\right]. \qquad (4.37)$$

The third term on the right hand side can also be simplified,

$$-u_j\frac{\partial}{\partial x_i}\left[\rho_o(z)\frac{\partial u_i}{\partial x_j}\right] = -u_j\frac{\partial u_i}{\partial x_j}\frac{\partial \rho_o(z)}{\partial x_i} - \rho_o(z)u_j\frac{\partial}{\partial x_i}\frac{\partial u_i}{\partial x_j}$$
$$= -u_j\frac{\partial u_i}{\partial x_j}\frac{\partial \rho_o(z)}{\partial x_i} - \rho_o(z)u_j\frac{\partial}{\partial x_j}\left[\frac{\partial u_i}{\partial x_i}\right]. \qquad (4.38)$$

¿From the anelastic continuity equation, $\frac{\partial}{\partial x_i}[\rho_o(z)u_i] = 0$ implies $\frac{\partial u_i}{\partial x_i} = -\frac{u_i}{\rho_o(z)}\frac{\partial \rho_o(z)}{\partial x_i} = -\frac{w}{\rho_o(z)}\frac{\partial \rho_o(z)}{\partial z}$ since $\frac{\partial \rho_o(z)}{\partial x} = \frac{\partial \rho_o(z)}{\partial y} = 0$. Substituting this into the last term of Eq. 38 yields

$$\begin{aligned} -u_j\frac{\partial}{\partial x_i}\left[\rho_o(z)\frac{\partial u_i}{\partial x_j}\right] &= -u_j\frac{\partial u_i}{\partial x_j}\frac{\partial \rho_o(z)}{\partial x_i} + \rho_o(z)u_j\frac{\partial}{\partial x_j}\left[\frac{W}{\rho_o(z)}\frac{\partial \rho_o(z)}{\partial z}\right] \\ &= -u_j\frac{\partial W}{\partial x_j}\frac{\partial \bar{\rho}(z)}{\partial z} + \rho_o(z)u_j\frac{\partial}{\partial x_j}\left[\frac{W}{\rho_o(z)}\frac{\partial \rho_o(z)}{\partial z}\right]. \end{aligned} \quad (4.39)$$

For j = 1,2 only

$$-u_j\frac{\partial W}{\partial x_j}\frac{\partial \rho_o(z)}{\partial z} + \rho_o(z)u_j\frac{\partial}{\partial x_j}\left[\frac{W}{\rho_o(z)}\frac{\partial \rho_o(z)}{\partial z}\right] = -u_j\frac{\partial W}{\partial x_j}\frac{\partial \rho_o(z)}{\partial z} + u_j\frac{\partial W}{\partial x_j}\frac{\partial \rho_o(z)}{\partial z} = 0. \quad (4.40)$$

For j = 3

$$\begin{aligned} -u_j\frac{\partial W}{\partial x_j}\frac{\partial \rho_o(z)}{\partial z} &+ \rho_o(z)u_j\frac{\partial}{\partial x_j}\left[\frac{W}{\rho_o(z)}\frac{\partial \rho_o(z)}{\partial z}\right] \\ &= -W\frac{\partial W}{\partial z}\frac{\partial \rho_o(z)}{\partial z} + \rho_o(z)W\frac{\partial}{\partial z}\left[\frac{W}{\rho_o(z)}\frac{\partial \rho_o(z)}{\partial z}\right] \\ &= -W\frac{\partial W}{\partial z}\frac{\partial \bar{\rho}(z)}{\partial z} + W\frac{\partial W}{\partial z}\frac{\partial \rho_o(z)}{\partial z} + \rho_o(z)W^2\frac{\partial}{\partial z}\left[\frac{1}{\rho_o(z)}\frac{\partial \rho_o(z)}{\partial z}\right] \\ &= \rho_o(z)W^2\frac{\partial^2}{\partial z^2}[ln\rho_o(z)]. \end{aligned} \quad (4.41)$$

Substituting this last equation back into the third term on the right hand side of Eq. 37 to get the final form of the diagnostic equation for pressure:

$$\frac{\partial}{\partial x_i}\frac{\partial p^*}{\partial x_i} = -\rho_o(z)d_{ij}d_{ij} + \frac{\rho_o(z)}{2}\omega_j\omega_j + \rho_o(z)W^2\frac{\partial^2}{\partial z^2}[ln\rho_o(z)] - \frac{\partial}{\partial z}[\rho_o(z)B]. \quad (4.42)$$

The first term on the right hand side represents the square of the rate of strain. This term always is correlated with the perturbation pressure being higher, on average, relative to points near it. It is important to point out that convergent and divergent fields are included in this term and both are correlated with a perturbation high. The second term is the square of the magnitude of total relative vorticity, also known as enstrophy. This term is always positive and hence a vorticity field, cyclonic or anticyclonic contributes to low pressure. Note that one way to amplify existing vorticity is to converge vortex lines. While convergence will act to increase the pressure, the resulting vorticity field will at

times balance this effect and may in fact be so large as to leave the pressure a relative low. The first two terms on the right hand side are large compared to the last two terms (Brandes, 1984) and therefore dominate the pressure field near and within a supercell thunderstorm. Therefore, to a good approximation,

$$\frac{\partial}{\partial x_i}\frac{\partial p^*}{\partial x_i} \simeq -\rho_o(z) d_{ij} d_{ij} + \frac{\rho_o(z)}{2}\omega_j \omega_j. \tag{4.43}$$

4.3 Analysis of High Resolution Model Output

At ninety minutes into the simulation, two finer grids were spawned. The model was allowed to run forward and at ninety six minutes analysis was done and is shown in Figure 4.1. The height is 1095m which is approximately cloud base. This and the following figures are for the finest grid where the horizontal grid spacing is 111m, unless stated otherwise. The solid lines depict the updraft speed, although the maximum of 36 m/s is seen at x = -1.75 km and y = -1.6. Note in particular the large horizontal gradient of the updraft speed just to the east of the updraft maximum. The pressure deficit, the long dashed lines, is a minimum in the same location with a value of -850 pa. The positive vertical vorticity, represented by a dashed-dot, with a maximum of 0.14 s^{-1} is highly correlated with the pressure minimum. The outermost contour of positive vertical vorticity has a value of $0.05 s^{-1}$ and is interpreted as the boundary of the mesocyclone. The horizontal vorticity vectors, shown by arrows, maximizes at the location of the largest horizontal gradient of updraft speed. Roughly two kilometers to the south-southwest of the main updraft is a region of low pressure and negative vertical vorticity. A striking feature is that the minimum in the pressure field is correlated with the maximum in the vorticity field, both the vertical component and the horizontal vectors.

A question that arises immediately from this figure is, should one expect the location of the local maximums or minimums of the pressure field and the total three dimensional vorticity field to be highly correlated? The diagnostic equation for pressure helps answer this question. Recall that the two terms that dominate are the square of the rate of strain and the square of the three dimensional vorticity. The rate of strain term is always correlated with high perturbation pressure and the vorticity term is always correlated

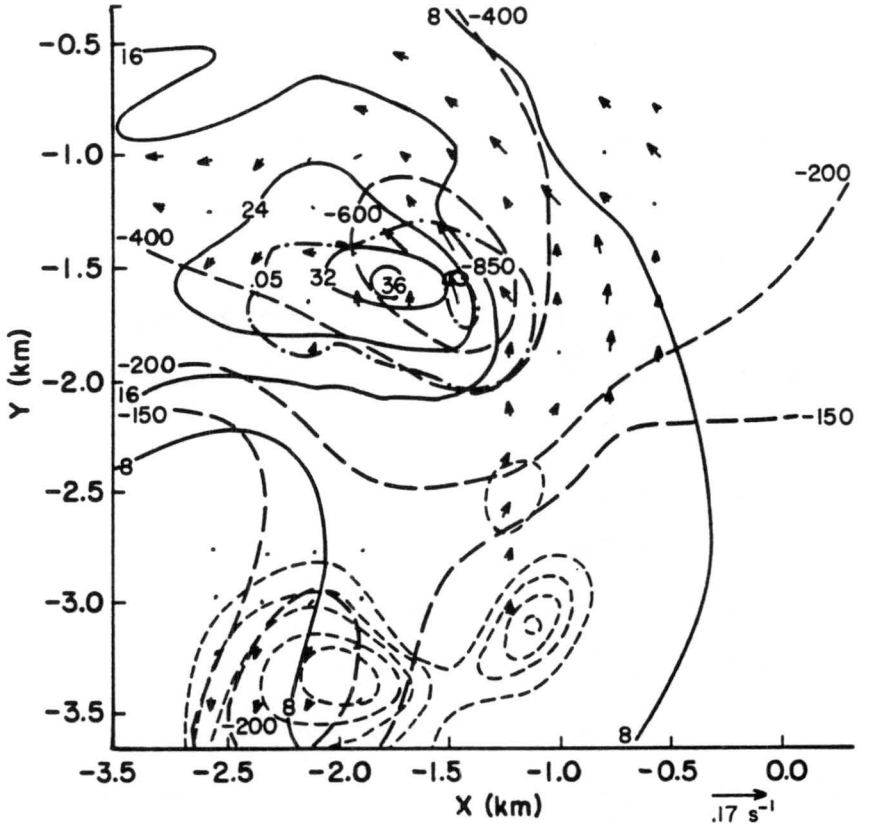

Figure 4.1: Horizontal cross section through the thunderstorm at 1095m and 96min into the simulation. Solid contours depicts upward motion in m/s, long dashed shows the perturbation pressure deficit, in pa. Positive vertical vorticity is depicted by dashed-dot and negative vertical vorticity by short dashed, in s^{-1} and horizontal vorticity vectors by arrows, the maximum vector is shown in the lower right of the figure.

with low perturbation pressure. In Figure 4.1, since the perturbation pressure is a low one can conclude that the vorticity term is responsible, and therefore, the region of low pressure is also the region of the maximum magnitude of the three dimensional vorticity field. The sign of the vertical vorticity is irrelevant, only the magnitude, and that's why one sees a local minimum in the pressure field where the vertical vorticity is positive, at x = -1.4 and y = -1.75, and where the vertical vorticity is negative, at x = -2.0 and y = -3.4 .

Even though the overall features at 1633m are basically the same, Figure 4.2, there are important differences. The maximum updraft speed of 34 m/s is slightly weaker and the horizontal gradient of the updraft speed is not nearly as large. The maximum pressure deficit is -760 pa and is not co-located with the maximum vertical vorticity but rather the largest horizontal vorticity vectors. The location of the positive vertical vorticity maximum is slightly to the east of the updraft maximum. A large region of positive vertical vorticity surrounds the core of the updraft as well as the largest pressure deficit with a value of 0.02 s^{-1} and is to be interpreted as the boundary of the mesocyclone.

A pressure trough is found to the south of the main updraft and is co-located with the largest, locally, horizontal vorticity vectors and negative vertical vorticity. Just to the east of this region is a secondary updraft with a local maximum of 22 m/s.

At 463m, Figure 4.3, the updraft has a maximum of 23 m/s with the region of largest horizontal gradient in updraft speed located around 500m to the southeast. The two small closed circles have pressure deficits of -360 and -380 pa respectively. There is a smaller circle immediately to the south and this represents the vertical vorticity maximum of 0.15 s^{-1}. The mesocyclone is delineated by the dashed-dot contour that again represents the vertical vorticity and has magnitude of 0.05 s^{-1}.

Figure 4.4 shows the model fields at 1095m and 99min. The shape of the updraft has changed, in particular a marked local minimum in the updraft field of 2 m/s at x = -1.25 and y = -1.25 is evident. This feature is maintaining the large horizontal gradient of the updraft speed between it and the local maximum in the updraft of 34 m/s just to

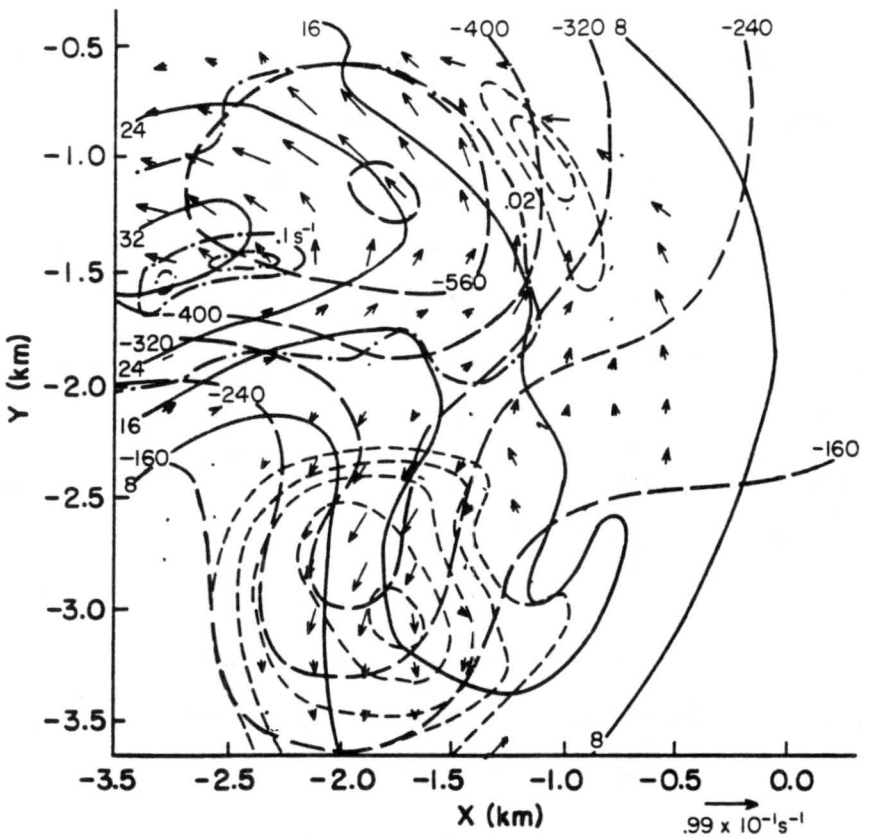

Figure 4.2: Same as Fig. 4.1 at 1633m and 96min.

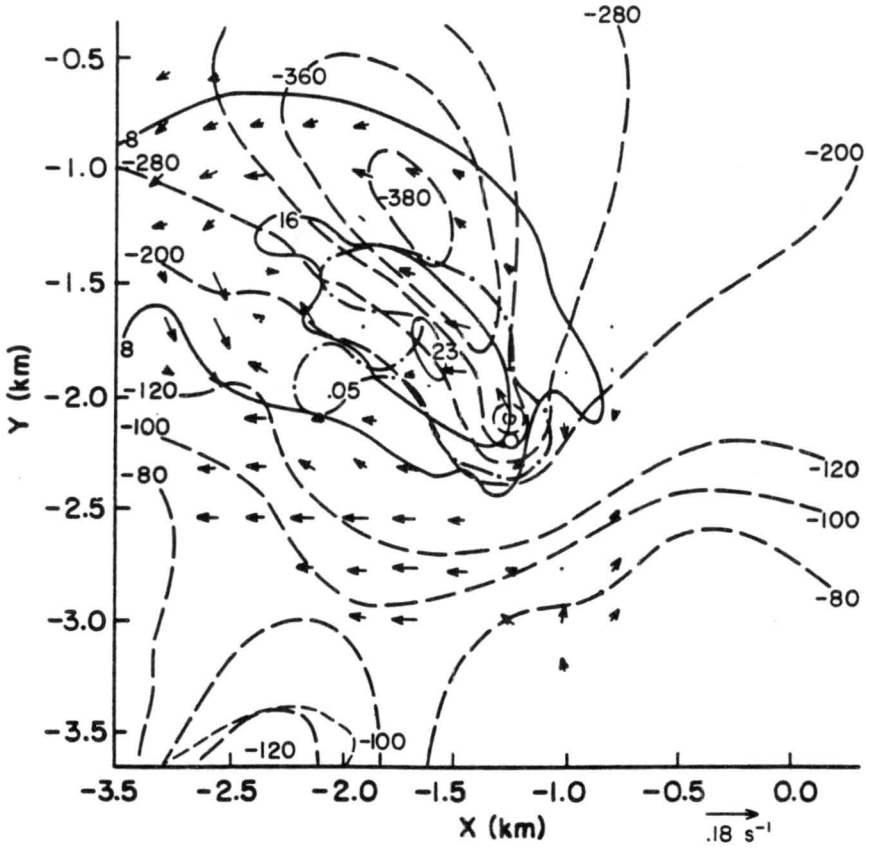

Figure 4.3: Same as Fig. 4.1 at 463m and 96min.

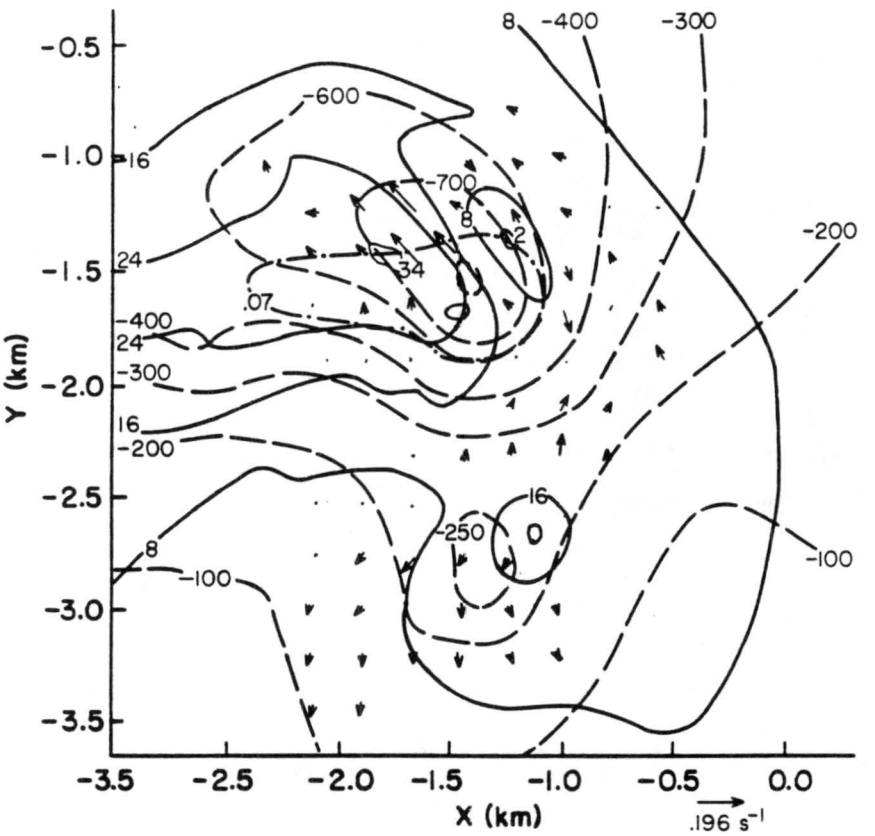

Figure 4.4: Same as Fig. 4.1 at 1095m and 99min.

the west. To the south at x = -1.0 and y = -2.75 a local maximum in the updraft field of 20 m/s has formed in just a few short minutes (see Figure 4.1 at the same location.).

The extrema in the pressure field are still correlated well with the extrema in the total three dimensional vorticity field. A local minimum of -900 pa is located at x = -1.4 and y = -1.6 about one hundred meters to the north of the positive vertical vorticity maximum and in the same region where the largest horizontal vorticity vectors are. To the south a secondary pressure minimum of -250 pa is just to the west of the 20 m/s updraft and again highly correlated with the maximum in the total vorticity field.

Figure 4.5 shows that the secondary updraft located to the southeast of the main updraft is intensifying at 1633m. The extrema in the pressure field is seen to co-locate with the extrema of the total vorticity.

At 581m, Figure 4.6 shows that the location of the relative minimum of the pressure field relative to the local maximum in the total vorticity is well preserved.

Figure 4.7 shows the surface fields. One striking feature is that the location of the pressure minimum, positive vertical vorticity maximum and the maximum in updraft field are all highly correlated.

Since 96 minutes the pressures have fallen at all of the levels shown. A well-defined pressure " tube " with a deficit of -900 pa exist from 1340m to 722m. The strength of the main updraft is essentially unchanged.

By examining the wind field each minute up to 99 minutes shows a well-defined rotation to the surface at the levels shown in the above figures. However, it's not clear if a distinct well-organized and stable tornadic vortex has been resolved. A three dimensional Lagrangian particle dispersion model has been run to investigate the existence of the tornado. The results show a well-defined stable rotating vortex from the ground to cloud base and therefore this feature is identified as the tornado.

As the model is run forward the main updraft and the secondary updraft, initially located to the south southeast, rotate counter-clockwise around each other and a significant downdraft forms between them and they also start to fill in a portion of the mesocyclone.

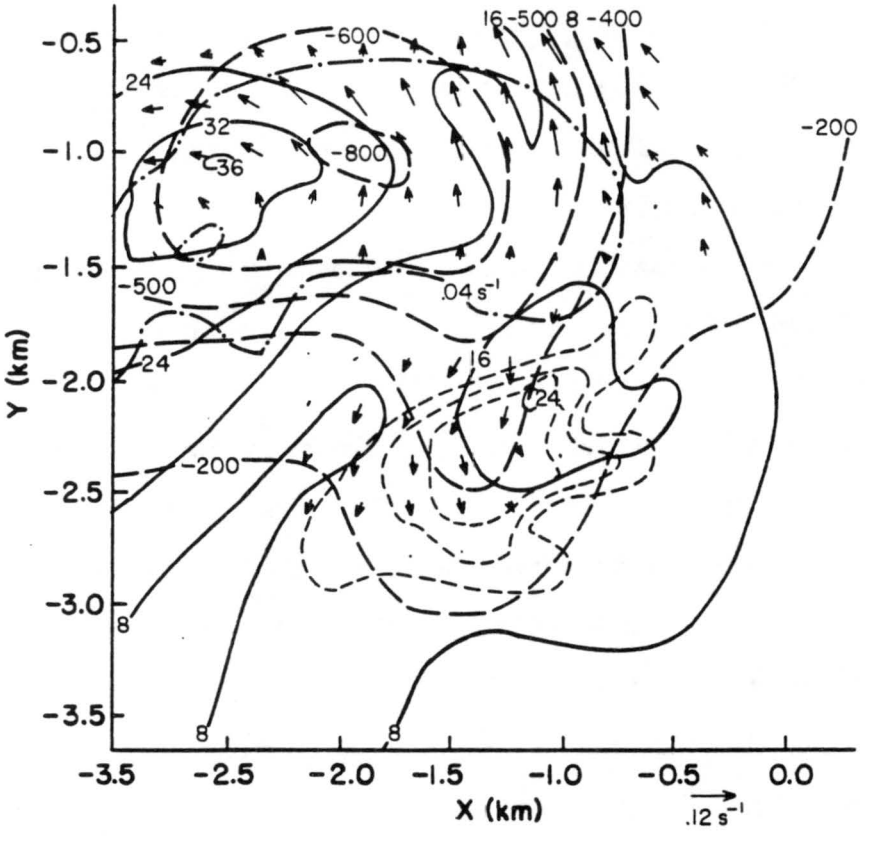

Figure 4.5: Same as Fig. 4.1 at 1633m and 99min.

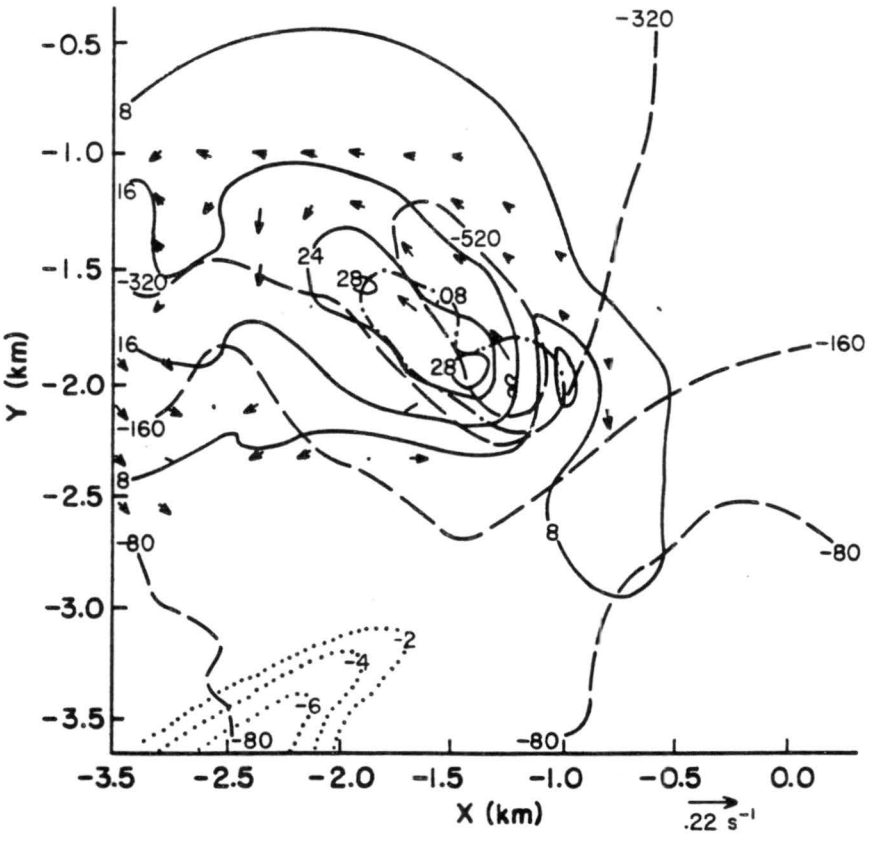

Figure 4.6: Same as Fig. 4.1 at 581m and 99min.

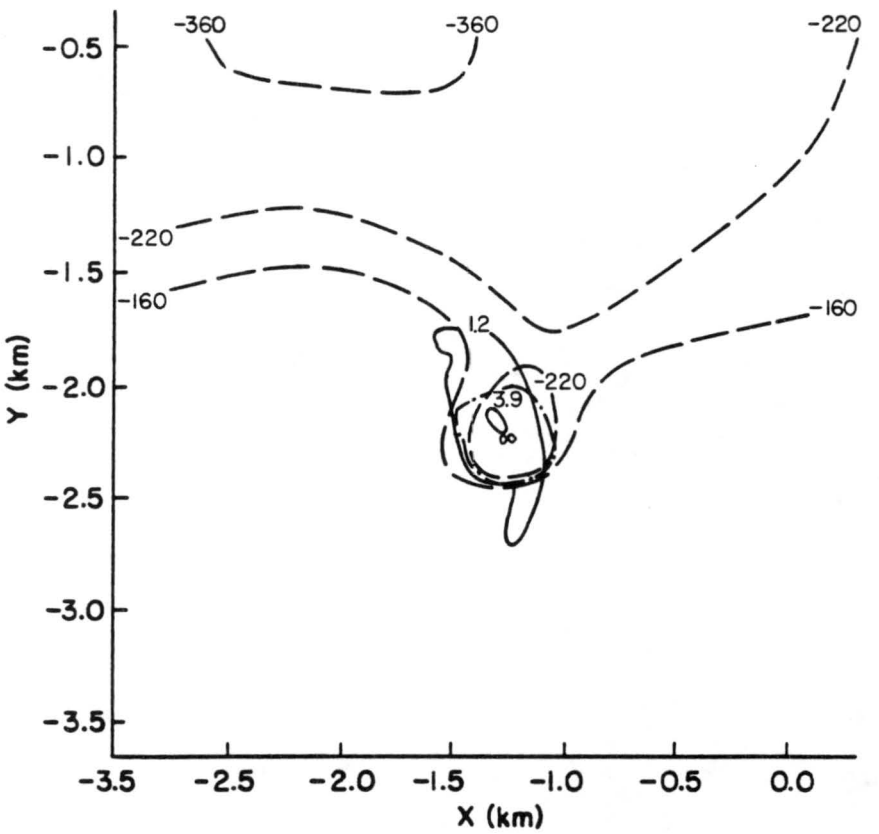

Figure 4.7: Same as Fig. 4.1 at 11m and 99min.

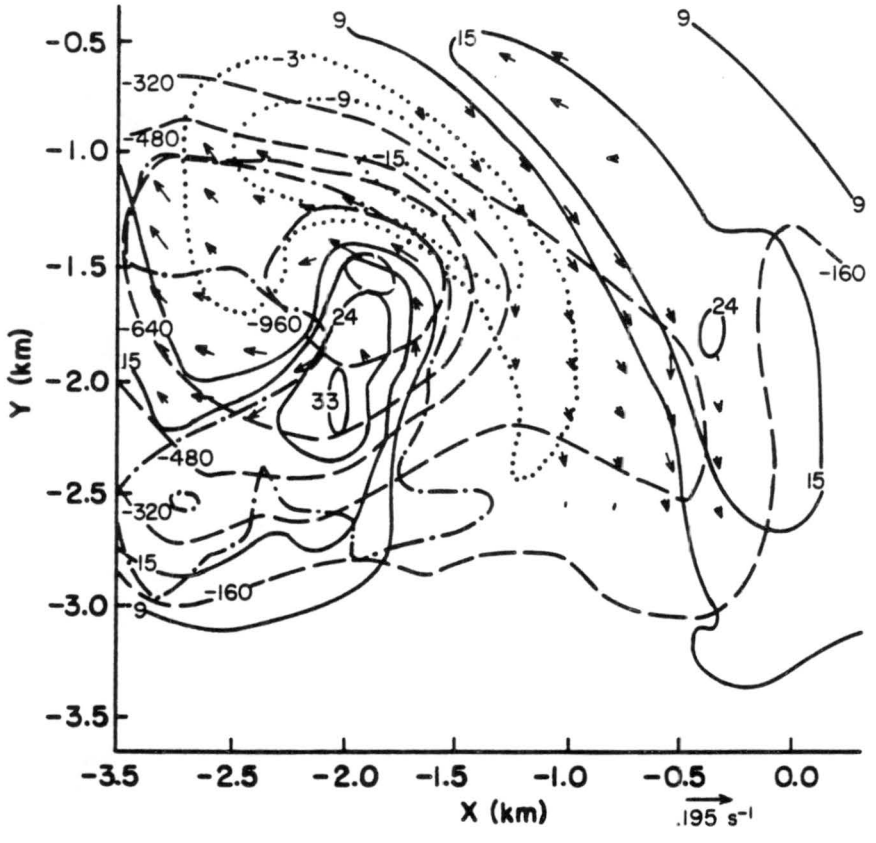

Figure 4.8: Same as Fig. 4.1 at 1095m and 105min.

Figure 4.8 shows the model fields at the time of the tornado's most intense stage. In this figure, at 1095m, the secondary updraft is now well to the east of the main updraft. The main updraft itself is now south of its original position. The newly-formed downdraft is quite strong (-15 m/s), and bounds the main updraft on the northern edge. The extrema in the pressure field is -1360 pa and is still located in the large horizontal gradient of updraft speed as well as the maximum in the total vorticity.

The pressure deficit fills rapidly with height above this level. At 1633 m the minimum pressure is only -800 pa. This hints at a possible forcing for the sudden formation of the strong downdraft that bounds the main updraft. If the air in the column from cloud base to 1633m is not strongly positively buoyant then it's possible that the vertical perturbation pressure gradient is responsible for forcing the downdraft.

Figure 4.9 shows the horizontal cut at 581 m. The 51 m/s updraft stands out as well as the -2400 pa pressure deficit. The downdraft to the northeast has a magnitude of -12 m/s and is the same downdraft that bounds the updraft on the northern edge in the last figure. To the east and southeast two updraft centers are seen.

The updraft reaches its most intense levels at 365m (Figure 4.10) with a magnitude of 60 m/s while the pressure deficit is -3000 pa! The updraft strengths at 283m, 215m, 158m and 11m are 56 m/s, 51 m/s, 45 m/s and 8.4 m/s, respectively. The corresponding pressure deficits are -2900 pa, -2600 pa, -2100 pa and -1280 pa respectively. These numbers are truly impressive and lend support to our contention that the feature producing them is, in fact, a tornado.

One minute later the downdraft has intensified to -36 m/s at 1095m and 892 m. The downdraft surges to the ground and the wind field at the sub-cloud levels become strongly divergent. The tornado is pushed south and the pressure deficits fill rapidly. This point is interpreted as the dissipation stage of the tornado and the simulation was stopped. A three dimensional animation of the model fields shows that the tornado lives for approximately 15 minutes.

In all of the above figures, the following distinct features were always present: the largest horizontal vorticity vectors, the largest values of vertical vorticity and the largest

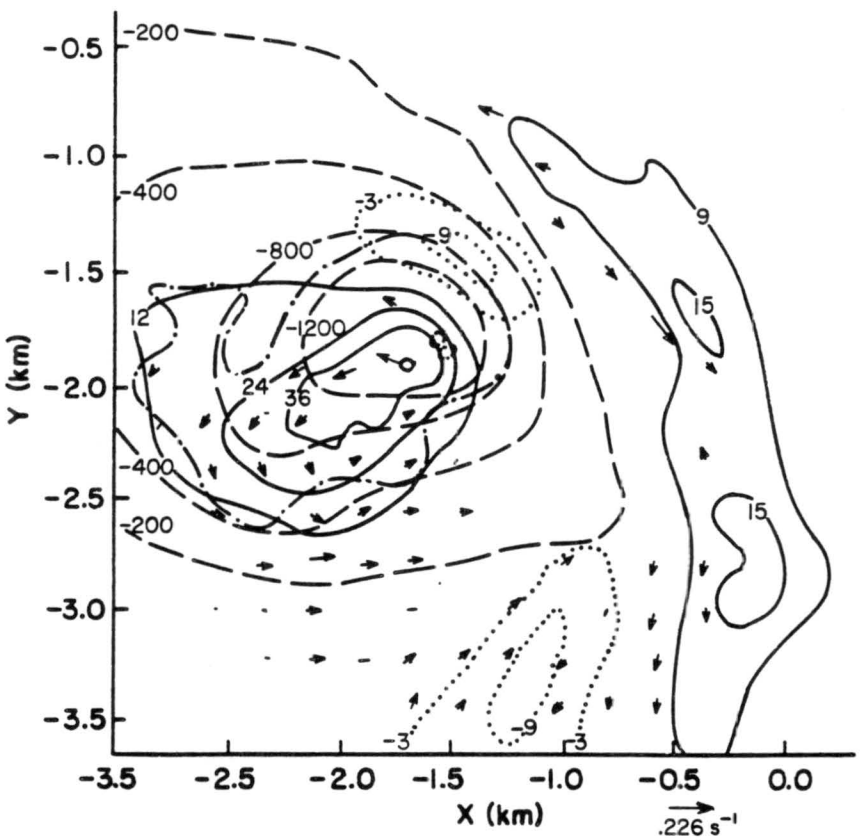

Figure 4.9: Same as Fig. 4.1 at 581m and 105min.

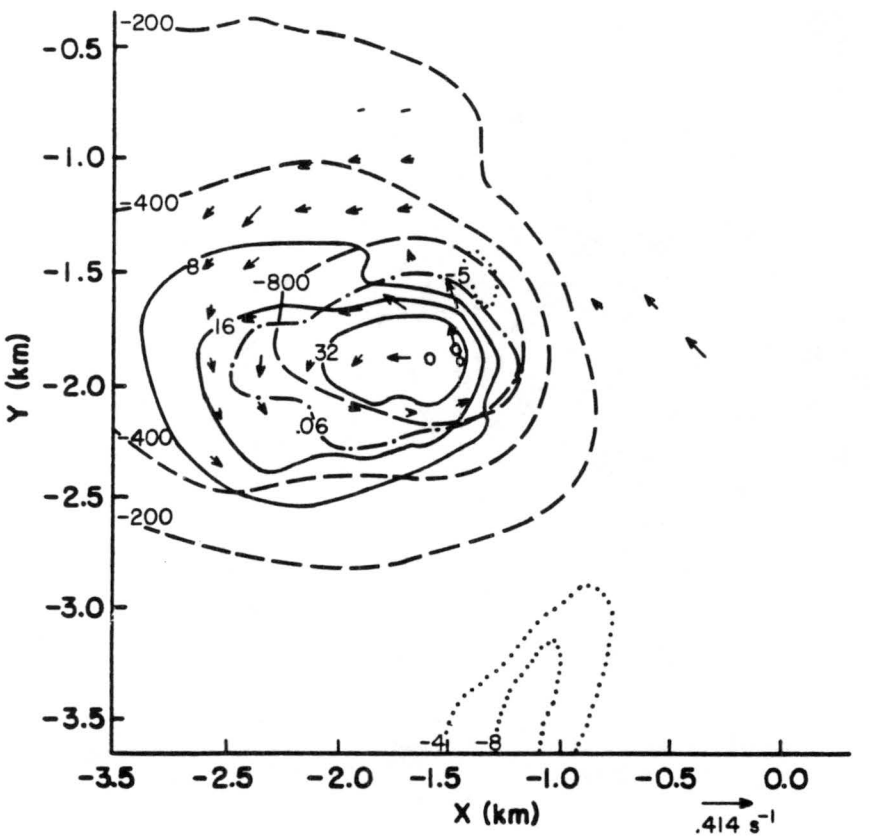

Figure 4.10: Same as Fig. 4.1 at 365m and 105min.

pressure deficits were always located in the region of the largest horizontal gradient of updraft speed.

The magnitude of the horizontal vorticity vectors is related to the horizontal gradient of vertical motion and the vertical gradient of horizontal motion. In the region of large horizontal shear of the updraft, the vertical shear is much smaller and as a result the magnitude of the horizontal vorticity vectors will reflect the large horizontal shear of the vertical motion of the storm. The largest horizontal vorticity vectors will therefore be located where the largest horizontal gradient of updraft speed is located. The magnitude of the horizontal vorticity vectors can also be discussed in terms of the horizontal gradients of buoyancy as seen in the last term of Eq. 19. The warm interior of the thunderstorms is a region of rapid ascent and the cool surroundings of the thunderstorm has very little vertical motion. The place in between is the region of the updraft gradient and hence the location of the large horizontal vorticity vectors.

Tilting/convergence of vortex tubes from the horizontal into the vertical is governed by the horizontal gradient of the updraft speed. The most efficient re-orientation will occur where the horizontal gradient of updraft speed is located. Therefore, the location where the vertical vorticity will be generated fastest is where the horizontal gradient of updraft speed is the largest and horizontal vorticity is present.

Focusing on the lowest levels of the tornado circulation, Figures 4.11-4.19 show the wind field at three heights, 463m, 158m and 11m in the subcloud air. Notice in Figure 4.11 that cyclonic circulation is present. The gust front has progressed to x = -1.0 with westerlies behind. To the east of the gust front and to the north of an east west line at y = -1.5 the flow has a significant easterly component. In the middle a well-defined vortex is present.

At 158m, Figure 4.12, shows the cyclonic circulation is not at all obvious to the eye. The air from the northwest is clearly seen to surge to the southeast where the leading edge has reached x = -1.5. To the north of y = -2.0 the flow is from the northeast and in between at x = -1.25, y = -2.25 the flow is exhibiting cyclonic circulation.

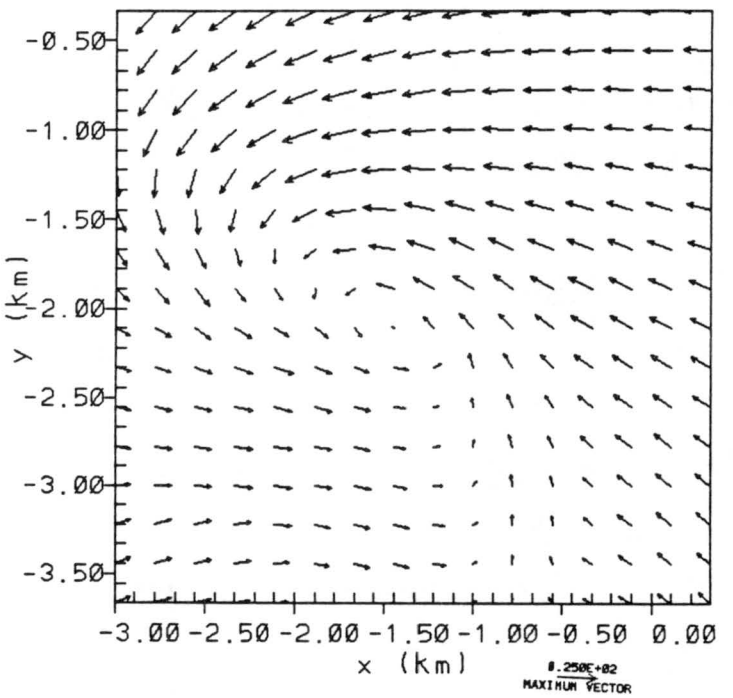

Figure 4.11: Horizontal cross section of horizontal wind vectors at 463m and 94min.

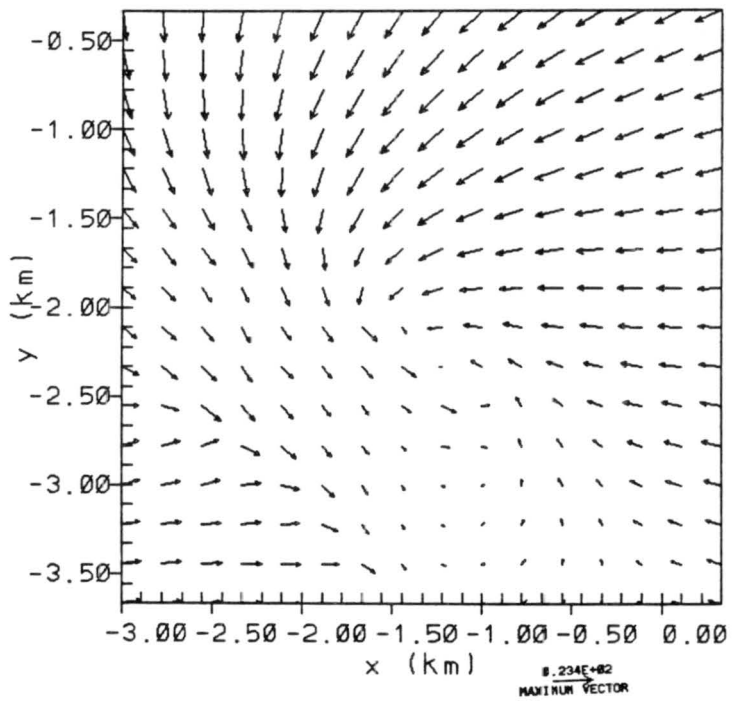

Figure 4.12: Same as Fig. 4.11 at 158m and 94min.

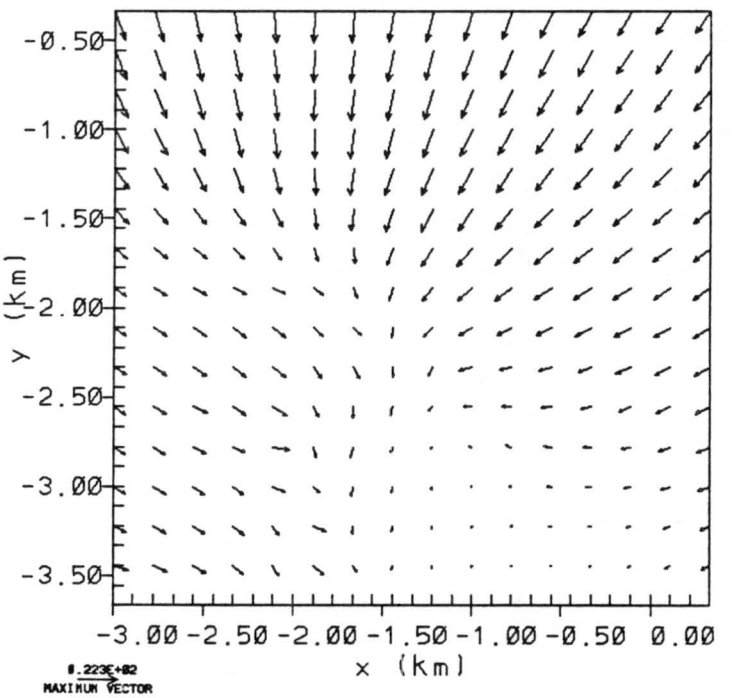

Figure 4.13: Same as Fig. 4.11 at 11m and 94min.

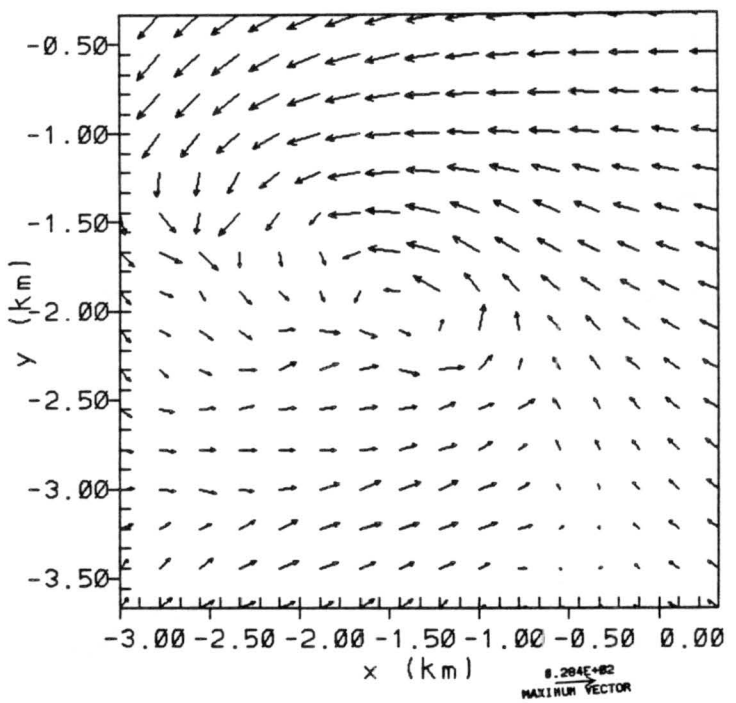

Figure 4.14: Same as Fig. 4.11 at 463m and 99min.

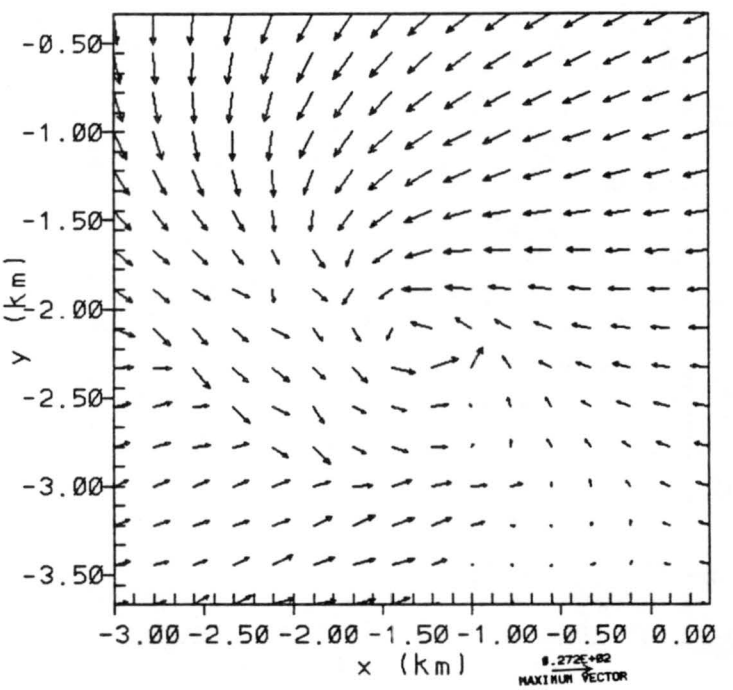

Figure 4.15: Same as Fig. 4.11 at 158m and 99min.

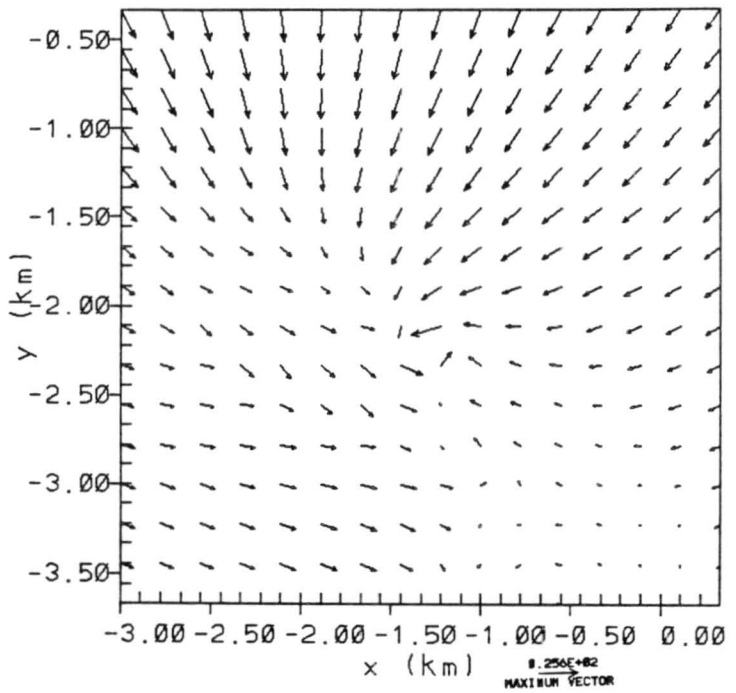

Figure 4.16: Same as Fig. 4.11 at 11m and 99min.

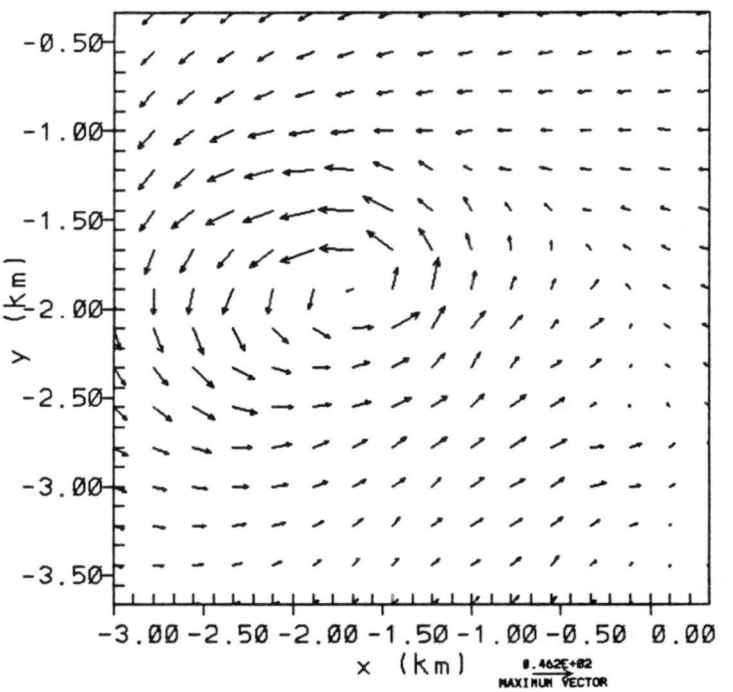

Figure 4.17: Same as Fig. 4.11 at 463m and 105min.

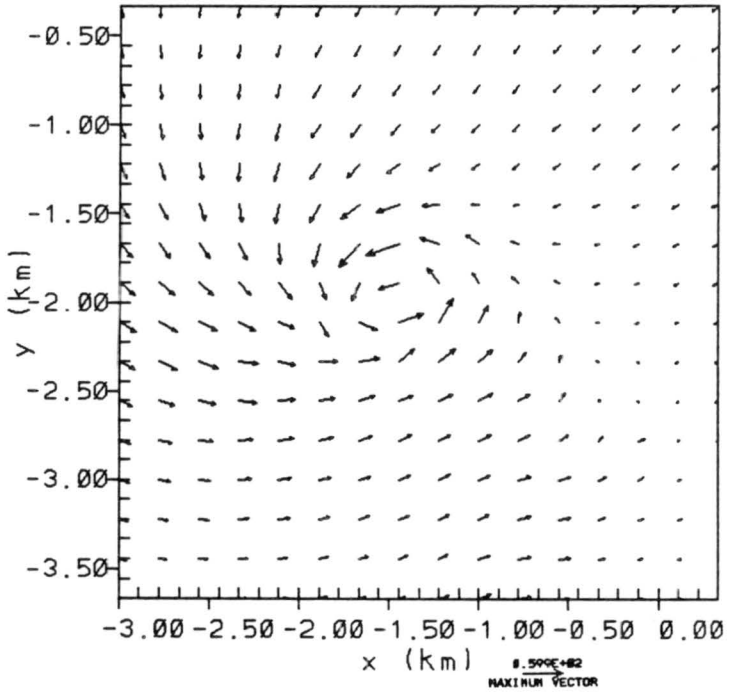

Figure 4.18: Same as Fig. 4.11 at 158m and 105min.

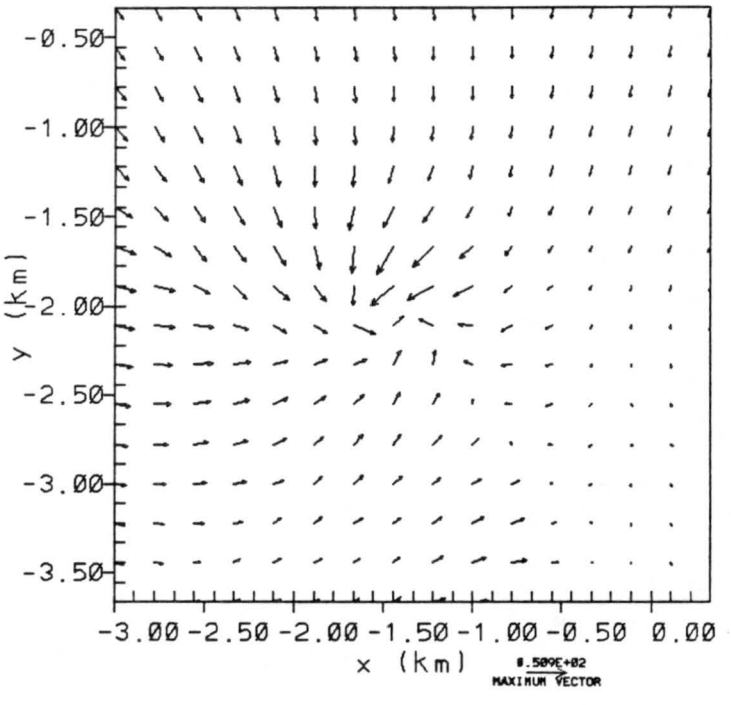

Figure 4.19: Same as Fig. 4.11 at 11m and 105min.

At the surface, Figure 4.13, the gust front has progressed to x = -1.75. Since the gust front has not progressed east enough, no significant cyclonic circulation has formed yet.

Three minutes later at 99 minutes, Figure 4.14 shows that the gust front has moved east to x = -.75 with the same flow characteristics as before. At 158m, Figure 4.15, the gust front has moved east to x = -1.0 and a well-defined rotation at x = -1.25 and y = -2.25 is now evident. Further down to the surface Figure 4.16 shows that the gust front has surged to x = -1.25. A marked circulation center is seen at x = -1.25, y = -2.25 that was not present earlier.

At the time of maximum intensity, the surface gust front (Figure 4.19) is orientated in a northwest to southeast direction from the circulation at x = -1.5, y = -2.0 to x = -0.5 at the southern boundary. At 158m, Figure 4.18, a dramatic and well-organized circulation is seen in the center of the grid. Again with air flowing from the northwest of the grid to the south of the circulation center to the gust front that arches from just east of the circulation center southeast to the lower right corner of the grid. At 463m, Figure 4.17, the well-defined circulation is present and is completely surrounded by downdraft air as the gust front has " occluded " the vortex.

The next few minutes that follow show the demise of the vortex as a significant downdraft forms and surges to the ground causing the air to become highly divergent. The tornado is no longer feeding on cyclonic circulation and dissipates.

4.4 Hypothesis of Tornadogenesis

In the above two paragraphs we have argued why the total three dimensional vorticity is maximized in the region of largest horizontal gradient of updraft speed. Referring back to the perturbation pressure equation, it follows that the region where the total vorticity or enstrophy is largest the pressure deficit will be a maximum provided that the strain rate in the same region is smaller. The fact that the largest pressure deficits are located in the same region as the largest horizontal gradient of updraft speed suggests that the strain rate must, indeed, be small. With all this in mind, the following theory for tornadogenesis is proposed.

As updraft air ascends in the intense supercell thunderstorm it accelerates from speeds of a few meters per second to over 45 m/s or more, at middle levels. At higher levels the updraft slows on approach to the tropopause and the overlying stratosphere. Since the diameter of the updraft is slightly smaller at mid-levels compared to lower levels, the horizontal gradient of the updraft will be largest near mid-levels. It is suggested that the clockwise turning, with height, of the shear vectors and the associated perturbation low on the downshear side of the vectors aids in accelerating the updraft on the forward side. This locally enhances the horizontal updraft gradient on the forward flank.

The vortex lines that spiral helically upward just outside the core of maximum updraft speed will be tilted/converged more efficiently in the region where the horizontal gradient of the updraft is largest. This process will increase the enstrophy locally and if the strain rate is smaller, the pressure will fall. As the pressure falls the vertical pressure gradient will increase at levels just below and an acceleration of the updraft will result at these lower levels. Since the updraft is now stronger at this lower level the horizontal gradient of updraft speed will increase causing the total vorticity to increase in this gradient by way of more efficient titling/convergence of the vortex lines found there. If the enstrophy is larger than the strain rate then the pressures will fall. The resulting lower pressure will cause the vertical pressure gradient to increase and cause an upward vertical acceleration from below. This process will build a pressure-deficit tube downward along the region of largest horizontal gradient of updraft speed.

As the pressure-deficit tube is building downward, what prevents the air above the maximum pressure loss from moving downward and filling in the tube? In the vertical equation of motion, the only forces are the pressure gradient and buoyancy. Therefore, to prevent a reversal in the updraft above the maximum pressure loss, the buoyant force must be upward and larger in magnitude than the downward pressure gradient.

It should also be pointed out that it is possible for the pressures to continue to fall, in the tube, above the maximum pressure loss if the strain rate decreases with time and the enstrophy remains fixed, or, if the strain rate remains fixed while the enstrophy increases with time. The pressures did infact fall throughout the entire pressure-deficit tube with time in the simulation.

The descent of the pressure-deficit tube via the above argument will not proceed to the surface because the subcloud air is generally negatively-buoyant and therefore resistant to the increasing vertical pressure gradient. This will inhibit the formation of a large horizontal gradient of the updraft near the ground where vertical motion is constrained to vanish and reduce the tilting/convergence of vortex lines. Some other agent must be present to allow the pressure tube to build down to the surface.

The simulated storm shows that the subcloud air has cyclonic circulation beneath the lowering, pressure tube. The two downdrafts, one to the west and northwest of the updraft associated with the precipitation and the second to the south associated with the clear slot are thought to play a key role in producing this circulation. As a growing updraft can bend up an initially horizontal vortex line, then a downdraft can bend down an initially horizontal vortex line. If the vortex lines are orientated streamwise, then the upstream side of the downdrafts will be the location of negative vertical vorticity while the downstream side will be locations of positive vertical vorticity. Therefore the downdraft in the clear slot can produce positive vertical vorticity to the south of the pressure-deficit tube. The main downdraft to the west can also produce positive vertical vorticity to the southwest of the pressure-deficit tube. Advection of these vortex lines towards the pressure tube will enhance the sub-cloud cyclonic circulation.

Since the air being ingested into the main updraft is being forced by surface convergence and is characterized by weak buoyuancy, the subcloud air influenced by the increasing vertical pressure gradient associated with the pressure-deficit tube, will ascend faster than that of the air around it. Therefore the pressure deficit will be co-located with the maximum in the updraft speed and not with horizontal gradient of the updraft. In response to the increased vertical acceleration of the subcloud air, horizontal convergence will take place. This will draw in subcloud air that is already rich in cyclonic circulation. The result is an increase of cyclonic circulation by converging the vortex lines and a corresponding increase of vertical vorticity. If the strain is smaller, and it will be since the flow is almost purely rotational, the pressure will fall and allow the pressure-deficit tube to continue working its way to the surface.

The presence of the lowering pressure-deficit tube or a cyclonically descending downdraft is not sufficient. It is possible for the lowering pressure-deficit tube to linger near cloud base and not be able to enhance sub-cloud circulation to produce a tornado if no downdraft is present to reorientate vortex lines. Likewise if the downdraft is present and if the pressure-deficit tube is not lowering far enough to enhance the sub-cloud circulation then no tornado will form. Therefore it is a necessary condition that both the lowering pressure-deficit tube be in phase, time wise, with the downdraft.

As the pressure tube lowers to the surface, feeding on the cyclonic circulation, the temperatures in the tube will fall. If the air is moist enough, condensation will occur; being visible for all to stop and take notice of natures most intense vortex, the tornado.

Chapter 5

CONCLUSIONS

RAMS has been used to aid in investigating processes that allow a thunderstorm to evolve into a tornadic state. We begin with a brief review of current theories of tornadogenesis.

5.1 Review of Past Ideas

Benton and Shapiro (1986) proposed the following concepts of tornadogenesis. They considered an axisymmetric mesocyclone with a jet along the axis of symmetry. Because buoyancy varies with height, the jet will be largest at the level of non-divergence. Maximum vertical stretching will be largest below this level. The vorticity about the vertical axis will be enhanced by this maximum stretching. As the vorticity increases the pressure will drop along the axis of symmetry. The resulting low pressure will accelerate fluid from below towards the axis and upward. As the fluid is accelerated upward, large vertical stretching will occur and hence increase the vertical vorticity. Since the vorticity is increasing the pressure will drop at this lower level and the process continues to the ground. Recall the simulated mesocyclone is axisymmetric and extends to the ground.

Implicit in this argument is that the process will transform the mesocyclone into tornadic strength. In their first paragraph they say "...and second, spin up of the mesoscale circulation into an intense tornadic vortex ...." Later it is said "...This could easily cause the spinning meso-scale vortex to intensify to tornadic strength ..." It's not clear whether the size of the "mesoscale circulation" contracts to a tornadic-sized circulation or if the mesoscale circulation stays the same size and the circulation increases. Note also their mechanism will cause the intensification to proceed along the axis of symmetry or central axis of the mesocyclone.

Observations suggest that tornadoes are a distinct intense vortex and are embedded within the mesocyclone. The location of the tornado is generally not along the central axis of the mesocyclone but rather on the edge. The mesocyclone also is not axisymmetric, in fact the theory contained in this thesis necessarily requires a distinct asymmetry to be present. The tornado and mesocyclone are two separate scales of rotation and for that reason a theory for tornadogenesis must be able to explain the formation of the tornado without changing the mesocyclone.

Davies-Jones (1982) points out that "Slight asymmetries in the atmosphere usually cause the mesocyclone to be the more intense circulation and it may begin producing funnel clouds, and even small tornadoes if there is sufficient background vertical vorticity at ground level. The final phase appears to await the development of a significant downdraft in the mesocyclone." It is this downdraft that transports to ground level, air with non-zero vertical vorticity derived from tilting the environmental horizontal vorticity. It therefore seems that the vertical shear of the environmental wind is of the utmost importance in tornadogenesis.

Klemp and Rotunno (1983) argue that the temperature gradient located from where the tornado will form running to the northeast, is an environment where horizontal vorticity can be generated baroclinically. Since air parcels move into the updraft along the isotherms, the horizontal streamwise vorticity will thus be tilted into the vertical and stretched. They point out that tilting can be very small since the stretching term will enhance the vertical vorticity exponentially.

Looking at a vortex line, at say, 50m above the ground and orientated along the temperature boundary to the northeast of the location where the tornado will form, it is not clear how, after the vortex line is tilted into the vertical, the vertical section of the vortex line is moved to the surface.

Vortex lines in a tornado are vertical and move radially out along the surface. After a vortex line is tilted into the vertical, it seems a downdraft is needed to transport the horizontal portion of the vortex line to the surface.

The Klemp, Rotunno theory lacks a mechanism to transport to the surface the horizontal section of the vortex lines so that horizontal winds may converge the parts of the vortex lines that have a vertical orientation.

Wakimoto and Wilson (1988) have investigated non-supercell tornadoes and have pointed out that the same mechanism could be important for supercell tornadoes. In their studies, vortices propagating along pre-existing convergent lines, co-locate with rapidly growing cumulus. The convergent lines may be outflow boundaries from old thunderstorms while the vortices are believed to be triggered by shear instabilities. Once the vortices move under a rapidly growing cumulus (prior to any significant radar echo aloft) vortex stretching is hypothesized to amplify the rotation while building it upwards into the weak echo region, the region of strongest vertical ascent. As far as supercell storms go, they point out "...it is interesting to speculate based on observations of dust whirls under flanking lines of supercells, that shearing or Helmholtz instabilities play an important role in tornadogenesis with supercells. If these small circulations along the flanking line are a common feature, they may move with the parent clouds of the flanking line as they merge into the main updraft of the supercell and thus provide the "optimal condition" for the formation of a tornado."

As this theory of upward building tornadoes is separate from downward building tornadoes from the mid-levels of mesocyclones, it is possible they are not mutually exclusive. For strong tornadoes, however, a different mechanism may be necessary. The missing link in tornado research is the connection between the mesocyclone and the formation of the tornado. It has been the intent of this thesis to help fill the void.

5.2 Proposed Theory of Tornadogenesis

In this study we find that the process of tornado formation can be summarized in the following steps:

1) A large horizontal gradient in the updraft on the inflow side of a mesocyclone develops.

2) Enhanced tilting/convergence of horizontal vortex lines into the vertical in the region of the large horizontal gradient of the updraft occurs.

3) Pressures fall rapidly in this region primarily as a result of the increased three dimensional vorticity, or enstrophy, and that this exceeds the strain rate.

4) Vertical pressure gradients develop that accelerate the updraft below this level.

5) Steps one through four repeat until the pressure-deficit tube reaches near cloud base.

6) As the pressure-deficit tube descends, the downdrafts, one to the west of the updraft associated with the precipitation and the other located with the clear slot to the south of the updraft, reorientate vortex lines so in the downstream side both downdrafts have positive vertical vorticity.

7) The downdrafts produce a cyclonic shear zone that the pressure-deficit tube can work on.

8) The cyclonic circulation is enhanced via horizontal convergence of vortex lines and the pressure-deficit tube can work its way to the surface becoming visible as a tornadic vortex if the air is moist enough.

It should be pointed out that if the vortex lines are orientated 180 degrees out of phase in the clear slot region, the downdraft there may produce negative vertical vorticity downstream, then, as these vortex lines converge an anti-cyclonic tornado may form to the south of the cyclonic one.

5.3 Future Research

To test the proposed mechanism for tornadogenesis a statistical study must be done. The key feature is the development of the large horizontal gradient of the updraft on the inflow side of the thunderstorm. The study must show that a high percentage of tornado-producing thunderstorms develop this large horizontal gradient in the updraft. Thunderstorms that do not develop tornadoes on the edge, must lack this gradient.

Unfortunately there is no tool to directly observe this feature. It's not enough to derive the updraft field from horizontal winds using the continuity equation since forming derivatives of winds, that contain small errors, can yield larger errors. The derived updraft gradient will also inherit these errors. It is critical that the errors be an absolute minimum and therefore a new tool will be needed to directly observe the large horizontal gradient of the updraft.

Detection of this updraft gradient will precede the formation of the tornado vortex signature by a few minutes, perhaps up to ten minutes. This will give the National Weather Service more time to warn the public that a thunderstorm is evolving into a tornadic state.

New ways to initialize severe cumulus convection models should be the next endeavor. Perhaps profilers and satellites to obtain winds and infer temperature and moisture fields on mesoscales and assimilate these date into a model is a possible procedure.

Chapter 6

REFERENCES

Battan, L.S., 1973: *Radar Observation of the Atmosphere.* University of Chicago Press, 324 pp.

Benton, G.S., Shapiro, A.M., 1986: A possible explanation for the sudden spin-up of tornadoes and other small scale atmospheric vortices. Preprints, 16th Conf. Severe Local Storms, Amer. Meteor. Soc., Boston, J93-J98.

Brandes, E.A., 1984: Relationships between radar-derived thermodynamic variables and tornadogenesis. *Mon. Wea. Rev.*, **112**, 1033-1052.

Browning, K.A., and F.H. Ludlam, 1962: Airflow in convective storms. *Quart. J. Roy. Meteor. Soc.*, **88**, 117-135.

Burgess, D., L. Hennington, R. Doviak and P.S. Ray, 1976: Multimoment Doppler display for severe storm identification. *J. Appl. Meteor.*, **15**, 1302-1306.

Burgess, D.W., Wood, V.T., Brown, R.A., 1982: Mesocyclone Evolution Statistics. Preprints, 12th conf. Severe Local Storms, Amer. Meteor. Soc., Boston, 422-424.

Chisholm, A.S., and J.H. Renick, 1972: The kinematics of multicell and supercel hail-storms. Alberta Hail Studies, Research Council of Alberta Hail Studies, Rep. 72-2, 24-32, 53 pp.

Cotton, W.R. and R.A. Anthes, 1989: *Storm and Cloud Dynamics.* Academic Press, Inc., San Diego. International Geophysics Series, Vol. 44., 883 pp.

Cotton, W.R., and G.J. Tripoli, 1978: Cumulus convection in shear flow– Three dimensional numerical experiments. *J. Atmos. Sci.*, **35**, 1503-1521.

Davies-Jones, R.P., 1982: Tornado dynamics. In *Thunderstorms: A Social, Scientific, and Technological Documentary*, E. Kessler, Ed., Vol. 2, U.S. Department of Commerce, Washington, D.C. 20402, 313 pp.

Deardorff, J.W., 1970: A three-dimensional numerical investigation of the idealized planetary boundary layer. *Geophys. Fluid Dyn.*, **1**, 377.

Fawbush, E.J., and R.C. Miller, 1954: The types of air masses in which North American tornadoes form. *Bull. Amer. Meteor. Soc.*, **35**, 154-165.

Fujita, T.T., 1959: Precipitation and cold air production in mesoscale thunderstorm systems. *J. Meteor.*, **16**, 454-466.

Fujita, T.T. and Wakimoto, R.M., 1982: Anticyclonic tornadoes in 1980 and 1981. Preprints, 12th Conf. Severe Local Storms, Amer. Meteor. Soc., Boston, 401-404.

Klemp, J.B. and D.K. Lilly, 1978: Numerical simulation of hydrostatic mountain waves. *J. Atmos. Sci.*, **35**, 78-107.

Klemp, J.B. and R.B. Wilhelmson, 1978a: The simulation of three-dimensional convective storm dynamics. *J. Atmos. Sci.*, **35**, 1070-1096.

Klemp, J.B. and R.B. Wilhelmson, 1978b: Simulations of right- and left-moving storms produced through storm splitting. *J. Atmos. Sci.*, **35**, 1097-1110.

Klemp, J.B., R.B. Wilhelmson, and P. Ray, 1981: Observed and numerically simulated structure of a mature supercell thunderstorm. *J. Atmos. Sci.*, **38**, 1558-1580.

Lilly, D.K., 1982: The development and maintenance of rotation in convective storms. Topics in Atmospheric and Oceanographic Sciences: Intense Atmospheric Vortices. L. Bengtsson and J. Lighthill, Eds., Springer-Verlag, Berlin & Heidelberg, 149-182.

Ludlam, F.H., 1963: Severe local storms: A review. *Meteor. Monogr.*, **5**, No. 27, Amer. Met. Soc., Boston.

Palmen, E., and C.W. Newton, 1969: Atmospheric Circulation Systems: Their Structure and Physical Interpretation. *International Geophysics Series, Vol. 13,* Academic Press, Inc., 603 pp.

Ray, P.S., B.C. Johnson, K.W. Johnson, J.S. Bradberry, J.J. Stephens, K.K. Wagner, R.B. Wilhelmson and J.B. Klemp, 1981: The morphology of several tornadic storms 20 May 1977. *J. Atmos. Sci.,* **38**, 1643-1663.

Rotunno, R., and Klemp, J.B., 1982: The influence of the shear-induced pressure gradient on thunderstorm motion. *Mon. Wea. Rev.*, **110**, 136-151.

Schlesinger, R.E., 1978: A three-dimensional numerical model of an isolated thunderstorm: Part I. Comparative experiments for variable ambient wind shear. *J. Atmos. Sci.,* **35**, 690-713.

Schlesinger, R.E., 1980: A three-dimensional numerical model of an isolated thunderstorm. Part II: Dynamics of updraft splitting and mesovortex couplet evolution. *J. Atmos. Sci.,* **37**, 395-420.

Takeda, T., 1966: Effect of the prevailing wind with vertical shear on the convective cloud accompanied with heavy rainfall. *J. Meteor. Soc. Japan,* **44**, 129-143.

Uccellini, L.W., and D.R. Johnson, 1979: The coupling of upper- and lower-tropospheric jet streaks and implications for the development of severe convective storms. *Mon. Wea. Rev.*, **107**, 682-703.

Wakimoto, R.M., Wilson, J.W., 1989: Non-supercell tornadoes. *Mon. Wea. Rev.*, **117**, 1113-1139.

Weisman, M., and J. Klemp, 1982: The dependence of numerically simulated convective storms on vertical wind shear and buoyancy. *Mon. Wea. Rev.,* **110,** 504-520.

Wilhelmson, R., 1974: The life cycle of a thunderstorm in three dimensions. *J. Atmos. Sci.,* **31,** 1629-1651.

Wilhelmson, R.B. and J. Klemp, 1981: A three-dimensional numerical simulation of splitting severe storms on 3 April 1964. *J. Atmos. Sci.,* **38,** 1581-1600.